

LIBRARY
Michigan State
University

PLACE IN RETURN BOX to remove this checkout from your record.
TO AVOID FINES return on or before date due.

DATE DUE	DATE DUE	DATE DUE
JUN 11 1997 2 0 23	AUG 23 2004 5 0 5 10	

**MODELING THE ELECTROMAGNETIC FIELD AND THE PLASMA
EXCITATION IN A MODERATE PRESSURE MICROWAVE CAVITY PLASMA
SOURCE**

By

Wen-yi Tan

A DISSERTATION

Submitted to
Michigan State University
in partial fulfillment of the requirements
for the degree of

DOCTOR OF PHILOSOPHY

Department of Electrical Engineering

1994

ABSTRACT

MODELING THE ELECTROMAGNETIC FIELD AND THE PLASMA EXCITATION IN A MODERATE PRESSURE MICROWAVE CAVITY PLASMA SOURCE

By

Wen-yi Tan

Microwave plasma sources are used for the generation of plasma discharges in a number of applications including diamond thin film deposition. A numerical model has been developed for these microwave plasma sources which includes an electromagnetic field model and a fluid plasma model. The microwave plasma source modeled was a cylindrical, single mode excited cavity with an input power probe for coupling the microwave energy into the cavity. The time-varying electromagnetic fields inside the resonant cavity, both inside and outside the discharge region, are obtained using the electromagnetic field model which incorporates a finite-difference time-domain (FDTD) method to solve Maxwell's equations. The microwave electric field interactions with the plasma discharge are described using a finite difference solution of the electron momentum transport equation. The characteristics of the discharge are simulated by the fluid plasma model which solves the electron and ion continuity equations, electron energy balance equation, and the Poisson equation. A final self-consistent solution is obtained by iteratively solving the electromagnetic field model and the fluid plasma

model.

In particular, a TM_{01n} mode, 17.78 cm i.d. microwave cavity plasma reactor used for diamond thin film deposition is simulated using this numerical model. The spatial electric field patterns, power absorption patterns, and quality factor of the cavity loaded with a hydrogen discharge are investigated in the moderate pressure range (1 Torr - 100 Torr). The physical behavior of the hydrogen discharge, such as plasma density, electron temperature, and plasma potential, are also simulated and analyzed for various input conditions. The simulated results are compared with experimental data. Calculations of the electromagnetic fields using the FDTD techniques are also done for a compact electron cyclotron resonance (ECR) plasma source and for an argon coaxially loaded microwave cavity plasma source. Additionally, microwave cavities loaded with lossy loads of various conductivities were simulated and compared to exact analytical solution. Agreement was found between the numerical FDTD solution and the analytical solution.

To my parents

ACKNOWLEDGMENTS

The author wishes to thank Dr. Timothy A. Grotjohn for his encouragement, guidance and support throughout this research. Thanks are also given to guidance committee members, Dr. Jes Asmussen, Dr. Donnie Reinhard, and Dr. David Yen for taking time to serve on the examining committee.

This research was supported in part by grants from National Science Foundation.

TABLE OF CONTENTS

LIST OF TABLES.....	x
---------------------	---

LIST OF FIGURES	xi
-----------------------	----

Chapter 1	Introduction.....	1
-----------	-------------------	---

1.1	Introduction.....	1
-----	-------------------	---

1.2	Objective	4
-----	-----------------	---

1.3	Outline	5
-----	---------------	---

Chapter 2	Electromagnetic Field Model	8
-----------	-----------------------------------	---

2.1	Introduction	8
-----	--------------------	---

2.2	Review of electromagnetic field model	10
-----	---	----

2.2.1	Frequency domain	11
-------	------------------------	----

2.2.2	Time domain	13
-------	-------------------	----

2.3	FDTD model implementation in cylindrical coordinates	20
-----	--	----

2.4	Conductivity models for FDTD model implementation	25
-----	---	----

2.4.1	Conductivity model for non-dispersive lossy materials	26
-------	---	----

2.4.2	Plasma conductivity model	27
-------	---------------------------------	----

2.4.2.1	Time harmonic domain solution	28
2.4.2.2	Time domain solution	32
2.5	Summary	33
Chapter 3	Numerical Models of Plasma Discharges	34
3.1	Introduction	34
3.2	Review of plasma discharge models	34
3.2.1	Particle model	35
3.2.2	Continuum (fluid) model	37
3.3	Model development	40
3.3.1	Distribution function	40
3.3.2	Boltzmann transport equation	43
3.3.3	Moment equations	44
3.3.4	Drift-Diffusion model	47
3.3.5	Fluid model	49
3.4	Numerical solution implementation	52
3.4.1	Discretization	53
3.4.2	Numerical solution	58
3.5	Summary	62
Chapter 4	Transient State Simulation of Electromagnetic Fields Inside Empty and Loaded Microwave Resonant Cavities	63
4.1	Introduction	63
4.2	Simulation of electromagnetic fields inside empty cavities	64

4.3	Natural frequency response for loaded lossy cavity	71
4.4	Simulation results of an argon plasma loaded cavity	85
4.5	Implementation and results for a compact ECR ion source	89
4.6	Summary	94
Chapter 5	Steady State Simulation of Electromagnetic Fields Inside Plasma Loaded Microwave Resonant Cavities	100
5.1	Introduction	100
5.2	Non-reflecting boundary conditions	103
5.3	Implementation for a coaxial waveguide	107
5.4	Implementation for a Microwave Cavity Plasma Reactor	112
5.5	Simulation results for a cavity reactor loaded with a H2 discharge	124
5.6	Conclusions	135
Chapter 6	Self-consistent Simulation of a Microwave Cavity Plasma Reactor	138
6.1	Introduction	138
6.2	Model description	138
6.3	Reactor description and Q value measurement	142
6.4	Implementation for H2 discharge simulation	150
6.5	Simulation results for fluid plasma model	156
6.6	Self-Consistent results for microwave cavity plasma reactor simulation	159
6.7	Summary	174

LIST OF TABLES

Table 1: H ₂ reaction rates.	155
--	-----

LIST OF FIGURES

Figure 1-1: Overview diagram.	6
Figure 2-1: Schematic description of microwave discharge generation.	9
Figure 2-2: A FDTD unit cell in three-dimensional cylindrical coordinates.	16
Figure 2-3: Leap-frog scheme.	18
Figure 3-1: The distribution function f can be described by three moments: n , $\langle v \rangle$, and $\langle \xi \rangle$	42
Figure 3-2: Staggered-mesh arrangement.	54
Figure 4-1: TE ₀₁₁ , TE ₁₁₁ , TM ₀₁₁ , and TM ₀₁₂ mode excitation techniques in a cylindrical cavity.	65
Figure 4-2: Electric field energy, $\frac{1}{V} \int_V \epsilon_0 E^2 dV$, versus time for the TE ₀₁₁ mode. The empty cylindrical cavity was 15.25 cm in diameter and 6.5 cm high.	68
Figure 4-3: Radial dependence of $ E_\phi $ at four different z locations for the TE ₀₁₁ mode.	69
Figure 4-4: Grid structure for FDTD simulation in cylindrical coordinate.	70
Figure 4-5: Electric field energy, $\frac{1}{V} \int_V \epsilon_0 E^2 dV$, versus time for the TM ₀₁₁ mode. The cylindrical empty cavity was 17.8 cm in diameter and 7.2 cm high. The resonant frequency was 2.45 GHz.	72
Figure 4-6: Total stored energy, U , versus time for the TM ₀₁₁ mode.	73

Figure 4-7: $ E_r $ (arbitrary units) versus z at four different r locations for the TM_{011} mode.	74
Figure 4-8: $ E_r $ (arbitrary units) versus z at four different r locations for the TM_{012} mode. The cylindrical empty cavity was 17.8 cm in diameter and 14.41 cm high. The resonant frequency was 2.45 GHz.	75
Figure 4-9: $ E_r $ (arbitrary units) versus ϕ at three different r locations for the TE_{111} mode. The cylindrical empty cavity was 8.9 cm in diameter and 6.9 cm high. The resonant frequency was 2.45 GHz.	76
Figure 4-10: Configuration of a coaxially loaded cylindrical cavity.	79
Figure 4-11: Fine grid structure for TE_{011} mode lossy cavity simulation.	80
Figure 4-12: Space averaged $ E ^2$ (arbitrary units), versus time, for the TE_{011} mode. Results are shown for three different load conductivities after the source is turned off.....	81
Figure 4-13: Total stored energy, U , versus time for the TE_{011} mode for three different load conductivities.	82
Figure 4-14 Radial dependence of $ E_\phi $ (arbitrary units) for the TE_{011} mode for three different conductivity loads in a 15.25 cm i.d. cylindrical cavity.	83
Figure 4-15: S-plane plot for the complex frequency as a function of load conductivity for the TE_{011} mode.	84
Figure 4-16: The geometry of a 17.8 cm i.d. cylindrical cavity with a 12 mm i.d. quartz tube loaded with an argon plasma.	86
Figure 4-17: Electron density, n_e , and effective collision frequency, ν_{eff} , versus pressure for the argon plasma shown in Figure 4-16.	88
Figure 4-18: Loaded cavity quality factor, Q , versus pressure.	90
Figure 4-19: Absorbed power density versus pressure.....	91
Figure 4-20: Simulation structure for an compact ECR ion source.	92
Figure 4-21: Electric field energy, $\frac{1}{V} \int \epsilon_0 E^2 dV$, versus time for the structure shown in Figure 4-20 with no plasma load present. The excitation of the source was turned off at time = 0.6 nsec.....	93

Figure 4-22: $ E_r $ (arbitrary units) versus r and z	95
Figure 4-23: $ E_z $ (arbitrary units) versus r and z	96
Figure 4-24: $ E_r $ (arbitrary units) versus r and z for the compact ion source operated with a helium plasma discharge.	97
Figure 4-25: $ E_z $ (arbitrary units) versus r and z for the compact ion source operated with a helium plasma discharge.	98
Figure 5-1: Steady-state response of the electric field energy, $\frac{1}{V} \int_V \epsilon_0 E^2 dV$, versus time for the TE_{011} mode.	101
Figure 5-2: Grid termination structure.	106
Figure 5-3: Simulation structure for the cylindrical coaxial waveguide.	108
Figure 5-4: Non-reflecting boundary simulation results: (above) spatial average E_r vs. time at two different cross section (solid: $z=30$, dash: $z=0$). (below) spatial average power flow vs. time (solid: $z=10$, dash: $z=20$).	110
Figure 5-5: Spatial variation (r vs. z) of the $ E_r $ component for the TEM mode in a cylindrical coaxial waveguide.	111
Figure 5-6: Configuration of a microwave cavity plasma reactor used for diamond film deposition. The cavity diameter is 17.78 cm.	113
Figure 5-7: Simplified simulation structure for a microwave cavity plasma reactor. .	114
Figure 5-8: Electric field energy vs. time for TM_{012} mode cavity simulation.	117
Figure 5-9: $ E_r $ field distribution for a TM_{012} mode microwave cavity plasma reactor.	118
Figure 5-10: $ E_z $ field distribution for a TM_{012} mode microwave cavity plasma reactor.	119
Figure 5-11: Field patterns of TM_{012} mode cylindrical cavity.	120
Figure 5-12: Q vs. cavity height for three different conductivity loaded TM_{012} mode cavity simulation.	122
Figure 5-13: Reflected power vs. cavity height for TM_{012} mode cavity simulation. ...	123

Figure 5-14: Simulation structure cross-section for microwave cavity plasma reactor.	126
Figure 5-15: Q value vs. electron density at a pressure of 20 Torr.	128
Figure 5-16: Q value vs. electron density at a pressure of 70 Torr.	129
Figure 5-17: $ E_r $ distribution in the r - z plane at 20 Torr for a plasma density = $3 \times 10^{12} \text{ cm}^{-3}$	131
Figure 5-18: $ E_z $ distribution in the r - z plane at 20 Torr for a plasma density = $3 \times 10^{12} \text{ cm}^{-3}$	132
Figure 5-19: $ E_r $ distribution in the r - z plane at 70 Torr for a plasma density = $8 \times 10^{13} \text{ cm}^{-3}$	133
Figure 5-20: $ E_z $ distribution in the r - z plane at 70 Torr for a plasma density = $8 \times 10^{13} \text{ cm}^{-3}$	134
Figure 5-21: Power density distribution in the r - z plane at 20 Torr for a plasma density = $3 \times 10^{12} \text{ cm}^{-3}$	136
Figure 5-22: Power density distribution in the r - z plane at 70 Torr for a plasma density = $8 \times 10^{13} \text{ cm}^{-3}$	137
Figure 6-1: Flow chart for microwave cavity plasma reactor simulation.	141
Figure 6-2: Microcoax probe and holes in the cavity walls.	143
Figure 6-3: Electric field strength vs. cavity height for microwave cavity plasma reactor during diamond deposition process.	148
Figure 6-4: Field patterns for TM_{013} mode.	149
Figure 6-5: Simulation structure cross-section for microwave cavity plasma reactor with quartz tube.	151
Figure 6-6: Grid structure for fluid plasma model.	153
Figure 6-7: Simulation results of microwave cavity plasma reactor using fluid plasma model with uniform absorbed power density. (a) Electron density (b) Plasma potential (c) Electron temperature (c) Neutral temperature (assigned values).	157
Figure 6-8: Electron temperature and density variations during fluid plasma simulation.	158

Figure 6-9: E_r field distribution.	161
Figure 6-10: E_z field distribution.	162
Figure 6-11: Conductivity distribution.	163
Figure 6-12: Absorbed power patterns.	164
Figure 6-13: E_r field pattern inside the quartz disk region.	165
Figure 6-14: E_z field pattern inside the quartz disk region.	166
Figure 6-15: Simulation results of a microwave cavity plasma reactor for pressure = 50 Torr and input microwave power = 1500 watt. (a) Electron density (b) Plasma potential (c) Electron temperature (d) Neutral temperature (assigned values).	168
Figure 6-16: Spatial variation of ionization rate and recombination rate for pressure = 50 Torr and input microwave power = 1500 watt.	169
Figure 6-17: Spatial distribution of various energy loss for pressure = 50 Torr and input microwave power = 1500 watt.	170
Figure 6-18: Absorbed power vs. number of iterations.	171
Figure 6-19: Neutral temperature and plasma volume vs. incident power for various pressures.	172
Figure 6-20: Electron temperature vs. absorbed power for three different pressures. ..	173
Figure 6-21: Q value vs. absorbed power for three different pressures.	175

Chapter 1

Introduction

1.1 Introduction

Microwave excited plasmas have demonstrated excellent potential in high-pressure (>100 Torr), moderate-pressure (1 Torr - 100 Torr), and low-pressure (0.1 mTorr - 1 Torr) plasma processing applications because of their ability to create high densities of excited and charged species without high plasma sheath potentials and contamination from electrodes. One way to create a microwave excited plasma is utilizing a single mode microwave resonance cavity which couples microwave energy into the discharge with or without a static multipolar magnetic field [1]. Previous studies have shown that microwave plasma reactor sources can efficiently produce microwave discharges at high pressures for thermal processing applications [2], at moderate pressure (10 -100 Torr) for diamond film deposition [3], and at low pressure for silicon and III-V etching applications [4][5].

The further development of microwave plasma processing technology requires that the physical behavior of discharges inside microwave plasma reactors be better understood and characterized. One of the major issues regarding this field is the plasma

heating mechanism, and in particular, the electromagnetic excitation mechanism of discharges inside microwave plasma sources. Generally, the discharges inside these sources are generated and sustained by the microwave fields either through collisional (Joule) heating or through electron cyclotron resonance (ECR) heating if an appropriate static magnet field is present. Inside the discharges, since the mass of electrons is much less than the mass of ions, electrons are usually accelerated to higher energies than the ions by microwave fields. Therefore, the electromagnetic field energy is mainly imparted to the electron gas, and the discharge heating mechanism is mainly determined by the behavior of electrons.

Under moderate pressure conditions, the ECR heating mechanism becomes insignificant since the mean free path of electrons, i.e., the distance between two consecutive collisions, is much smaller than that in low pressure conditions. The electrons can not resonate in the microwave electric field long enough to gain energy between collisions. Therefore, under moderate pressure conditions, the plasma is usually unmagnetized, and created mainly by Joule heating. During the Joule heating process, the electrons are accelerated by the input microwave electric field, and a net transfer of energy to the electrons occurs as the electrons undergo elastic collisions with heavier particles such as ions and neutrals. In particular, the direction of electron motion changes during elastic collisions, causing a net transfer of energy from the oscillating microwave fields to the electron. This energetic electron gas can further transfer energy to heavier gas particles by inelastic collision processes, such as gas ionization and dissociation. Thus, the input gas is partially ionized and a discharge inside a plasma reactor is created.

Once ionization and dissociation occurs, the energy loss mechanism of discharges depends on a number of factors including a key factor which is pressure. When the pressure is low, the collisions between particles are infrequent, so electrons, ions, and dissociated atoms will diffuse to the boundary wall where wall recombination takes place. Hence, the discharge spreads out and fills the whole chamber, and the main energy loss is due to diffusion processes. As the pressure is increased the rate of volume recombination increases. Electrons, ions, and free radicals recombine quickly and convert the ionization, dissociation and excitation energy into thermal energy. The discharge then contracts away from the wall boundary and becomes thermally inhomogeneous. Heat conduction then becomes an important energy loss mechanism of the discharges [2][3].

A key consideration for the operation of microwave plasmas is the impedance matching between the microwave generator and the applicator which couples the microwave power into the plasma. An impedance mismatch causes a partial reflection of microwave power by the applicator; hence not all the power delivered by the generator can be used to sustain the plasma. This behavior essentially arises from the fact that the impedance of the applicator, and the resonance characteristics of a cavity, strongly depend on the actual plasma state, e.g., density, temperature and electrical conductivity. Therefore, in order to understand the coupling efficiency from the generator to the applicator, the characteristics of the resonant cavity, and the interactions between discharge and resonant microwave field, have to be studied in a systematic manner.

In order to understand these behaviors of the plasma inside a cavity reactor source, microwave fields, gas transport, energy transport, as well as, their relations should be investigated carefully. The coupling among these is complex and analytic models are hard

to apply to handle these problems. Thus, a systematic numerical model, which can self-consistently solve the plasma behavior as well as the exciting microwave fields, is essential to provide insight, interpret experiments, and help in the design, development, and control of microwave plasma reactors.

1.2 Objective

The overall objective of this study is to develop a self-consistent numerical model of a single mode microwave cavity plasma reactor source. This model will provide the steady state electromagnetic field solutions inside cylindrical resonant cavity structures loaded with H_2 discharges, as well as, be used to investigate the excitation mechanism and characteristics of these discharges across a pressure range (100 mTorr to 100 Torr) and across an input power range. The overall significance of this study is to build up a self-consistent model of microwave cavity plasma excitation.

The overall objective may be divided into several specific objectives which include:

1. To develop a time domain numerical model to simulate the steady state electromagnetic fields inside a cylindrical cavity with a specific resonant mode or input coupling structure. The cavity can be either empty or loaded with a plasma.
2. To develop a plasma model which can describe the physical behavior and investigate the characteristics of H_2 discharges inside a microwave cavity plasma reactor source.
3. To couple these two models together to build up a self-consistent microwave cavity plasma reactor model. The discharge excitation mechanisms and the microwave

power absorbed by the discharge will be investigated in detail by this model.

4. To verify that the models developed agree with experimental diagnostic measurements.

1.3 Outline

This dissertation is organized as shown in Figure 1-1. Chapter 2 presents the finite difference time-domain (FDTD) model which is used throughout this study for electromagnetic field simulation. The plasma conductivity models used for determining the microwave power absorbed by the discharges are developed in both the frequency domain and the time domain. Chapter 3 reviews the numerical models for plasma discharge simulation and presents the fluid plasma model used in this study for microwave discharge simulation. The physical background and numerical techniques used for model development are discussed. Chapter 4 provides the simulation results of transient state response of empty and loaded resonant cavities. The FDTD model is applied to investigate the characteristics of resonant cavities, such as the natural frequency response, cavity quality factor Q , and the electric field patterns. The resonant cavities which are investigated in this chapter include empty cavities operating in various resonant modes, cavities loaded with lossy materials and argon discharges, and a compact ECR ion source. Chapter 5 presents the simulation results of the electromagnetic behavior of a steady-state microwave cavity plasma reactor used for diamond film deposition. The method used to model the input power coupling is included in the FDTD model. Plasma discharges used here are assumed spatially uniform and with a constant temperature. Electric field and power absorption patterns under various input conduction are presented. Chapter 6

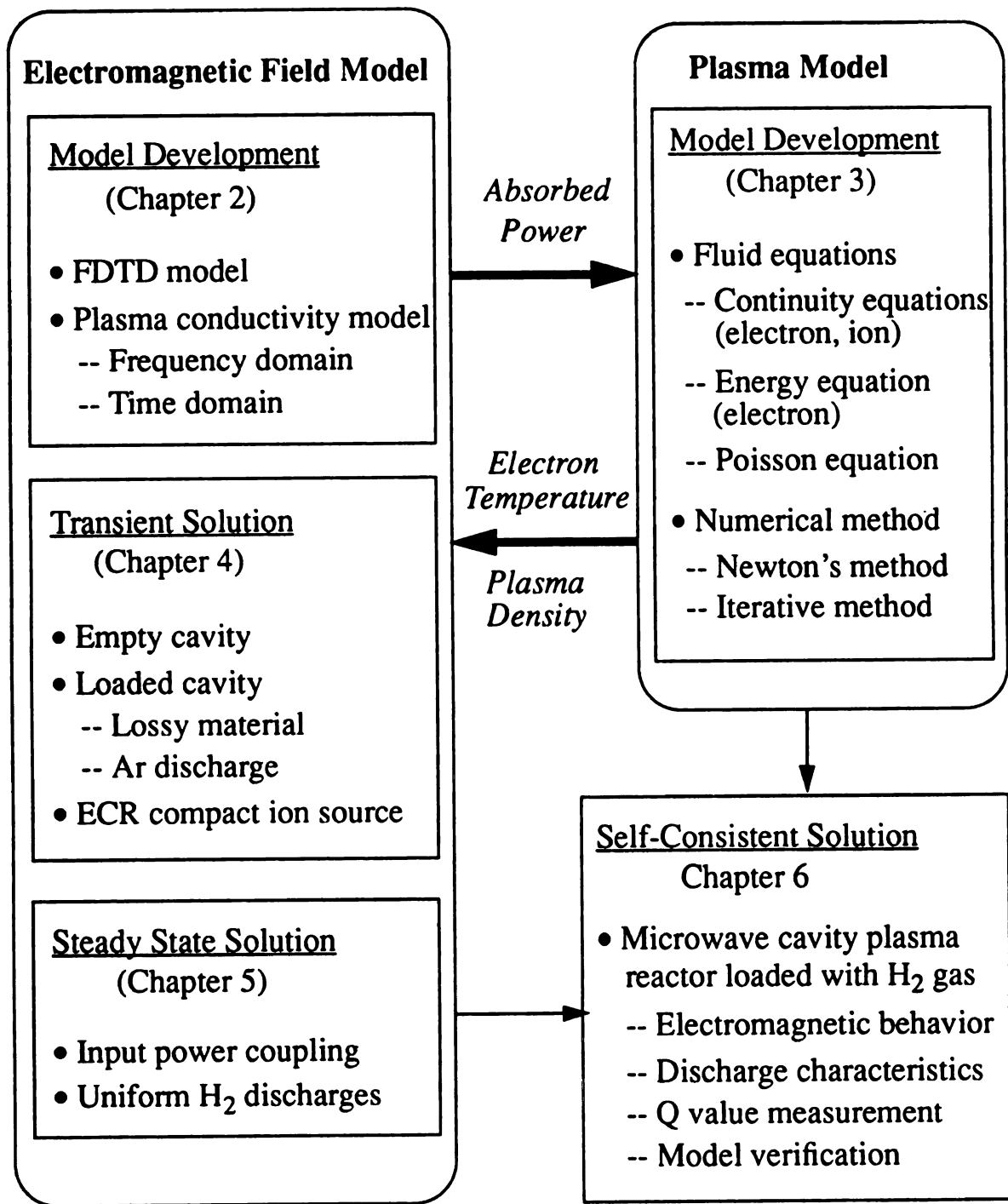


Figure 1-1: Overview diagram.

couples the FDTD electromagnetic field model with the fluid plasma model to provide a self-consistent microwave cavity plasma reactor model. The characteristics of discharges, such as densities and electron temperature, are investigated under various input conditions. The simulated cavity quality factor Q is compared with experimental results. Chapter 7 presents the conclusions and some speculations on future research and numerical model development for microwave cavity plasma reactor simulation.

Chapter 2

Electromagnetic Field Model

2.1 Introduction

Microwave fields serve as the energy source to excite and sustain the discharge inside cavity plasma reactors. The microwave energy is imparted into the cavity as shown in Figure 2-1 through an input electromagnetic coupling structure, such as a power coupling probe, and confined by the cavity walls which serve as the electromagnetic boundaries. When the exciting wave frequency and the cavity size match a certain resonant condition, the electromagnetic field will oscillate back and forth inside the cavity. These oscillating electromagnetic fields usually have specific field distribution patterns, or so called resonant modes, so the electromagnetic energy can focus on some local regions inside the cavity and breakdown the gases. These ionized gas species form the plasma discharges which are usually confined in a container, such as a quartz chamber. For an empty lossless cylindrical cavity, the electric field pattern, or the resonant cavity mode is well characterized by the size and resonant frequency. When a plasma is present, the plasma acts as a volume of lossy material loaded inside the cavity. It changes the resonant electric field patterns and the characteristics of the resonant cavity because microwave

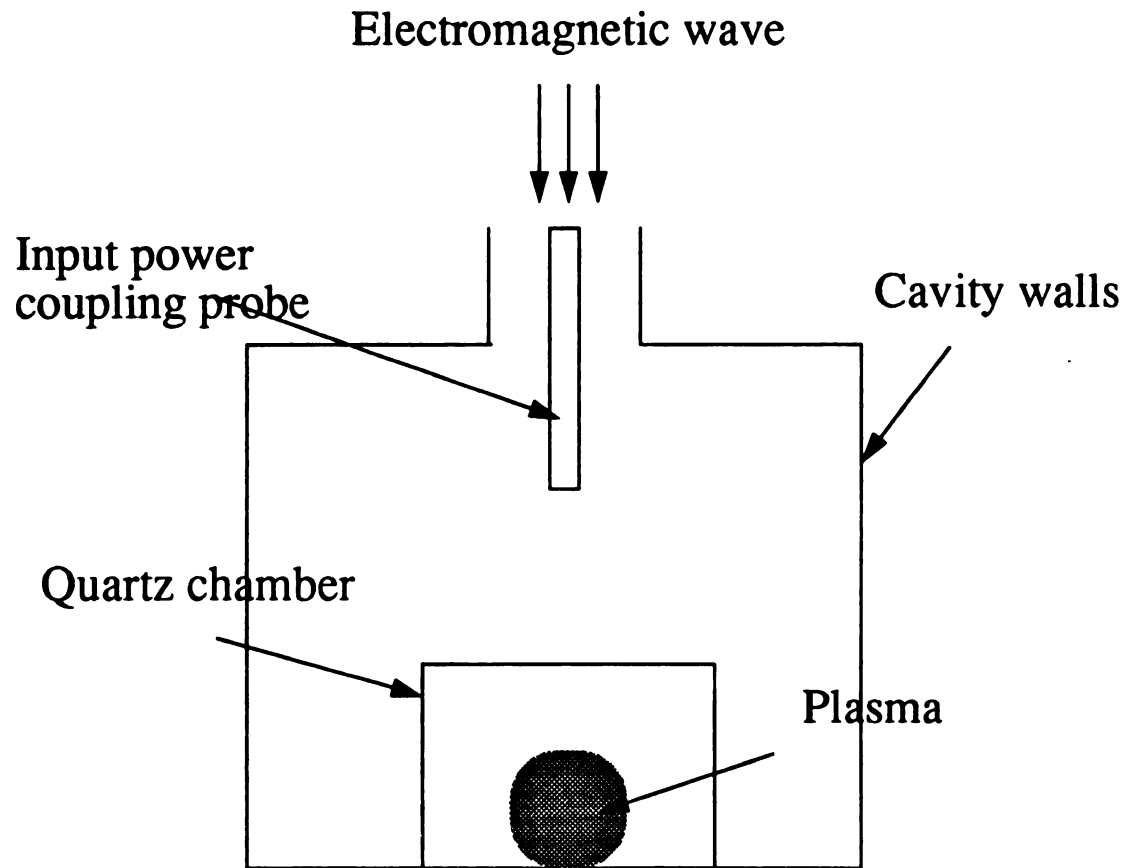


Figure 2-1: Schematic description of microwave discharge generation.

power is absorbed by the plasma. Moreover, since the plasma discharges are generated by the resonant electromagnetic fields, changes of the resonant behavior of the cavity also affect the characteristics of the discharges.

Since the resonant electromagnetic fields play a vital role for microwave discharge characterization, a mathematical model is required to describe the electromagnetic field behavior inside the plasma reactor system. In this chapter, the history of electromagnetic field models, both frequency domain or time domain modules, used for solving the resonant electromagnetic fields inside cavities are reviewed. The technique and background of the finite-difference time-domain method, which is used in this study to model the electromagnetic fields, are examined in detail. The method to implement the FDTD model in cylindrical coordinate is next described. Finally, the techniques used to solve electromagnetic field interactions with lossy materials and plasma discharges by coupling the FDTD model with appropriate conductivity models and by simultaneously solving the Maxwell's equations with the electron momentum transport equations are discussed.

2.2 Review of electromagnetic field model

One way to model the electromagnetic fields in a system is directly solving the Maxwell equations, which govern all well-behaved electromagnetic quantities. The Maxwell equations are

$$\begin{aligned}
\nabla \times \mathbf{E} &= -\mu \frac{\partial \mathbf{H}}{\partial t} \\
\nabla \times \mathbf{H} &= \epsilon \frac{\partial \mathbf{E}}{\partial t} + \mathbf{J} \\
\nabla \cdot \mathbf{E} &= \frac{\rho}{\epsilon} \\
\nabla \cdot \mathbf{H} &= 0
\end{aligned} \tag{2.1}$$

where \mathbf{E} is the electric field strength (Volts per meter), \mathbf{H} is the magnetic field strength (Amperes per meter), \mathbf{J} is the electric current density (Amperes per square meter), ρ is the electric charge density (Coulombs per cubic meter), ϵ is the electric permittivity of the medium (Coulombs per Volt-meter), and μ is the magnetic permeability of the medium (Volt-seconds per Ampere-meter). This differential form of Maxwell's equations can be solved either in the frequency domain or in the time domain.

2.2.1 Frequency domain

To solve the electromagnetic fields for a resonant cavity in the frequency domain, the electromagnetic quantities such as \mathbf{E} and \mathbf{H} are often assumed to be time-harmonic, i.e., their time dependence can be described by a periodic sinusoid and can be included in Maxwell's equations as a factor of the form $e^{j\omega t}$. Then, the Maxwell equations are converted to vector Helmholtz equations, and the E-field and the H-field are analytically solved in cylindrical coordinates in terms of a set of Bessel function type solutions [49]. The problem becomes an eigenvalue problem and the electromagnetic field solution inside the cavity can be expressed in terms of the eigenmode solutions such as the transverse magnetic mode (TM mode) and transverse electric mode (TE mode) solutions[49]. For a loaded cavity, i.e., different mediums filled inside the cavity, the electromagnetic fields

can be expanded in terms of a series of eigenmode solutions in each medium region, and appropriate boundary conditions are applied to ensure the electromagnetic continuity conditions are satisfied at the boundaries. A characteristic equation then be formed to determine the unknowns of the field solutions and can be solved either by graphical techniques or by numerically searching for the eigenvalues using a complex root finding method. This so called mode-matching or mode-expansion technique of solving time harmonic electromagnetic field solutions has been well established for studying the electromagnetic field behaviors inside coaxially loaded cylindrical waveguides and cylindrical resonant cavities loaded with lossy materials [8].

In terms of microwave cavity plasma reactors, the same techniques can be applied to investigate the microwave and plasma behavior by treating the discharges as lossy materials. J. R. Roger [6] used this technique to solve the electromagnetic behavior inside a cavity containing a quartz-tube-confined Ar plasma by treating the plasma as a lossy, homogeneous, isotropic, rod-shaped material. M. L. Passow, et al. [7] used the same electromagnetic analysis to determine the electron density, conductivity and collision frequency of a tube-contained air discharge. Modeling the inhomogeneous properties of plasmas using the mode-matching technique has been investigated by S. Offermann [9][10]. He coupled the Maxwell's equations together with an energy balance equation to solve the local dielectric constants of a high pressure Hg plasma. In order to reduce the complexity of this problem, only TM_{0m0} modes were considered, which reduced the field configuration to one dimension only.

Generally, there are two major difficulties in applying the frequency domain electromagnetic field solutions and mode-matching methods to solve the plasma-loaded

cavity problem. First, the plasma discharges inside microwave cavity reactors are inhomogeneous, anisotropic, and dispersive (the electric properties dependent on excitation frequency) in nature. This behavior makes the mode-matching method hard to apply to solve the plasma-loaded cavity problem. Another problem results from the geometry of the lossy load (discharge) or resonant cavity. If the load or cavity are geometrically complex, the number of boundary conditions needed for field solutions increases leading to intractable computer solutions.

2.2.2 Time domain

An alternative way to solve the electromagnetic field inside the cavity is to directly solve the time-dependent Maxwell's equations by using a finite-difference time-domain (FDTD) method. The FDTD technique was first proposed by K. S. Yee in 1966 to solve the interactions of electromagnetic waves with perfectly conducting material [11]. In his model, the time-dependent Maxwell's equations in a rectangular coordinate system were expanded to a set of six scalar equations:

$$\frac{\partial H_x}{\partial t} = \frac{1}{\mu} \left(\frac{\partial E_y}{\partial z} - \frac{\partial E_z}{\partial y} \right) \quad (2.2)$$

$$\frac{\partial H_y}{\partial t} = \frac{1}{\mu} \left(\frac{\partial E_z}{\partial x} - \frac{\partial E_x}{\partial z} \right) \quad (2.3)$$

$$\frac{\partial H_z}{\partial t} = \frac{1}{\mu} \left(\frac{\partial E_x}{\partial y} - \frac{\partial E_y}{\partial x} \right) \quad (2.4)$$

$$\frac{\partial E_x}{\partial t} = \frac{1}{\epsilon} \left(\frac{\partial H_z}{\partial y} - \frac{\partial H_y}{\partial z} \right) - \frac{J_x}{\epsilon} \quad (2.5)$$

$$\frac{\partial E_y}{\partial t} = \frac{1}{\epsilon} \left(\frac{\partial H_x}{\partial z} - \frac{\partial H_z}{\partial x} \right) - \frac{J_y}{\epsilon} \quad (2.6)$$

$$\frac{\partial E_z}{\partial t} = \frac{1}{\epsilon} \left(\frac{\partial H_y}{\partial x} - \frac{\partial H_x}{\partial y} \right) - \frac{J_z}{\epsilon} \quad (2.7)$$

These scalar equations were further discretized in both the time and space domain to get a set of finite difference equations:

$$\begin{aligned} H_x^{n+1/2} \left(i, j + \frac{1}{2}, k + \frac{1}{2} \right) &= H_x^{n-1/2} \left(i, j + \frac{1}{2}, k + \frac{1}{2} \right) + \frac{\Delta t}{\mu \left(i, j + \frac{1}{2}, k + \frac{1}{2} \right)} \\ &\times \left(\frac{E_y^n \left(i, j + \frac{1}{2}, k + 1 \right) - E_y^n \left(i, j + \frac{1}{2}, k \right)}{\Delta z} - \frac{E_z^n \left(i, j + 1, k + \frac{1}{2} \right) - E_z^n \left(i, j, k + \frac{1}{2} \right)}{\Delta y} \right) \end{aligned} \quad (2.8)$$

$$\begin{aligned} H_y^{n+1/2} \left(i + \frac{1}{2}, j, k + \frac{1}{2} \right) &= H_y^{n-1/2} \left(i + \frac{1}{2}, j, k + \frac{1}{2} \right) + \frac{\Delta t}{\mu \left(i + \frac{1}{2}, j, k + \frac{1}{2} \right)} \\ &\times \left(\frac{E_z^n \left(i + 1, j, k + \frac{1}{2} \right) - E_z^n \left(i, j, k + \frac{1}{2} \right)}{\Delta x} - \frac{E_x^n \left(i + \frac{1}{2}, j, k + 1 \right) - E_x^n \left(i + \frac{1}{2}, j, k \right)}{\Delta z} \right) \end{aligned} \quad (2.9)$$

$$\begin{aligned} H_z^{n+1/2} \left(i + \frac{1}{2}, j + \frac{1}{2}, k \right) &= H_z^{n-1/2} \left(i + \frac{1}{2}, j + \frac{1}{2}, k \right) + \frac{\Delta t}{\mu \left(i + \frac{1}{2}, j + \frac{1}{2}, k \right)} \\ &\times \left(\frac{E_x^n \left(i + \frac{1}{2}, j + 1, k \right) - E_x^n \left(i + \frac{1}{2}, j, k \right)}{\Delta y} - \frac{E_y^n \left(i + 1, j + \frac{1}{2}, k \right) - E_y^n \left(i, j + \frac{1}{2}, k \right)}{\Delta x} \right) \end{aligned} \quad (2.10)$$

$$\begin{aligned}
E_x^{n+1}\left(i+\frac{1}{2}, j, k\right) &= E_x^n\left(i+\frac{1}{2}, j, k\right) + \frac{\Delta t}{\epsilon\left(i+\frac{1}{2}, j, k\right)} \\
&\times \left(\frac{H_z^{n+1/2}\left(i+\frac{1}{2}, j+\frac{1}{2}, k\right) - H_z^{n+1/2}\left(i+\frac{1}{2}, j-\frac{1}{2}, k\right)}{\Delta y} \right. \\
&\left. - \frac{H_y^{n+1/2}\left(i+\frac{1}{2}, j, k+\frac{1}{2}\right) - H_y^{n+1/2}\left(i+\frac{1}{2}, j, k-\frac{1}{2}\right)}{\Delta z} - J_x^n\left(i+\frac{1}{2}, j, k\right) \right)
\end{aligned} \tag{2.11}$$

$$\begin{aligned}
E_y^{n+1}\left(i, j+\frac{1}{2}, k\right) &= E_y^n\left(i, j+\frac{1}{2}, k\right) + \frac{\Delta t}{\epsilon\left(i, j+\frac{1}{2}, k\right)} \\
&\times \left(\frac{H_x^{n+1/2}\left(i, j+\frac{1}{2}, k+\frac{1}{2}\right) - H_x^{n+1/2}\left(i, j+\frac{1}{2}, k-\frac{1}{2}\right)}{\Delta z} \right. \\
&\left. - \frac{H_z^{n+1/2}\left(i+\frac{1}{2}, j+\frac{1}{2}, k\right) - H_z^{n+1/2}\left(i-\frac{1}{2}, j+\frac{1}{2}, k\right)}{\Delta x} - J_y^n\left(i, j+\frac{1}{2}, k\right) \right)
\end{aligned} \tag{2.12}$$

$$\begin{aligned}
E_z^{n+1}\left(i, j, k+\frac{1}{2}\right) &= E_z^n\left(i, j, k+\frac{1}{2}\right) + \frac{\Delta t}{\epsilon\left(i, j, k+\frac{1}{2}\right)} \\
&\times \left(\frac{H_y^{n+1/2}\left(i+\frac{1}{2}, j, k+\frac{1}{2}\right) - H_y^{n+1/2}\left(i-\frac{1}{2}, j, k+\frac{1}{2}\right)}{\Delta x} \right. \\
&\left. - \frac{H_x^{n+1/2}\left(i, j+\frac{1}{2}, k+\frac{1}{2}\right) - H_x^{n+1/2}\left(i, j-\frac{1}{2}, k+\frac{1}{2}\right)}{\Delta y} - J_z^n\left(i, j, k+\frac{1}{2}\right) \right)
\end{aligned} \tag{2.13}$$

where (i, j, k) denotes a grid point in space and n denotes the time step, Δx , Δy , and Δz are the space grid unit in x, y, and z directions, and Δt is the time step. These field components in a unit cell are assigned in an interleaved manner similar to that shown in Figure 2-2. With the system of equations, (2.8) to (2.13), the new value of a field vector component at any grid point (e.g. E_x^n), depends only on its previous value (e.g. E_x^{n-1}) and the value of

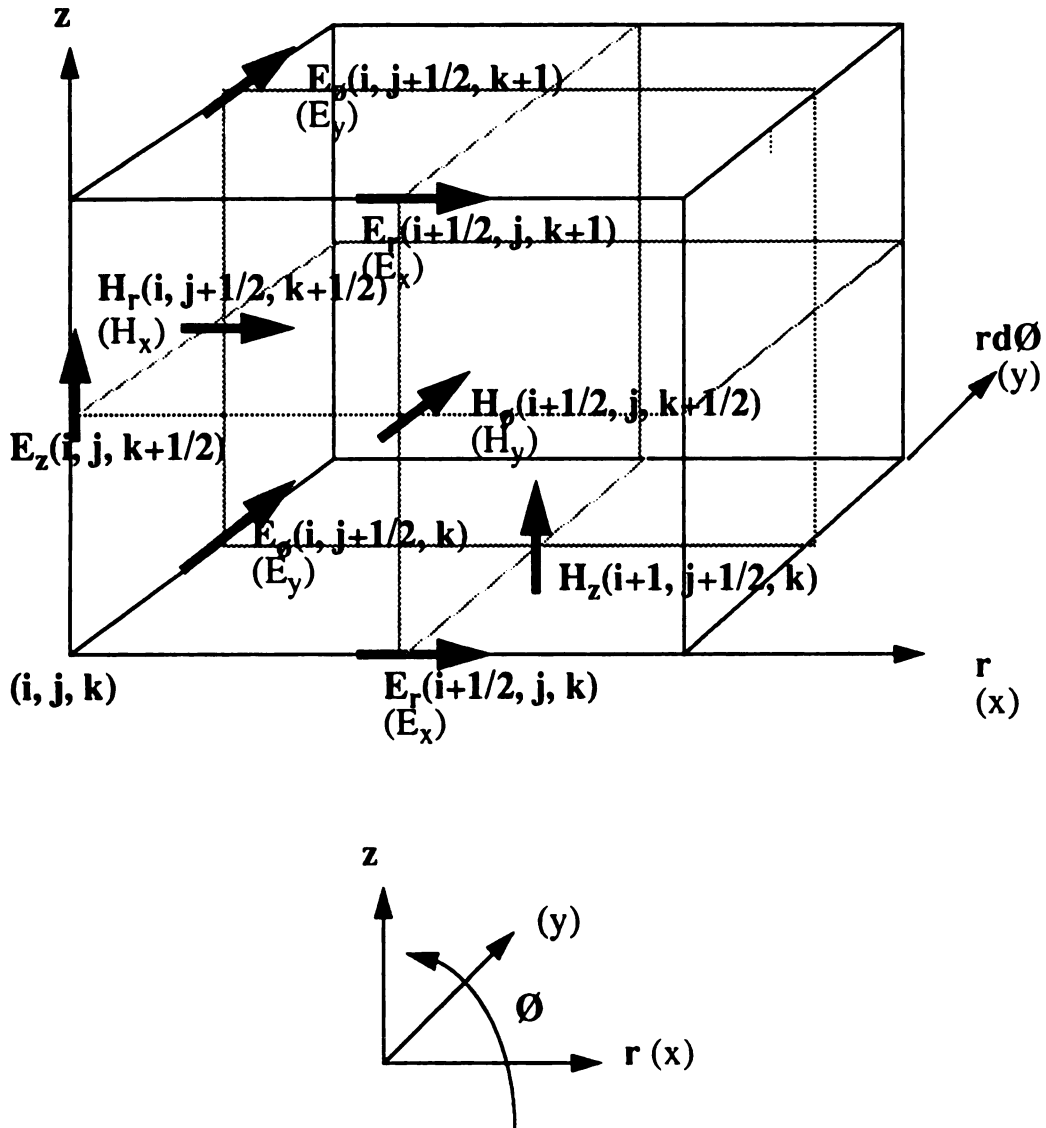


Figure 2-2: A FDTD unit cell in three-dimensional cylindrical coordinates.

the components of the other field vector at the adjacent point, which are perpendicular to it (e.g. $H_y^{n+1/2}$ and $H_z^{n+1/2}$). Therefore, with appropriate initial and boundary conditions, the electromagnetic fields on the grid points of the space mesh can be evaluated in time domain at alternate half-time steps (leapfrog method). By the stagger mesh arrangement in space and by the leapfrog time marching method, as shown in Figure 2-3, the numerical solutions of the FDTD model can achieve second order accuracy both in time and space [55].

This method has been used extensively to investigate the electromagnetic wave scattering phenomenon with dielectric or conducting objects. R. Holland, et. al., developed a three-dimensional computer code based on the FDTD method, to solve the electromagnetic pulse field scattering and surface currents for an aircraft [12]. Steady-state, sinusoidal electromagnetic scattering and penetration problems were investigated by A. Taflov, et. al., using the FDTD method for arbitrary metal or dielectric structures [13][14]. The electromagnetic power deposition in a human body has also been simulated by the FDTD method [17][18]. The model of the human body is an anatomically based model, which is an inhomogeneous, human shaped structure and composed of different types of tissues. Each tissue is assigned a set of specific dielectric constant and conductivity values, which can be used to determine the electromagnetic power absorbed by the tissue [19].

By using the Fourier Transform technique, the results of the FDTD method can be used to calculate the parameters in the frequency domain. This technique has been applied to analyze the characteristics of microstrips, waveguides, as well as, resonant cavities [20]-[26]. X. Zhang et. al. [20][21] use the FDTD method with Gaussian pulse excitation,

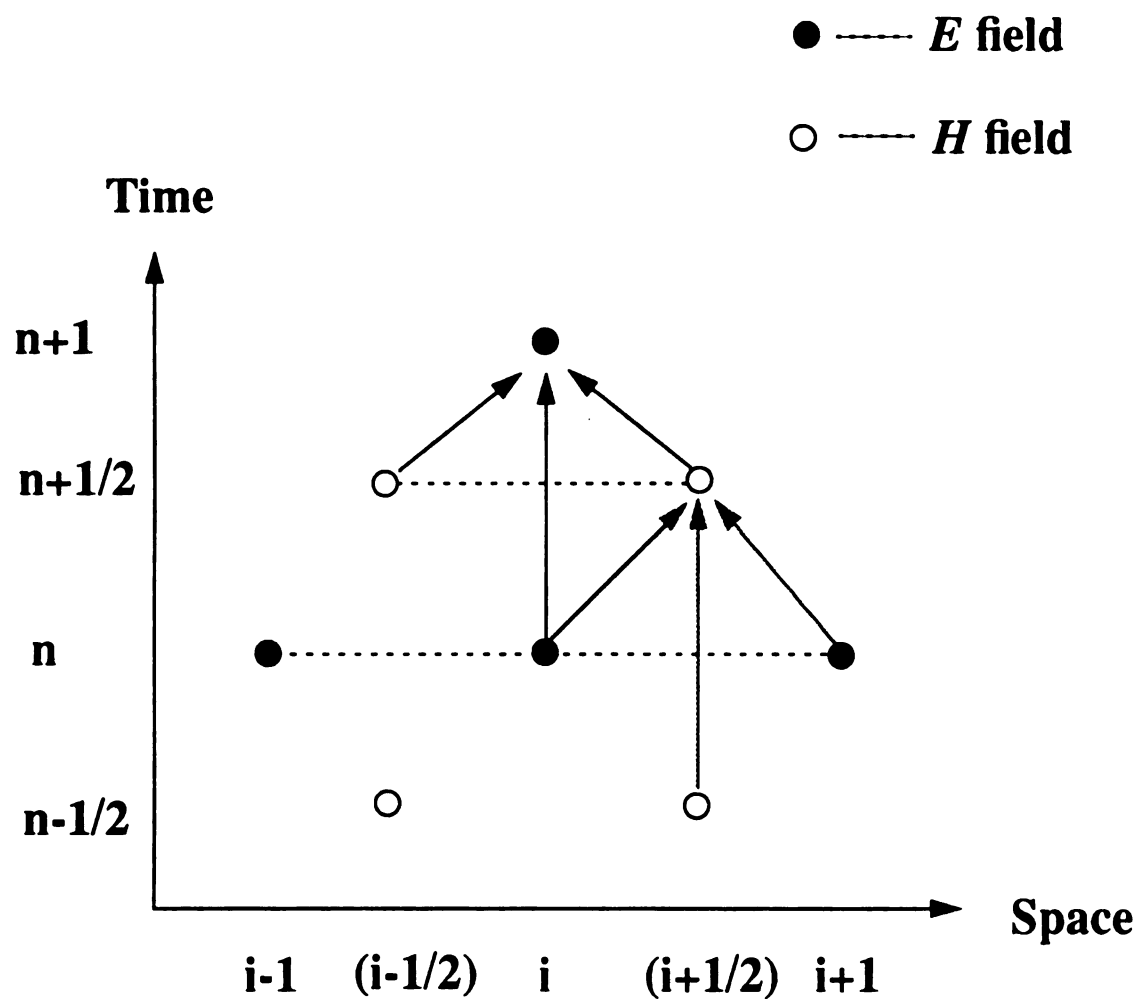


Figure 2-3: Leap-frog scheme.

which provides a wide band of frequency, to investigate the dispersive characteristics and discontinuity of microstrips. In terms of resonant cavities, D. H. Choi, et al., used the FDTD method and discrete Fourier transformation (DFT) techniques to solve three dimensional eigenvalue problems of inhomogeneous rectangular resonators [24]. The steady-state FDTD solution was treated as a time-harmonic function, from which the eigenvalues (resonant frequencies) were extracted by a discrete Fourier Transform technique given by

$$S(f) = \sum_n F^n(i_0, j_0, k_0) \exp(-j2\pi snf) \quad (2.14)$$

where S is the frequency (f) response spectrum, F is the FDTD solution at grid point (i_0, j_0, k_0) of the n^{th} iteration, and s is the stability factor. The same method was also used by A. Navarro, et. al., [25] to calculate the resonant frequencies of TE_0 and TM_0 mode cylindrical cavities with a axially symmetric dielectric load at the base. The FDTD method was also applied to simulate the microwave interactions with materials inside a resonant cavity. M. F. Iskander, et al., [26] used the FDTD method to simulate the sintering process of ceramics inside a rectangular, single mode microwave cavity. They provided a model which utilized a realistic wave excitation arrangement to improve the calculation of the cavity Q and the shift in resonant frequency. The steady state spatial electric field distributions were solved for both empty and loaded resonant cavities. The power absorption for different materials loaded inside the resonant cavity under different operating conditions was also calculated and analyzed.

There are several advantages of using the FDTD method to simulate the

electromagnetic field behavior for a plasma loaded resonant cavity. First, it is easy to implement for complicated loads (like plasmas), because spatially varying dielectric parameters can be assigned using grid points. Second, complex simulation structure, such as the discharge or cavity reactor geometry, can be solved by the FDTD method by using appropriate grid structures. Moreover, most of the plasma numerical models, both particle and fluid models, can be easily coupled to the FDTD model because both are in the time domain. Therefore, the FDTD method has great potential to solve the electromagnetic fields inside a discharge loaded cavity.

2.3 FDTD model implementation in cylindrical coordinates

As mentioned above, the finite-difference time-domain (FDTD) method is a good choice for solving the electromagnetic fields inside a plasma loaded cavity. The FDTD method used in this dissertation is adopted from Yee's algorithm [11] and transferred into three-dimensional cylindrical coordinates. In cylindrical coordinates, (2.1) can be expanded as six scalar equations given by

$$\frac{\partial H_r}{\partial t} = \frac{1}{\mu} \left(\frac{\partial E_\phi}{\partial z} - \frac{1}{r} \frac{\partial E_z}{\partial \phi} \right) \quad (2.15)$$

$$\frac{\partial H_\phi}{\partial t} = \frac{1}{\mu} \left(\frac{\partial E_z}{\partial r} - \frac{\partial E_r}{\partial z} \right) \quad (2.16)$$

$$\frac{\partial H_z}{\partial t} = \frac{1}{\mu} \left[\frac{1}{r} \frac{\partial E_r}{\partial \phi} - \frac{1}{r} \frac{\partial}{\partial r} (r E_\phi) \right] \quad (2.17)$$

$$\frac{\partial E_r}{\partial t} = \frac{1}{\epsilon} \left(\frac{1}{r} \frac{\partial H_z}{\partial \phi} - \frac{\partial H_\phi}{\partial z} \right) - \frac{J_r}{\epsilon} \quad (2.18)$$

$$\frac{\partial E_\phi}{\partial t} = \frac{1}{\epsilon} \left(\frac{\partial H_r}{\partial z} - \frac{\partial H_z}{\partial r} \right) - \frac{J_\phi}{\epsilon} \quad (2.19)$$

$$\frac{\partial E_z}{\partial t} = \frac{1}{\epsilon} \left[\frac{1}{r} \frac{\partial}{\partial r} (r H_\phi) - \frac{1}{r} \frac{\partial H_r}{\partial \phi} \right] - \frac{J_z}{\epsilon} . \quad (2.20)$$

These six differential equations can be discretized in both time and space domain by the central finite difference method. The resulting finite difference equations in cylindrical coordinate are:

$$H_r^{n+1/2} \left(i, j + \frac{1}{2}, k + \frac{1}{2} \right) = H_r^{n-1/2} \left(i, j + \frac{1}{2}, k + \frac{1}{2} \right) + \frac{\Delta t}{\mu \left(i, j + \frac{1}{2}, k + \frac{1}{2} \right)} \times \left[\frac{E_\phi^n \left(i, j + \frac{1}{2}, k + 1 \right) - E_\phi^n \left(i, j + \frac{1}{2}, k \right)}{\Delta z} - \frac{E_z^n \left(i, j + 1, k + \frac{1}{2} \right) - E_z^n \left(i, j, k + \frac{1}{2} \right)}{r_i (\Delta \phi)} \right] \quad (2.21)$$

$$H_\phi^{n+1/2} \left(i + \frac{1}{2}, j, k + \frac{1}{2} \right) = H_\phi^{n-1/2} \left(i + \frac{1}{2}, j, k + \frac{1}{2} \right) + \frac{\Delta t}{\mu \left(i + \frac{1}{2}, j, k + \frac{1}{2} \right)} \times \left[\frac{E_z^n \left(i + 1, j, k + \frac{1}{2} \right) - E_z^n \left(i, j, k + \frac{1}{2} \right)}{\Delta r} - \frac{E_r^n \left(i + \frac{1}{2}, j, k + 1 \right) - E_r^n \left(i + \frac{1}{2}, j, k \right)}{\Delta z} \right] \quad (2.22)$$

$$\begin{aligned}
H_z^{n+1/2}\left(i+\frac{1}{2}, j+\frac{1}{2}, k\right) &= H_z^{n-1/2}\left(i+\frac{1}{2}, j+\frac{1}{2}, k\right) + \frac{2\Delta t}{\mu\left(i+\frac{1}{2}, j+\frac{1}{2}, k+1\right)} \\
&\times \left[\frac{\frac{r_{i+1}-r_i}{2} \times \frac{E_r^n\left(i+\frac{1}{2}, j+1, k\right) - E_r^n\left(i+\frac{1}{2}, j, k\right)}{\Delta\phi}}{r_{i+1}^2 - r_i^2} \right. \\
&\quad \left. - \frac{r_{i+1}E_\phi^n\left(i+1, j+\frac{1}{2}, k\right) - r_iE_\phi^n\left(i, j+\frac{1}{2}, k\right)}{r_{i+1}^2 - r_i^2} \right] \quad (2.23)
\end{aligned}$$

$$\begin{aligned}
E_r^{n+1}\left(i+\frac{1}{2}, j, k\right) &= E_r^n\left(i+\frac{1}{2}, j, k\right) + \frac{\Delta t}{\varepsilon\left(i+\frac{1}{2}, j, k\right)} \\
&\times \left(\frac{H_z^{n+1/2}\left(i+\frac{1}{2}, j+\frac{1}{2}, k\right) - H_z^{n+1/2}\left(i+\frac{1}{2}, j-\frac{1}{2}, k\right)}{r_{i+1/2}\Delta\phi} \right. \\
&\quad \times \frac{H_\phi^{n+1/2}\left(i+\frac{1}{2}, j, k+\frac{1}{2}\right) - H_\phi^{n+1/2}\left(i+\frac{1}{2}, j, k-\frac{1}{2}\right)}{\Delta z} \\
&\quad \left. - J_r^n\left(i+\frac{1}{2}, j, k\right) \right) \quad (2.24)
\end{aligned}$$

$$\begin{aligned}
E_\phi^{n+1}\left(i, j+\frac{1}{2}, k\right) &= E_\phi^n\left(i, j+\frac{1}{2}, k\right) + \frac{\Delta t}{\varepsilon\left(i, j+\frac{1}{2}, k\right)} \\
&\times \left(\frac{H_r^{n+1/2}\left(i, j+\frac{1}{2}, k+\frac{1}{2}\right) - H_r^{n+1/2}\left(i, j+\frac{1}{2}, k-\frac{1}{2}\right)}{\Delta z} \right. \\
&\quad \times \frac{H_z^{n+1/2}\left(i+\frac{1}{2}, j+\frac{1}{2}, k\right) - H_z^{n+1/2}\left(i-\frac{1}{2}, j+\frac{1}{2}, k\right)}{r_{i+1/2} - r_{i-1/2}} \\
&\quad \left. - J_\phi^n\left(i, j+\frac{1}{2}, k\right) \right) \quad (2.25)
\end{aligned}$$

$$E_z^{n+1}\left(i, j, k + \frac{1}{2}\right) = E_z^n\left(i, j, k + \frac{1}{2}\right) + \frac{\Delta t}{\epsilon\left(i, j, k + \frac{1}{2}\right)} \times \left(\frac{r_{i+1/2} H_\phi^{n+1/2}\left(i + \frac{1}{2}, j, k + \frac{1}{2}\right) - r_{i-1/2} H_\phi^{n+1/2}\left(i - \frac{1}{2}, j, k + \frac{1}{2}\right)}{r_{i+1/2}^2 - r_{i-1/2}^2} \right. \\ \times \left. \frac{r_{i+1/2} - r_{i-1/2}}{r_{i+1/2}^2 - r_{i-1/2}^2} \times \frac{H_r^{n+1/2}\left(i, j + \frac{1}{2}, k + \frac{1}{2}\right) - H_r^{n+1/2}\left(i, j - \frac{1}{2}, k + \frac{1}{2}\right)}{\Delta\phi} - J_z^n\left(i, j, k + \frac{1}{2}\right) \right) \quad (2.26)$$

where n is the time index, i, j, k are space indexes, Δt is the time step, Δr , $\Delta\phi$ and Δz are the dimensions of the unit cell in r , ϕ and z direction, and r_{index} is position in r direction. Similar to rectangular coordinates, the six field locations in cylindrical coordinates are assigned to be interleaved in space to satisfy the continuity of tangential field components, as shown in Figure 2-2. If the dielectric parameters, such as permittivity ϵ and permeability μ , are space dependent, appropriate values are assigned to lattice points for each field component. Therefore, inhomogenous, anisotropic, or arbitrary shape materials can be easily handled by the FDTD model.

If the simulation domain is ϕ symmetry, such as the TM_0 mode resonant cavity problem, the three dimensional FDTD model can be reduced to a two dimensional model by neglecting all the variation in the ϕ direction, and the index (i, j, k) in (2.21) to (2.26) reduce to (i, k) only. The discretized two dimensional Maxwell's equations by assuming ϕ symmetry can be rewritten as:

$$H_r^{n+1/2}\left(i, k + \frac{1}{2}\right) = H_r^{n-1/2}\left(i, k + \frac{1}{2}\right) \times \frac{\Delta t}{\mu\left(i, k + \frac{1}{2}\right)} \left[\frac{E_\phi^n(i, k+1) - E_\phi^n(i, k)}{\Delta z} \right] \quad (2.27)$$

$$H_\phi^{n+1/2}\left(i + \frac{1}{2}, k + \frac{1}{2}\right) = H_\phi^{n-1/2}\left(i + \frac{1}{2}, k + \frac{1}{2}\right) + \frac{\Delta t}{\mu\left(i + \frac{1}{2}, k + \frac{1}{2}\right)} \times \left[\frac{E_z^n\left(i + 1, k + \frac{1}{2}\right) - E_z^n\left(i, k + \frac{1}{2}\right)}{\Delta r} \right] \quad (2.28)$$

$$H_z^{n+1/2}\left(i + \frac{1}{2}, k\right) = H_z^{n-1/2}\left(i + \frac{1}{2}, k\right) + \frac{2\Delta t}{\mu\left(i + \frac{1}{2}, k + 1\right)} \times \left[-\frac{r_{i+1}E_\phi^n(i+1, k) - r_iE_\phi^n(i, k)}{r_{i+1}^2 - r_i^2} \right] \quad (2.29)$$

$$E_r^{n+1}\left(i + \frac{1}{2}, k\right) = E_r^n\left(i + \frac{1}{2}, k\right) + \frac{\Delta t}{\varepsilon\left(i + \frac{1}{2}, k\right)} \times \left(-\frac{H_\phi^{n+1/2}\left(i + \frac{1}{2}, k + \frac{1}{2}\right) - H_\phi^{n+1/2}\left(i + \frac{1}{2}, k - \frac{1}{2}\right)}{\Delta z} - J_r^n\left(i + \frac{1}{2}, k\right) \right) \quad (2.30)$$

$$E_\phi^{n+1}(i, k) = E_\phi^n(i, k) + \frac{\Delta t}{\varepsilon(i, k)} \times \left(\frac{H_r^{n+1/2}\left(i, k + \frac{1}{2}\right) - H_r^{n+1/2}\left(i, k - \frac{1}{2}\right)}{\Delta z} - \frac{H_z^{n+1/2}\left(i + \frac{1}{2}, k\right) - H_z^{n+1/2}\left(i - \frac{1}{2}, k\right)}{r_{i+1/2} - r_{i-1/2}} - J_\phi^n(i, k) \right) \quad (2.31)$$

$$E_z^{n+1}\left(i, k + \frac{1}{2}\right) = E_z^n\left(i, k + \frac{1}{2}\right) + \frac{\Delta t}{\epsilon\left(i, k + \frac{1}{2}\right)} \times \left[\frac{r_{i+1/2} H_\phi^{n+1/2}\left(i + \frac{1}{2}, k + \frac{1}{2}\right) - r_{i-1/2} H_\phi^{n+1/2}\left(i - \frac{1}{2}, k + \frac{1}{2}\right)}{r_{i+1/2}^2 - r_{i-1/2}^2} - J_z^n\left(i, k + \frac{1}{2}\right) \right] \quad (2.32)$$

The time step in (2.21) to (2.26) and (2.27) to (2.32) is determined by the cell size and must satisfy the stability condition [13]:

$$\Delta t \leq \frac{\delta_{min}}{v_{max}\sqrt{3}} \text{ for three dimensions} \quad (2.33)$$

and

$$\Delta t \leq \frac{\delta_{min}}{v_{max}\sqrt{2}} \text{ for two dimensions} \quad (2.34)$$

where δ_{min} is the smallest space grid size, and v_{max} is the maximum phase velocity within the model. v_{max} is typically selected as the speed of light, c .

2.4 Conductivity models for FDTD model implementation

For the resonant cavity simulation, the current density (J_x , J_y , J_z) in equations (2.24) to (2.26) represents the current density which is induced by the applied electromagnetic fields. It plays an important role in the FDTD model because it describes the electromagnetic power absorbed by the loaded material or cavity wall. For an empty or perfect dielectric (loseless) medium loaded cavity with perfect conducting walls, the

current density is zero and there is no power loss in the cavity. When losses occur due to the presence of a lossy medium, such as a plasma load, the power density P absorbed by the medium is:

$$P(\mathbf{r}, t) = \mathbf{J}(\mathbf{r}, t) \bullet \mathbf{E}(\mathbf{r}, t) . \quad (2.35)$$

The current density \mathbf{J} can be determined by using an appropriate conductivity model for lossy materials or plasmas. The plasma conductivity model can be established in the frequency (time-harmonic) domain as a fixed conductivity or in the time domain by solving the momentum transport equation of electrons, where $\mathbf{J} = en\mathbf{v}$. Additionally, the current density \mathbf{J} also can be calculated by averaging over the particle velocities in a particle type plasma simulation.

2.4.1 Conductivity model for non-dispersive lossy materials

When electromagnetic fields interact with a non-dispersive (the dielectric parameters are independent of frequency) lossy material, the current density (J_r, J_ϕ, J_z) in (2.24) to (2.26) can be evaluated using the conductivity of the load, i.e.

$$J_m(i, j, k) = \sigma(i, j, k) E_m(i, j, k) , \quad m = r, \phi, z \quad (2.36)$$

where i, j , and k denote the grid indices in the r, ϕ , and z directions, respectively. In this case, like ϵ and μ , σ can be assigned to each lattice point to calculate the current density. By substituting (2.36) into (2.24) to (2.26), the equation in center finite difference form for E_r for example, can be rewritten as

$$\begin{aligned}
E_r^{n+1}\left(i + \frac{1}{2}, j, k\right) = & CA_r\left(i + \frac{1}{2}, j, k\right)E_r^n\left(i + \frac{1}{2}, j, k\right) + \frac{\Delta t}{\varepsilon\left(i + \frac{1}{2}, j, k\right)} \\
& \times \left(\frac{H_z^{n+1/2}\left(i + \frac{1}{2}, j + \frac{1}{2}, k\right) - H_z^{n+1/2}\left(i + \frac{1}{2}, j - \frac{1}{2}, k\right)}{r_{i+1/2}\Delta\phi} \right. \\
& \left. - \frac{H_\phi^{n+1/2}\left(i + \frac{1}{2}, j, k + \frac{1}{2}\right) - H_\phi^{n+1/2}\left(i + \frac{1}{2}, j, k - \frac{1}{2}\right)}{\Delta z} \right)
\end{aligned} \tag{2.37}$$

where

$$CA_r\left(i + \frac{1}{2}, j, k\right) = \left(1 - \frac{\sigma_r\left(i + \frac{1}{2}, j, k\right)\Delta t}{2\varepsilon_r\left(i + \frac{1}{2}, j, k\right)}\right) \times \left(1 + \frac{\sigma_r\left(i + \frac{1}{2}, j, k\right)\Delta t}{2\varepsilon_r\left(i + \frac{1}{2}, j, k\right)}\right)^{-1} \tag{2.38}$$

Similarly, E_ϕ and E_z can be rewritten in this manner.

2.4.2 Plasma conductivity model

Plasma discharges can also be viewed as lossy materials, and microwave power absorbed by the plasma can be described using a plasma conductivity model. The conductivity of a plasma can be derived by solving the macroscopic motion of the electrons under the influence of applied forces and particle collision processes. The microscopic electron motion can be described by the electron momentum transport equation, i.e., the Langevin equation [50] under the assumption of the cold plasma:

$$m_e \frac{d}{dt} \mathbf{v}(\mathbf{r}, t) = -e(\mathbf{E}(\mathbf{r}, t) + \mathbf{v}(\mathbf{r}, t) \times \mathbf{B}(\mathbf{r}, t)) - m_e \nu_{eff}(\mathbf{r}, t) \mathbf{v}(\mathbf{r}, t) \tag{2.39}$$

where \mathbf{v} is the average electron velocity, \mathbf{E} is the applied electric field, \mathbf{B} is the applied

magnetic field, q is the electron charge, m_e is the electron mass, and ν_{eff} is the effective collision frequency which represents the elastic collision frequency between the electron and neutrals for momentum transfer. This equation assumes that the electrons are free to move in a stationary uniform background of ions and neutral which provide a viscous damping force to the motion of the electrons. It is suitable for partially ionized and elastic collision dominate discharges such as those of interest in this study.

From (2.39) the current density can be determined as

$$\mathbf{J}(\mathbf{r}, t) = -en_e(\mathbf{r}, t)\mathbf{v}(\mathbf{r}, t) \quad (2.40)$$

where n_e is the electron density. By equation (2.39) and (2.40), the characteristics of the plasma (n_e and ν_{eff}) can be coupled with the \mathbf{J} quantity in FDTD model to investigate the electromagnetic excitation of discharges inside microwave cavity plasma reactor. Equation (2.39) can be solved and modeled in either the time harmonic domain or the time domain.

2.4.2.1 Time harmonic domain solution

In the time harmonic domain, the applied electric field is considered oscillating harmonically with time, $\mathbf{E} = \mathbf{E}_0 e^{j\omega t}$. For unmagnetized plasmas, the steady state solution for \mathbf{v} must have this time dependence given from (2.39)

$$j\omega m_e \mathbf{v} = -e\mathbf{E} - m\nu_{eff}\mathbf{v} \quad (2.41)$$

therefore,

$$\mathbf{v} = \frac{-e\mathbf{E}}{m_e(\nu_{eff} + j\omega)} = \frac{-e\mathbf{E}}{m_e} \left(\frac{\nu_{eff}}{\nu_{eff}^2 + \omega^2} - j \frac{\omega}{\nu_{eff}^2 + \omega^2} \right). \quad (2.42)$$

From (2.40), the current density is

$$\mathbf{J} = \sigma \mathbf{E} = -en_e \mathbf{v} \quad (2.43)$$

and the conductivity of an unmagnetized plasma is

$$\sigma = \frac{e^2 n_e}{m_e} \left(\frac{\nu_{eff}}{\nu_{eff}^2 + \omega^2} - j \frac{\omega}{\nu_{eff}^2 + \omega^2} \right). \quad (2.44)$$

Also, the dielectric parameter of an unmagnetized plasma can be written as

$$\begin{aligned} \epsilon &= \epsilon_0 \epsilon_r \\ \epsilon_r &= 1 - j \frac{\sigma}{\omega \epsilon_0} = \left(1 - \frac{\omega_p^2}{\nu_{eff}^2 + \omega^2} \right) + j \frac{\nu_{eff}}{\omega} \left(\frac{\omega_p^2}{\nu_{eff}^2 + \omega^2} \right) \end{aligned} \quad (2.45)$$

where ω_p is the plasma frequency, which is defined by [50]

$$\omega_p = \sqrt{\frac{n_e e^2}{m_e \epsilon_0}}. \quad (2.46)$$

The time-average electromagnetic power absorbed by the plasma can be expressed as [1]

$$\langle P \rangle_{abs}(\mathbf{r}) = \frac{1}{2} \text{Re}(\mathbf{E}(\mathbf{r}) \bullet (\sigma(\mathbf{r}) \mathbf{E}(\mathbf{r}))^*) \quad (2.47)$$

where P has the units of power density (Watt/m³). Substituting equations (2.43) and (2.44) into equation (2.47), the time-average-absorbed power density of an unmagnetized plasma is given by

$$\langle P \rangle_{abs}(r) = \frac{n_e e^2}{2m_e} \left(\frac{v_{eff}}{v_{eff}^2 + \omega^2} \right) |E(r)|^2 \quad (2.48)$$

where $|E(r)|$ is the magnitude of the electric field as a function of r . From above, the power absorbed by the discharge is proportional to the real part of the plasma conductivity, or the imaginary part of the plasma dielectric constant.

For magnetized plasmas, the conductivity is in a complex tensor form, which indicates the anisotropic properties of a magnetized plasma. By assuming the magnetic field \mathbf{B} exists only in the z direction, i.e., $\mathbf{B} = B_0 \mathbf{z}$, the relation of the current density to the applied electric field can be expressed as [50]:

$$\begin{bmatrix} J_x \\ J_y \\ J_z \end{bmatrix} = \begin{bmatrix} \sigma_{\perp} & -\sigma_x & 0 \\ \sigma_x & \sigma_{\perp} & 0 \\ 0 & 0 & \sigma_{||} \end{bmatrix} \begin{bmatrix} E_x \\ E_y \\ E_z \end{bmatrix} \quad (2.49)$$

where

$$\begin{aligned}
\sigma_{\perp} &= \frac{n_e e^2}{m_e} \frac{v_{eff} + j\omega}{(v_{eff} + j\omega)^2 + \omega_{ce}^2} \\
\sigma_x &= \frac{n_e e^2}{m_e} \frac{\omega_{ce}}{(v_{eff} + j\omega)^2 + \omega_{ce}^2} \\
\sigma_{||} &= \frac{n_e e^2}{m_e} \frac{1}{v_{eff} + j\omega}
\end{aligned} \tag{2.50}$$

ω_{ce} is defined as the electron cyclotron frequency, which is equal to eB_0/m_e .

Similarly, by substituting equations (2.49) and (2.50) into equation (2.47), the time-averaged power density absorbed by the magnetized plasma becomes:

$$\langle P \rangle_{abs}(r) = \frac{1}{2} \left(Re(\sigma_{\perp}) |E_{\perp}(r)|^2 + Re(\sigma_{||}) |E_{||}(r)|^2 \right) \tag{2.51}$$

where the symbol \perp means perpendicular to the static magnetic field (B_z), and $||$ means parallel to the static magnetic field (B_z). If the time-varying electric field is perpendicular to the static magnetic field only, the time-averaged power density absorbed by the plasma becomes:

$$\langle P \rangle_{abs}(r) = \frac{n_e e^2 v_{eff}}{4m_e} \times \left(\frac{1}{v_{eff}^2 + (\omega - \omega_{ce})^2} + \frac{1}{(v_{eff}^2 + (\omega + \omega_{ce})^2)} \right) |E(r)|^2 \tag{2.52}$$

Note that when $\omega \gg v_{eff}$ and $\omega_{ce} \sim \omega$, (2.52) represents the electron cyclotron heating mechanism.

The above conductivity expressions can be coupled with the FDTD method by assigning the calculated conductivity value at each grid point. This method can approximately provide the power absorption solutions of the plasmas. However, because

plasma discharges are dispersive in natural, i.e., its macroscopic dielectric parameters are dependent on its excitation frequency, these conductivity models expressed in frequency domain are highly dependent on the real exciting frequency. This will cause difficulties while applying them in time-domain simulations (such as the FDTD model) where the time variation of the electric fields may not be known before the simulation begins [16]. In this study, in order to not lose generality, the Maxwell's equations are solved self-consistently in the time domain with the electron momentum transport equation (2.39). The details are provided in the next section.

2.4.2.2 Time domain solution

To model the plasma conductivity due to an applied electric field in the time domain, ϵ and μ in the discretized Maxwell's equations (2.21) to (2.26) are set equal to ϵ_0 and μ_0 (dielectric parameters in vacuum or air), and the current density in equations (2.24) to (2.26) is evaluated using the electron momentum transport equation (2.40). To get the time domain solution of equation (2.40), the finite difference method is used to discretize this first order differential equation in time. Neglecting the static magnetic field, (2.40) becomes

$$v_{r,\phi,z}^n(i,j,k) = (1.0 - \Delta t \cdot \nu_{eff}(i,j,k)) \cdot v_{r,\phi,z}^{n-1}(i,j,k) - \frac{q\Delta t}{m_e} E_{r,\phi,z}^{n-1}(i,j,k) \quad (2.53)$$

and the current density is

$$J_{r,\phi,z}^n(i,j,k) = -qn_e(i,j,k) v_{r,\phi,z}^n(i,j,k) \quad (2.54)$$

where n denotes the time iteration count, Δt is the time step, and i, j, k denote the grid location. Equations (2.53) and (2.54) are solved simultaneously with equations (2.21) to (2.26). The absorbed power density can be solved directly by coupling (2.53) with (2.35).

From the above equations, the space-dependent current density \mathbf{J} is determined by the space-dependent discharge characteristics such as electron density n_e and effective collision frequency ν_{eff} . Moreover, the effective collision frequency which describes the momentum transfer due to electron-neutral elastic collisions is a function of electron energy distributions (electron temperature). For a complete microwave plasma excitation solution, the electron density and electron temperature must be solved self-consistently by using appropriate plasma models, such as fluid (continuum) or particle plasma models. These models used for solving the characteristics of plasma discharges are discussed in the next chapter.

2.5 Summary

The electromagnetic field model for this study was developed in this chapter. The model developed solves Maxwell's equations in two and three dimensional cylindrical coordinates using a FDTD technique. The microwave induced current density which determines the power absorption inside the cavity was described by using conductivity models. The methods developed to describe the conductivity of discharges included the solution of the electron momentum transport equation either in the frequency domain or in the time domain. This electromagnetic field model will be verified by the transient state simulation results of empty and loaded cavities in Chapter 4.

Chapter 3

Numerical Models of Plasma Discharges

3.1 Introduction

In this chapter, numerical models which describe the behavior of plasma discharges are presented and developed. First, the models used for plasma simulation in the literature are reviewed and the physical background of discharge transport behavior is discussed. Next, the fluid description of the plasma based on the moments of Boltzmann transport equation is derived. Finally, the numerical methods used for solving the fluid model description are introduced.

3.2 Review of plasma discharge models

Generally, for plasma-aided processing simulation, there are two major approaches to solve the transport behavior of discharges. One is the particle approach, which is done using the particle simulation technique which treats the plasma as a combination of particles (electrons, ions, and neutrals) and calculates the trajectories of many particles in time to obtain the macroscopic quantities of the plasma. The other one is the continuum (or fluid) approach, which treats the plasma as a fluid and solves the moment equations of the Boltzmann transport equation (BTE) which include the continuity equation,

momentum transport equation and energy transport equation of each plasma species by appropriate numerical techniques. The fluid models and particle models are sometimes combined together as a hybrid fluid/particle model to provide self-consistent solutions. These models are reviewed in this section.

3.2.1 Particle model

The particle models simulate the trajectories of particles inside the discharge as they move through a system under the influence of the applied fields and random scattering forces. If the number of simulated trajectories is large enough, the average results provide a good approximation of the particle transport behavior inside the discharges. There are two types of particle models used in plasma processing simulation. The first is a single particle Monte Carlo method, which precisely simulates a single particle trajectory and its collision events. It is usually used to solve the transport parameters such as mobility, diffusion coefficient and various collision rates of the plasma species. M. J. Kushner [31] and B. E. Thompson, et. al. [32] studied the secondary electrons phenomena and ion bombardment properties respectively in RF discharges by the Monte Carlo techniques. A similar technique was developed by J. I. Ullacia and J. P. McVittie [33], to perform a two-dimensional plasma etching simulation. The motion of electrons in applied magnetic fields has also been investigated using Monte Carlo methods by G. R. Govinda Raju [34] and T. E. Sheridan, et. al. [35].

The major problem of the single particle Monte Carlo methods for plasma simulation is the inclusion of the local electric field induced by charge densities variations. To overcome the above problem, a many-particle simulation method, particle-in-cell

method (PIC), is introduced in combination with the Monte Carlo collision method [47]. Originally, the PIC method was used in hot fully ionized collisionless bulk plasmas (especially for fusion plasmas) [36]. The defining characteristic of the PIC simulations is the method of calculating the force acting on each particle. The simulation region is divided into a number of cells and the resulting grid is used in the solution of a field equation (e.g. Poisson's equation) from which the force on each particle can be determined. Each simulation 'particle', also called a superparticle, is actually a group of charges with a specific charge density. The history of the development of the PIC method and the details of melding of PIC with Monte Carlo collision models was reviewed by C. K. Birdsall [36].

Recently, the PIC method merged with the Monte Carlo collision method has been used to model bounded, partially ionized, collisional discharges, which are used intensively in industrial applications. D. Vender and R. Boswell [37], M. Suerndra and D. B. Graves [38], H. W. Trombley et. al. [39], and R. W. Boswell and D. Vender [40] have used the PIC method together with the Monte Carlo method to investigate RF discharge behaviors for various operating conditions. T. A. Grotjohn [41] used a PIC/Monte Carlo particle model coupled with FDTD solutions of Maxwell's equations as mentioned in Chapter 2 to model a compact ECR ion source in the 2d3v domain. In this magnetized discharge simulation, the electron and ion trajectories were determined by the Lorentz force equation and elastic/inelastic collision events.

In many cases, the particle models are the most accurate techniques available for analyzing and simulating the plasma transport behaviors. Moreover, it is well suited for low pressure, ECR, and non-equilibrium discharge simulation. However, its time-

consuming nature when implemented in computer programs largely reduces its efficiency. This is especially unattractive for large simulation domains (\gg particle mean free path) and three dimensional (3d3v) simulations. Therefore, in this study, the microwave discharges are modeled based on fluid techniques.

3.2.2 Continuum (fluid) model

In continuum plasma models, the transport behavior of the plasma species are described by moment equation solutions of the Boltzmann transport equation, including the continuity equation, momentum transport equation, and energy transport equation. These moment equations are often combined with Poisson equation to provide self-consistent solutions. Under the assumption of a steady state thermal equilibrium existing in the system, the fluid model might be simplified to solve only the continuity equation and Poisson equation and becomes the drift-diffusion model. The details of these models will be discussed in next section.

Fluid models have been used in the simulation of capacitively coupled DC and RF discharges. The first global self-consistent continuum DC and RF discharge models were build up by D. Graves and K. F. Jensen [27]. They solved the electron and ion continuity equations, the Poisson's equation, and an energy conservation equation for electrons. Assuming collisionally dominated particle motion, the electron and ion momentum transport equations were reduced to expressions for particle flux incorporating mobilities and diffusivities. A finite-element method with mesh points was used for solving the equations. D. Graves later coupled an electron excitation term into this model to qualitatively examine the time and space dependence of rates of electron impact excitation

[28]. J. P. Boeuf added negative ions into the continuity equations, and analyzed the influence of frequency and gas composition (electropositive v.s. electronegative gas) on RF glow discharge properties [29]. A local equilibrium approximation was assumed, so the transport parameters were dependent on the local electric field. An implicit finite difference scheme was used for the numerical technique. The same fluid model and assumptions were extended to two-dimensional simulations for N_2 and SF_6 RF glow discharges by J. H. Tsai and C. Wu [30]. They used a more accurate flux-corrected transport method and a reconstructed fast-Fourier-transform technique to solve the continuity equations and Poisson's equation respectively.

The transport parameters and collision rates used in fluid plasma model are sometimes determined by Monte Carlo techniques. M. S. Barnes, et. al. [42] used this method to solve ion and electron continuity equations for RF glow discharge. In his later work, Barnes further coupled the Monte Carlo method with three moments of the Boltzmann transport equation for steady state RF discharge simulation [43]. The nonequilibrium characteristics of electron transport was taken into account by N. Sato and H. Tagashira [44] in their flux-corrected transport fluid model. In their study, the Monte Carlo simulation showed the electron transport properties were not in equilibrium with the local electrical field for SiH_4/H_2 mixture RF discharges.

For microwave ECR plasmas, due to the low operating pressure (0.1 mTorr to few mTorr), fluid models may no longer be valid. However, a direct application of a particle model (like PIC/MC) cost a lot of time for realistic ECR reactors, which normally require simulation in two (or three) dimensions. R. K. Porteous and D. B. Graves [45] developed a hybrid electron fluid-particle ion model for magnetically confined low pressure discharges

with cylindrical axisymmetry. Ions are treated as particles, which can travel in two dimensions under the combined influence of applied static magnetic fields and the self-consistent electric fields solved by Poisson's equation. Non-uniform grids were used ranging from 0.5 Debye lengths to 300 Debye lengths. Electrons were treated as a fluid, which were strongly magnetized and had only axial directional motion. A Maxwell-Boltzmann distribution was assumed and both the continuity and energy equations were solved for electrons. Power was directly deposited into electrons with an assumed profile. This work provide the possibility of treating a two-dimensional system which had a very small Debye length to system chamber length scale ratio.

Y. Weng and M. J. Kushner [46] used a hybrid Monte Carlo- fluid model to investigate the electron energy distributions in ECR discharges. The Monte Carlo simulation of the electron swarm was capable of resolving the electron-electron collisions and provided the details of electron energy distributions. This MC simulation was iteratively combined with a fluid model, which solved the electron and ion continuity equations, to calculate ambipolar electric fields. The electric field cycled back to the MC simulation and was included in the equations of motion for electrons. The microwave electric fields were assumed to be a plane wave with uniform amplitude as a function of radial position. The results of the fluid model for the ambipolar potential, though applied in low pressure, successfully agreed with experimental results.

Two major difficulties which arise while applying a continuum model for plasma simulation are: (1) If the pressure is low in the system, the collisions of particles are infrequent. The mean free path for the particles (especially electrons) becomes large, and in some case larger than the chamber dimensions. It is not suitable to apply fluid models

when the mean free paths are not the smallest characteristic length in the system. (2) For discharges with non-equilibrium or large density (or energy) gradient regions, e.g. sheath or ECR regions, the transport parameters and rates used in the moments of Boltzmann's equation are difficult to determined. The fluid model is inappropriate to apply under these conditions.

3.3 Model development

The fluid plasma model used in this study is established in this section. The physical background for model development, such as the concept of distribution function and Boltzmann transport equations, is discussed. The moments of Boltzmann transport equations are derived in detail. Finally, the moment equations used in the fluid plasma model are introduced.

3.3.1 Distribution function

Plasmas consist of several categories of particles, including the electrons, ions, and neutral species. In order to give a complete specification of the properties of this system of particles, it is necessary to know the phase space location, i.e., the position \mathbf{r} and velocity \mathbf{v} , of each particle. The number of particles in an elemental volume of the phase space at any instant of time can be statistically specified by a distribution function $f(\mathbf{r}, \mathbf{v}, t)$. Then, the density of particles $n(\mathbf{r}, t)$ at a given position inside the system can be determined by integrating the distribution function over all velocity volume as

$$n(\mathbf{r}, t) = \int f(\mathbf{r}, \mathbf{v}, t) d\mathbf{v}. \quad (3.1)$$

Then, the average quantity ϕ of the entire collection of particles is given by

$$\langle \phi \rangle = \frac{1}{n(r, t)} \int \phi(r, v, t) f(r, v, t) dv . \quad (3.2)$$

For example, the average velocity $\langle v(r, t) \rangle$, and energy $\langle \xi(r, t) \rangle$ of all particles are

$$\langle v(r, t) \rangle = \frac{1}{n(r, t)} \int v(r, t) f(r, v, t) dv \quad (3.3)$$

$$\langle \xi(r, t) \rangle = \frac{1}{n(r, t)} \int \frac{1}{2} m v^2 f(r, v, t) dv \quad (3.4)$$

respectively. Thus, the distribution function f can be described by the macroscopic quantities (also called moments) defined by (3.1), (3.3) and (3.4) as shown in Figure 3-1. The area under the distribution function f is described by the density n , the displacement of f described by the average velocity $\langle v \rangle$, and the width of f is described by the average energy $\langle \xi \rangle$.

If the system is in thermodynamic equilibrium and not subject to any external force, the distribution function f becomes the Maxwellian distribution

$$f(r, v, t) = n(r, t) \left(\frac{m}{2\pi k_B T} \right)^{3/2} e^{-mv^2/2k_B T} \quad (3.5)$$

which is isotropic in velocity space. Sometimes, it is convenient to express f as a energy distribution

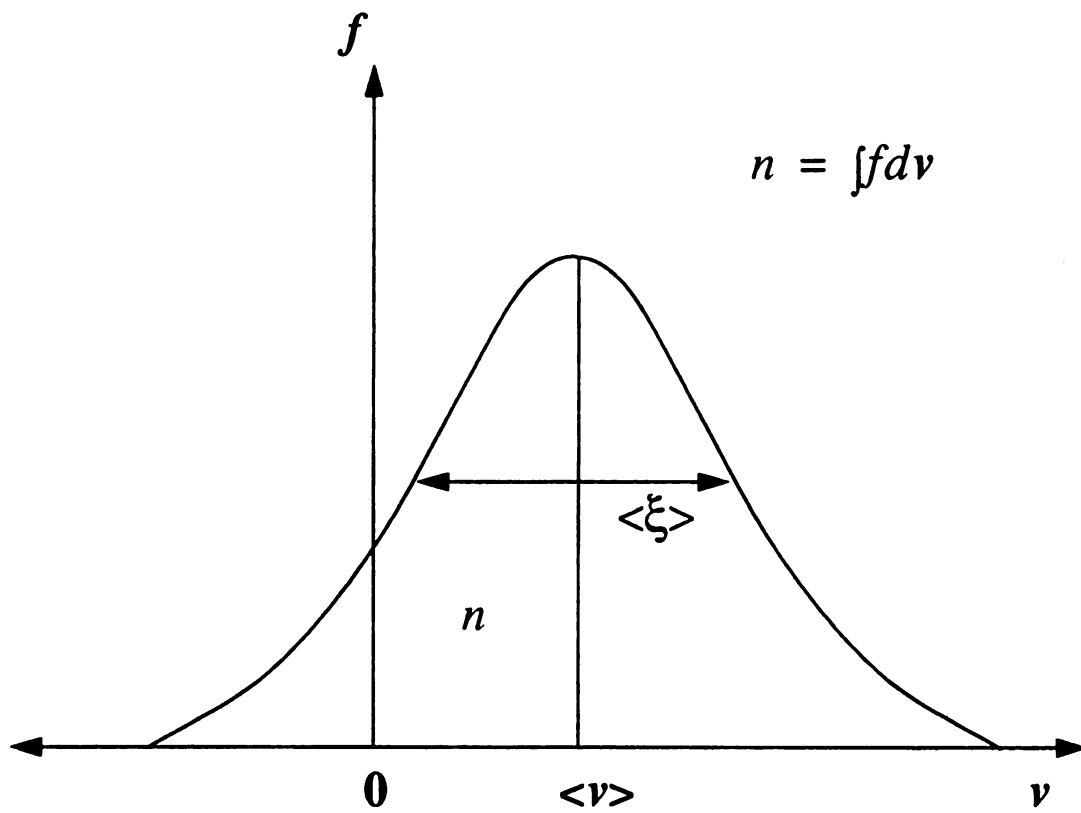


Figure 3-1: The distribution function f can be described by three moments: n , $\langle v \rangle$, and $\langle \xi \rangle$.

$$f(\xi) = \frac{2\sqrt{\xi}}{\sqrt{\pi}(k_B T)^{3/2}} e^{-\xi/2k_B T} \quad (3.6)$$

where $f(\xi)$ has been normalized so that

$$\int_0^\infty f(\xi) d\xi = 1. \quad (3.7)$$

Using the Maxwellian distribution function, the average energy of all particles in thermodynamic equilibrium can be determined by (3.4) as

$$\langle \xi \rangle = \frac{3}{2} k_B T \quad (3.8)$$

3.3.2 Boltzmann transport equation

When an external force is applied to the system of particles, the transport behaviors of the particles inside the discharge can be characterized by the Boltzmann transport equation (BTE). The Boltzmann transport equation, which describes the motion of the distribution function due to an external force in coordinate and velocity space, can be written as

$$\frac{\partial f}{\partial t} + \mathbf{v} \cdot \nabla_{\mathbf{r}} f + \frac{\mathbf{F}}{m} \cdot \nabla_{\mathbf{v}} f = \left(\frac{\partial f}{\partial t} \right)_{coll} \quad (3.9)$$

where $\nabla_{\mathbf{r}}$ is a gradient in coordinate (x, y, z) space, $\nabla_{\mathbf{v}}$ is a gradient in velocity space, \mathbf{F} represents external forces, and m is particle mass. The right hand side of equation (3.9) includes the randomly-timed scattering events that the particles experience, such as elastic

collisions, ionization collisions, and recombination collisions.

Since equation (3.9) does not have a direct, closed form solution, an alternative way to solve this equation is to make a series of simplifying assumptions to obtain the moments of the Boltzmann transport equation. The basic assumption is that the distributions of each plasma species can be described adequately by three macroscopic quantities, namely, particle density n , drift velocity $\langle \mathbf{v} \rangle$, and temperature T . The use of the moment equations, or fluid equations, considers the plasma to act as a fluid, rather than as individual particles. The condition for validity of this approximation is that the distance between particles be small with respect to the interparticle forces, i.e., $n\lambda_D^3 \gg 1$, where λ_D is the Debye length, and the mean free path \ll scale of change of macroscopic quantities. This condition is well satisfied in the plasma discharges investigated for this study. In the following section, the fluid models used in this study are constructed by obtaining the moment equations for the Boltzmann transport equation.

3.3.3 Moment equations

The moment equations are obtained from equation (3.9) by multiplying it by various functions of velocity, $\Phi(\mathbf{v})$, and integrating over velocity space. The result is changing from the BTE (one equation) which is a function of $(x, y, z, v_x, v_y, v_z, t)$ to a series of equations which are just functions of (x, y, z, t) . Various $\Phi(\mathbf{v})$ functions include 1, \mathbf{v} , and $\mathbf{v}\mathbf{v}$, etc. which give rise to the zero-order, first-order, and second-order, etc. moment equations.

Hence, multiplying (3.9) by $\Phi(\mathbf{v})$ and integrating over velocity space, the general moment equation may be written as

$$\frac{\partial}{\partial t}(n\langle\Phi\rangle) + \nabla \bullet (n\langle\mathbf{v}\Phi\rangle) - \frac{ne}{m}\mathbf{E} \cdot \left\langle \frac{\partial\Phi}{\partial\mathbf{v}} \right\rangle = \left[\frac{\partial}{\partial t}(n\langle\Phi\rangle) \right]_{coll} \quad (3.10)$$

where \mathbf{F} is replaced by $e\mathbf{E}$, where e is the particle charge and \mathbf{E} is the electric field.

Thus the BTE for the distribution function f is replaced by a set of equations containing averaged quantities. Each moment equation introduces the next higher-order velocity moment due to the second term in equation (3.10). The moment equations are then an infinite set of equations unless some additional assumptions are used to break the chain of equations and restrict the variables to a manageable number. These additional assumptions will be considered below.

The zero-order moment equation is obtained from equation (3.10) by putting $\Phi = 1$ to get

$$\frac{\partial n}{\partial t} + \nabla \bullet (n\langle\mathbf{v}\rangle) = \left[\frac{\partial n}{\partial t} \right]_{coll}. \quad (3.11)$$

The zero-order moment equation (3.11) is the particle continuity equation. According to (3.11) the change of particle density plus the divergence of particles equals the change in density due to collisions.

The velocity \mathbf{v} of the particles inside discharges can be expressed as the sum of the drift velocity and thermal velocity \mathbf{c} , i.e., $\mathbf{v} = \langle\mathbf{v}\rangle + \mathbf{c}$, and in most case, $c \gg \langle v \rangle$. By putting $\Phi(\mathbf{v}) = m\mathbf{v}$ into equation (3.10) and assuming the particle pressure is given by $P = nm\langle c^2 \rangle / 2 = nk_B T$ (thermodynamic equilibrium condition), the first-order moment equation can be derived to be

$$\frac{\partial}{\partial t} \langle v \rangle + \langle v \rangle \cdot \nabla \langle v \rangle + \frac{1}{mn} \nabla (nk_B T) - \frac{e}{m} E = \left[\frac{\partial}{\partial t} \langle v \rangle \right]_{coll} \quad (3.12)$$

where the collision term can be written as

$$\left[\frac{\partial}{\partial t} \langle v \rangle \right]_{coll} = \frac{1}{mn} \left[\frac{\partial}{\partial t} (mn \langle v \rangle) \right]_{coll} - \frac{\langle v \rangle}{n} \left[\frac{\partial}{\partial t} \langle v \rangle \right]_{coll} \quad (3.13)$$

which represents the rate of drift velocity (momentum) change due to elastic and inelastic collisions.

Similarly, with the same assumption for particle pressure, the second-order moment equations can be obtained by substitute $\Phi(v) = \frac{1}{2} m v v$ into equation (3.10),

$$\frac{\partial W}{\partial t} + \nabla \cdot (\langle v \rangle W) = en \langle v \rangle \cdot E - \nabla \cdot (\langle v \rangle nk_B T) - \nabla \cdot Q + \left[\frac{\partial W}{\partial t} \right]_{coll} \quad (3.14)$$

where W is the average energy density ($W = \frac{1}{2} nm \langle v \rangle^2 + \frac{3}{2} nk_B T$), and Q is the heat flux ($Q = -\lambda \nabla T$, λ is the heat conductivity). Equation (3.14) contains on the left-hand side the rate of change of the average energy density plus the outflow of average energy density W . On the right-hand side, the first term is the power supplied by the electric field, the second term is the work performed by the particle pressure, the third term is the divergence of the heat flow Q , and the last term is the rate of change of particle energy density due to collisions.

The zero, first, and second moment equations shown in (3.11), (3.12) and (3.14) are also called the continuity equation, momentum conservation equation, and energy conservation equation, respectively. These moment equations sometimes are simplified to construct the drift-diffusion model as shown in the next section.

3.3.4 Drift-Diffusion model

The Drift-Diffusion model consists of solving the Poisson equation and the continuity equation (3.11). This model makes a simplified approximation for the momentum equation (3.12) and neglects the energy conservation equation (3.14). The drift-diffusion model assumes that all the particles in the discharges are at thermal equilibrium and the particle temperature gradient is zero.

Assuming the particle considered here is an electron, $e = -q$, the first step to simplify the moment conservation equation is using a simple relaxation model to replace the collision term in (3.12), i.e.

$$\left[\frac{\partial}{\partial t} \langle v \rangle \right]_{coll} = -\langle v \rangle \nu_m \quad (3.15)$$

where ν_m is defined as the collision frequency for momentum transfer. This assumption is valid because the major momentum loss of electrons in partially ionized discharges results primarily from the elastic collision with neutrals. Moreover, assuming the collision term dominates over the inertial term, the momentum conservation equation becomes

$$\langle v \rangle = -\frac{qE}{m\nu_m} - \frac{k_B T}{m\nu_m} \frac{\nabla n}{n}. \quad (3.16)$$

If the mobility and diffusion parameters are defined as

$$\mu_n = \frac{q}{m\nu_m} \quad (3.17)$$

and

$$D_n = \frac{k_B T}{q} \mu_n, \quad (3.18)$$

then the expression for the electron velocity can be written as

$$\langle v_n \rangle = -\mu_n E - D_n \frac{\nabla n}{n} \quad (3.19)$$

and the electron flux becomes

$$J_n = n \langle v_n \rangle = -n \mu_n E - D_n \nabla n \quad . \quad (3.20)$$

This representation of electron transport is referred to as the ‘Drift-Diffusion’ model and can be extended similarly for ions in the discharges. The equations in the Drift-Diffusion model for electrons and ions are the electron continuity equation, ion continuity equation, and Poisson equation, which is used to provide a self-consistent space charge field. The equations are written as

$$\nabla^2 \Psi = \frac{q}{\epsilon} (n_e - n_i) \quad (3.21)$$

$$\frac{\partial n_e}{\partial t} + \nabla \cdot J_e = \left[\frac{\partial n_e}{\partial t} \right]_{coll} \quad (3.22)$$

$$\frac{\partial n_i}{\partial t} + \nabla \cdot J_i = \left[\frac{\partial n_i}{\partial t} \right]_{coll} \quad (3.23)$$

where Ψ is the plasma potential, n_e and n_i are the electron and ion density, and the electron and ion current density J_e and J_i can be expressed as

$$J_e = -n_e \mu_e E - D_e \nabla n_e \quad (3.24)$$

and

$$J_i = n_i \mu_i E - D_i \nabla n_i \quad (3.25)$$

3.3.5 Fluid model

The Drift-Diffusion model discussed above is valid only under the assumptions that the discharge is in thermodynamic equilibrium condition, i.e. $T_{electron} = T_{ion} = T_{neutrals}$, and has a spatially uniform temperature distribution. However, this is not true for microwave discharges. For the microwave discharges investigated in this study, electrons absorb microwave energy more efficiently and hence have a higher temperature than other plasma species, such as ions and neutrals. Due to most of the microwave energy being imparted into electron gas, and the electron temperature plays an important role in determining the transport parameters and reaction rates. Therefore, the energy conservation equation of electron has to be included in the fluid model in order to provide a self-consistent solution. The fluid model used in this model then includes the ion continuity equation (3.23), the ion current equation (3.25), the electron continuity equation (3.22), the electron current equation (3.24) and a variation of the electron energy conservation equation (3.14).

The energy conservation equation of electron used in the fluid model for this study is based on equation (3.14). By assuming that the energy distribution of electrons is $\frac{3}{2} k_B T_e \gg \frac{1}{2} m \langle v \rangle^2$, (3.14) can be simplified to be [51]

$$\frac{\partial}{\partial t} \left(\frac{3}{2} k_B T_e n_e \right) + \nabla \cdot \mathbf{q}_e = -q \mathbf{J}_e \cdot \mathbf{E} + \left[\frac{\partial W}{\partial t} \right]_{coll} \quad (3.26)$$

where \mathbf{q}_e is the electron heat flux, which includes both heat convection and conduction terms

$$\mathbf{q}_e = \frac{5}{2} k_B T_e \mathbf{J}_e - \left(\frac{5}{2} k_B D_e n_e \right) \nabla T_e. \quad (3.27)$$

Note that the thermal conduction coefficient λ in (3.14) is approximated to be $\frac{5}{2} D_e n_e$ [52].

For partially ionized discharges, where the neutral densities are much greater than the electron and ion densities, the right-hand side of the continuity equations of electrons and ions, (3.22) and (3.23), are primarily determined by the inelastic collision events of electrons, such as ionization (electron-neutral interaction) and recombination (electron-ion interaction). These can be written as

$$\left[\frac{\partial n_e}{\partial t} \right]_{coll} = \left[\frac{\partial n_i}{\partial t} \right]_{coll} = \sum_j n_e R_{ion}^j - \sum_j \alpha_r^j n_i^j n_e \quad (3.28)$$

where R_{ion} is the ionization rate (sec^{-1}), α_r is the electron-ion recombination coefficient ($\text{m}^3 \text{sec}^{-1}$), and index j stands for different ion and neutral species. Equation (3.28) also implies that the electron attachment mechanism is not significant in the discharge of interest. This is true for the argon gases portion of this study.

The electron energy loss due to collisions can also be more completely specified as the energy loss due to several electron-neutral and electron-ion interactions, including

electron-neutral elastic collisions, ionizations, excitations, dissociations, and electron-ion recombinations. Thus the collision term on the right-hand side of equation (3.26) can be written as

$$\begin{aligned} \left[\frac{\partial W}{\partial t} \right]_{coll} = & -n_e \left(\sum_j \epsilon_{ion}^j R_{ion}^j + \sum_j \epsilon_{ext}^j R_{ext}^j + \sum_j \epsilon_{dis}^j R_{dis}^j \right) \\ & - \sum_j \frac{2m_e}{m_n^j} \left(\frac{3}{2} k_B T_e - \frac{3}{2} k_B T_n^j \right) \nu_m^j n_e - \frac{3}{2} k_B T_e \sum_j \alpha_r^j n_i^j n_e \end{aligned} \quad (3.29)$$

where R_{ion} , R_{ext} and R_{dis} together with ϵ_{ion} , ϵ_{ext} and ϵ_{dis} represent the rate and threshold energy for ionization, excitation, and dissociation. ν_m is the electron-neutral momentum transfer frequency. Moreover, the collision rate R for neutral ionization, excitation and dissociation can be expressed as

$$R_{ion, ext, dis} = n_n k_{ion, ext, dis}$$

where n_n is the neutral density, and k is the rate coefficient with unit, m^3/sec , which is usually a function of electron temperature [50].

In summary, the fluid model for plasma discharges involving both electrons and ions solves self-consistently the Poisson equation, the continuity equation for electron, the continuity equation for ions, and the energy conservation equation for electrons. Since in this study we are interested in steady state phenomenon, these equations can be written as

$$\nabla^2 \Psi = \frac{q}{\epsilon} (n_e - n_i) \quad (3.30)$$

$$\nabla \cdot \mathbf{J}_e = \sum_j n_e n_n k_{ion}^j - \sum_j \alpha_r^j n_i^j n_e \quad (3.31)$$

$$\nabla \cdot J_i = \sum_j n_e n_n k_{ion}^j - \sum_j \alpha_r^j n_i^j n_e \quad (3.32)$$

$$\begin{aligned} \nabla \cdot q_e = & -q J_e \cdot E \\ & -n_e n_n \left(\sum_j \epsilon_{ion}^j k_{ion}^j + \sum_j \epsilon_{ext}^j k_{ext}^j + \sum_j \epsilon_{dis}^j k_{dis}^j \right) \\ & - \sum_j \frac{2m_e}{m_n^j} \left(\frac{3}{2} k_B T_e - \frac{3}{2} k_B T_n^j \right) v_m^j n_e - \frac{3}{2} k_B T_e \sum_j \alpha_r^j n_i^j n_e \end{aligned} \quad (3.33)$$

where

$$J_e = -n_e \mu_e E - D_e \nabla n_e \quad (3.34)$$

$$J_i = n_i \mu_i E - D_i \nabla n_i \quad (3.35)$$

and

$$q_e = \frac{5}{2} k_B T_e J_e - \left(\frac{5}{2} k_B D_e n_e \right) \nabla T_e. \quad (3.36)$$

3.4 Numerical solution implementation

In this section, the implementation of numerical solutions for the models discussed in the last section will be presented. To solve the fluid plasma model numerically involves discretization of the equations at a set of grid points. Setting up the discretized equations for the grid points constructs a nonlinear matrix problem which typically needs to be solved iteratively. If the iterations result in a convergent solution, the unknowns on the grid points are solved. Several numerical methods have been used in the literature to solve

the fluid equations including the finite difference and finite element methods. For this study, the finite difference method has been used to solve these equations. The details of the numerical solution are presented below.

3.4.1 Discretization

The numerical solution of the fluid equations requires the discretization of the equations (3.30) to (3.33) for an appropriate grid structure superimposed on the simulated discharge geometry. For cylindrical microwave plasma sources, the discretization of the equations should be done in cylindrical coordinate. Since the resonant electromagnetic modes of the microwave plasma sources used for diamond thin film deposition are normally TM_{01n} mode, the electric field spatial distributions are ϕ symmetric in nature and the E_ϕ component is zero. Therefore the discharge behavior can be assumed to be ϕ symmetric and the discretization of the equations reduced to a two dimensional problem. Thus, the simulation region remains in the r - z plane only.

In order to obtain a symmetric and stable solution from the simulation, a grid structure arrangement is developed according to the staggered-mesh arrangement [43][59] as shown in Figure 3-2. The area within the dotted square represents a simulation cell, (i, k) . The indices along the radial and axial axes are represented by i and k , respectively. The positions of plasma densities, potential and electron temperature are defined at the center of each cell which is represented by the dark circle. The r and z components of the current density and electric field are defined at the positions marked with an empty circle and gray circle, respectively. The quantity values at undefined positions can be interpolated from their value-defined neighbors. For example, the electron density at the boundary between

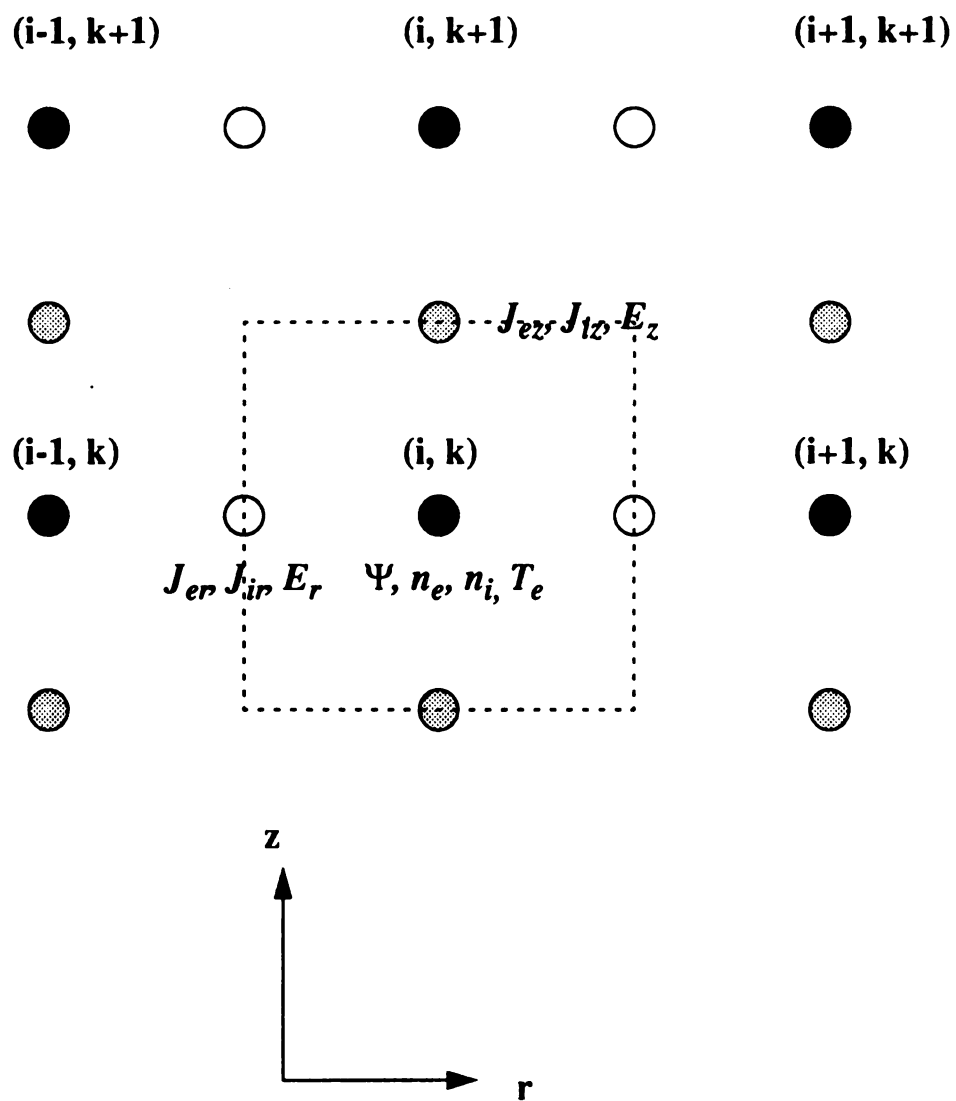


Figure 3-2: Staggered-mesh arrangement.

cell (i, k) and cell (i, k+1) can be determined by averaging the electron density of positions (i, k) and (i, k+1).

The discretization of the Poisson equation is done using a ‘five-point’ finite difference approximation derived from truncated Taylor series. The details of the derivation are shown in Appendix. It gives in cylindrical coordinates

$$\begin{aligned}
& \left(\frac{2}{r_{i+1/2}^2 - r_{i-1/2}^2} \right) \cdot \frac{r_{i+1/2}}{\Delta r_i} \cdot \Psi(i+1, k) \\
& + \left(\frac{2}{r_{i+1/2}^2 - r_{i-1/2}^2} \right) \cdot \frac{r_{i-1/2}}{\Delta r_{i-1}} \cdot \Psi(i-1, k) \\
& + \frac{2}{(\Delta z_k + \Delta z_{k-1})} \cdot \frac{\Psi(i, k+1)}{\Delta z_k} \\
& + \frac{2}{(\Delta z_k + \Delta z_{k-1})} \cdot \frac{\Psi(i, k-1)}{\Delta z_{k-1}} \\
& - \left(\frac{2}{r_{i+1/2}^2 - r_{i-1/2}^2} \right) \cdot \left(\frac{r_{i+1/2}}{\Delta r_i} + \frac{r_{i-1/2}}{\Delta r_{i-1}} \right) \\
& + \frac{2}{(\Delta z_k + \Delta z_{k-1})} \cdot \left(\frac{1}{\Delta z_k} + \frac{1}{\Delta z_{k-1}} \right) \cdot \Psi(i, k) \\
& = -\frac{q}{\epsilon} (n_i(i, k) - n_e(i, k))
\end{aligned} \tag{3.37}$$

For electron continuity equation, (3.31) can be written in discretized form as

$$\begin{aligned}
& \left(\frac{2}{r_{i+1/2}^2 - r_{i-1/2}^2} \right) \cdot r_{i+1/2} \cdot J_{er} \left(i + \frac{1}{2}, k \right) \\
& - \left(\frac{2}{r_{i+1/2}^2 - r_{i-1/2}^2} \right) \cdot r_{i-1/2} \cdot J_{er} \left(i - \frac{1}{2}, k \right) \\
& + \frac{2}{(\Delta z_k + \Delta z_{k-1})} \cdot \left(J_{ez} \left(i, k + \frac{1}{2} \right) - J_{ez} \left(i, k - \frac{1}{2} \right) \right) \\
& = n_e(i, k) [n_n(i, k) k_{ion}(i, k) - \alpha_r(i, k) n_i(i, k)]
\end{aligned} \tag{3.38}$$

The electron flux in (3.34) can also be discretized as

$$J_{er}\left(i + \frac{1}{2}, k\right) = \left(-\frac{D_e}{\Delta r_i} + \frac{\mu_e}{2}\left(\frac{\Psi(i+1, k) - \Psi(i, k)}{\Delta r_i}\right)\right) \cdot n_e(i+1, k) \\ + \left(\frac{D_e}{\Delta r_i} + \frac{\mu_e}{2}\left(\frac{\Psi(i+1, k) - \Psi(i, k)}{\Delta r_i}\right)\right) \cdot n_e(i, k) \quad (3.39)$$

and

$$J_{ez}\left(i, k + \frac{1}{2}\right) = \left(-\frac{D_e}{\Delta z_k} + \frac{\mu_e}{2}\left(\frac{\Psi(i, k+1) - \Psi(i, k)}{\Delta z_k}\right)\right) \cdot n_e(i+1, k) \\ + \left(\frac{D_e}{\Delta z_k} + \frac{\mu_e}{2}\left(\frac{\Psi(i, k+1) - \Psi(i, k)}{\Delta z_k}\right)\right) \cdot n_e(i, k) . \quad (3.40)$$

The ion continuity equation is similar to that of the electron continuity equation and is simply the substitute of index i for e and μ_e for $-\mu_i$ in (3.38), (3.39), and (3.40).

Finally, the electron energy conservation equation can be discretized using the same methods discussed above. Note that the heating term $qJ_e \cdot E$ in equation (3.33) primarily represents the microwave power absorbed by the plasma, which is determined by the microwave electric field and the microwave induced current density using the electromagnetic field model developed in Chapter 2. Therefore, for simplicity, this heating term can be viewed as an input parameter, P_{abs} , for the energy conservation equation, and it is not necessary that it be discretized. Equation (3.33) can be discretized as:

$$\begin{aligned}
& \left(\frac{2}{r_{i+1/2}^2 - r_{i-1/2}^2} \right) \cdot r_{i+1/2} \cdot q_{er} \left(i + \frac{1}{2}, k \right) \\
& - \left(\frac{2}{r_{i+1/2}^2 - r_{i-1/2}^2} \right) \cdot r_{i-1/2} \cdot q_{er} \left(i - \frac{1}{2}, k \right) \\
& + \frac{2}{(\Delta z_k + \Delta z_{k-1})} \cdot \left(q_{ez} \left(i, k + \frac{1}{2} \right) - q_{ez} \left(i, k - \frac{1}{2} \right) \right) \\
& = n_e(i, k) \sum_j H^j(i, k) + P_{abs}(i, k)
\end{aligned} \tag{3.41}$$

where $\sum_j H^j(i, k)$ represents all the collisional energy loss in (3.33). The heat flux terms are discretized as

$$\begin{aligned}
q_{er} \left(i + \frac{1}{2}, k \right) &= \frac{5}{2} k_B \left(\frac{T_e(i+1, k) + T_e(i, k)}{2} \right) J_{er} \left(i + \frac{1}{2}, k \right) \\
&\quad - \frac{5}{2} k_B D_e \left(\frac{n_e(i+1, k) + n_e(i, k)}{2} \right) \left(\frac{T_e(i+1, k) - T_e(i, k)}{\Delta r_i} \right)
\end{aligned} \tag{3.42}$$

and

$$\begin{aligned}
q_{ez} \left(i, k + \frac{1}{2} \right) &= \frac{5}{2} k_B \left(\frac{T_e(i, k+1) + T_e(i, k)}{2} \right) J_{ez} \left(i, k + \frac{1}{2} \right) \\
&\quad - \frac{5}{2} k_B D_e \left(\frac{n_e(i, k+1) + n_e(i, k)}{2} \right) \left(\frac{T_e(i, k+1) - T_e(i, k)}{\Delta z_k} \right).
\end{aligned} \tag{3.43}$$

Equation (3.37) to (3.43) are derived for the case that r is not equal to zero, i.e. not at the center of the cylinder. The discretized equations for r equal to zero and their derivations are also given in Appendix.

3.4.2 Numerical solution

The solution of the discretized fluid plasma equations on a grid of N nodes involves a total of $4N$ unknowns for the fluid model since at each point the unknowns are Ψ , n_e , n_i , and T_e . The system of $4N$ discretized equations including the Poisson equation, the continuity equation for electrons and ions, and the energy conservation equation for electrons are

$$F(\Psi, n_e, n_i, T_e) = \begin{bmatrix} F_{\Psi}(\Psi, n_e, n_i, T_e) \\ F_{n_e}(\Psi, n_e, n_i, T_e) \\ F_{n_i}(\Psi, n_e, n_i, T_e) \\ F_{T_e}(\Psi, n_e, n_i, T_e) \end{bmatrix} = 0 \quad (3.44)$$

where F_{Ψ} denotes the system of the N poisson equations, F_{n_e} and F_{n_i} denote the system of $2N$ continuity equations for electrons and ions, and F_{T_e} denotes the system of N energy conservation equations for electrons. Two principle methods of solving the system of non-linear equations (3.44) are the fully coupled method or Newton method and the decoupled method or iterative method [60] [61].

The Newton's method linearizes the system of partial differential equations and, by starting from an initial guess, the solution of the nonlinear equations is obtained by iterating the matrix equation

$$\begin{bmatrix} \frac{\partial F_\Psi}{\partial \Psi} & \frac{\partial F_\Psi}{\partial n_e} & \frac{\partial F_\Psi}{\partial n_i} & \frac{\partial F_\Psi}{\partial T_e} \\ \frac{\partial F_{n_e}}{\partial \Psi} & \frac{\partial F_{n_e}}{\partial n_e} & \frac{\partial F_{n_e}}{\partial n_i} & \frac{\partial F_{n_e}}{\partial T_e} \\ \frac{\partial F_{n_i}}{\partial \Psi} & \frac{\partial F_{n_i}}{\partial n_e} & \frac{\partial F_{n_i}}{\partial n_i} & \frac{\partial F_{n_i}}{\partial T_e} \\ \frac{\partial F_{T_e}}{\partial \Psi} & \frac{\partial F_{T_e}}{\partial n_e} & \frac{\partial F_{T_e}}{\partial n_i} & \frac{\partial F_{T_e}}{\partial T_e} \end{bmatrix}^k \begin{bmatrix} \Delta \Psi \\ \Delta n_e \\ \Delta n_i \\ \Delta T_e \end{bmatrix} = - \begin{bmatrix} F_\Psi(\Psi^k, n_e^k, n_i^k, T_e^k) \\ F_{n_e}(\Psi^k, n_e^k, n_i^k, T_e^k) \\ F_{n_i}(\Psi^k, n_e^k, n_i^k, T_e^k) \\ F_{T_e}(\Psi^k, n_e^k, n_i^k, T_e^k) \end{bmatrix} \quad (3.45)$$

where k denotes the iteration count. The correction vector for the k-th iteration is given by

$$\begin{aligned} \Delta \Psi^k &= \Psi^{k+1} - \Psi^k \\ \Delta n_e^k &= n_e^{k+1} - n_e^k \\ \Delta n_i^k &= n_i^{k+1} - n_i^k \\ \Delta T_e^k &= T_e^{k+1} - T_e^k \end{aligned} \quad (3.46)$$

The iterative method decouples the equations such that each system of equations can be treated independently for each iteration cycle. Each system of equations are solved sequentially and variables are updated after each solution. When all the updates are less than a set of criterion for an iteration, the convergence is reached. This iterative method can be written as

$$\left(\frac{\partial F_\Psi(\Psi^k, n_e^k, n_i^k, T_e^k)}{\partial \Psi} \right) \cdot \Delta \Psi^k = -F_\Psi(\Psi^k, n_e^k, n_i^k, T_e^k) \quad (3.47)$$

$$\left(\frac{\partial F_{n_e}(\Psi^{k+1}, n_e^k, n_i^k, T_e^k)}{\partial n_e} \right) \cdot \Delta n_e^k = -F_{n_e}(\Psi^{k+1}, n_e^k, n_i^k, T_e^k) \quad (3.48)$$

$$\left(\frac{\partial F_{n_i}(\Psi^{k+1}, n_e^{k+1}, n_i^k, T_e^k)}{\partial n_i} \right) \cdot \Delta n_i^k = -F_{n_i}(\Psi^{k+1}, n_e^{k+1}, n_i^k, T_e^k) \quad (3.49)$$

$$\left(\frac{\partial F_{T_e}(\Psi^{k+1}, n_e^{k+1}, n_i^{k+1}, T_e^k)}{\partial T_e} \right) \cdot \Delta T_e^k = -F_{T_e}(\Psi^{k+1}, n_e^{k+1}, n_i^{k+1}, T_e^k) \quad (3.50)$$

where (3.47) to (3.50) are solved sequentially. At each stage only one system of N equations is being linearized and solved by the Newton method, so the matrix being solved has N rows by N columns regardless of the number of coupled equations being solved. Whereas, in the full Newton method, all of the coupling between variables are taken into account and the matrix size will be $4N \times 4N$.

Because of the tight-coupling, the full Newton's method requires a smaller number of iterations for convergence, however, since the matrix size is larger, it takes more time to solve each iteration. Moreover, the Newton method needs larger computer memory to store the elements in the matrix. The iterative method usually takes considerably more iterations to reach the convergence while the time for each iterations is often less than the full Newton method because of the smaller matrix size. However, due to loosely coupled feature, the iterative method is less stable than the full Newton method, especially for high density plasma simulation.

In this study, both Newton's method and iterative method are used to solve the discretized equations. The Newton's method is used to solve Poisson's equation, electron

continuity equation, and ion continuity equations. The matrix size is $3N \times 3N$ and the plasma potential, electron density and ion density are solved in a tightly-coupled manner. These solutions are iteratively coupled with the discretized electron energy balance equation to solve the electron temperature and this temperature is then put back to the continuity equation and Poisson equation to modify the solution of densities and potential. The final solution is achieved by iteratively solving the continuity/Poisson equations and electron energy equation.

Since the electron energy balance equation and charge continuity equations are not tightly coupled, a damping technique has to be used in order to prevent unstable numerical problems such as oscillation or divergence from occurring. One damping method applied here is to use only a portion of the updated data as the input to the next coupled equation. This method can be written as

$$Q^{n+1} = Q^n + (Q^{n+1} - Q^n) \times \text{damping factor} \quad (3.51)$$

where Q represents a quantity to be solved (such as n_e or T_e) and n is the time index. (3.51) indicates that the new quantity which is used as the input for next coupled equation in the iterative solution is the sum of the previous quantity and a portion of the difference between the previous quantity and updated quantity. The damping factor is usually less than one to secure solution stability. If the damping factor is equal to one, that means no damping is applied for the solution. The value of the damping factor depends on the current situation of the solution. If damping factor is too high, the solution might diverge very fast, however, if too low, it will take more loops to get a converged solution. A automatic damping factor algorithm was implemented by checking the value of F_ψ , F_{ne} ,

F_{ni} and F_{Te} defined in (3.24). When an exact solution is reached, the value of F_{Ψ} , F_{ne} , F_{ni} and F_{Te} should equal or be close to zero. If the current values of F_{Ψ} , F_{ne} , F_{ni} and F_{Te} are higher than the previous ones, that means the solutions are starting to diverge and a smaller value should be used to secure stability. Otherwise, the damping factor can become larger to speedup the convergence. This damping technique is also used for the Newton method while calculating the potential and densities to ensure the stability of the solution.

Both the Newton method and iterative method produce a linear matrix equation of the form $Ax = B$. This matrix equation can be solved by direct or iterative techniques [55]. In this study, this linear matrix equation is solved by the LU-decomposition method. Since matrix A is a banded, sparse matrix, after a careful arrangement of matrix A , the size of A can be reduced from $3N \times 3N$ to $(6n_r+5) \times 3N$, where n_r is the number of grids in the r direction. The reduced matrix A can save substantial memory space and increase the speed of calculation [60].

3.5 Summary

The fluid plasma model of this study was developed in this chapter. The model consists of the Poisson equation, electron and ion continuity equations, and electron energy equation. The numerical methods used to solve these equations were also discussed. This fluid model can be used to investigate the characteristics of discharges and it can be coupled with the FDTD model to self-consistently simulate the electromagnetic excitation of discharges inside a microwave cavity plasma reactor. These simulation results will be present in Chapter 6.

Chapter 4

Transient State Simulation of Electromagnetic Fields Inside Empty and Loaded Microwave Resonant Cavities

4.1 Introduction

In Chapter 2, we discussed the fundamentals of the FDTD method used for solving Maxwell's equations in order to get the electromagnetic field solutions inside cylindrical cavities. Before simulating the complete microwave cavity plasma reactors operating in steady state with complex plasma loads, a simple-structure cylindrical resonant cavity will be simulated. Transient simulations of empty and loaded cylindrical resonant cavities will be done in order to establish the accuracy of the FDTD model for microwave cavity plasma reactors.

Several simulation results based on the FDTD model are provided in this chapter to study the electromagnetic mode variation and energy transfer inside cylindrical microwave resonant cavities. The electromagnetic resonant mode solutions of cylindrical, lossless, empty cavities, operating in either TE or TM modes, are determined in the time domain and are compared with theoretical results to verify the accuracy of the FDTD model. Two types of lossy loads in the resonant cavity are considered here. The first type is a non-dispersive load where the current density needed to solve Maxwell's equations is

determined from the conductivity using $\mathbf{J} = \sigma \mathbf{E}$. The second type is a dispersive load where the current density is determined by simultaneously solving the momentum transport equation in the time domain. For the non-dispersive load type, FDTD solutions were directly compared and found to agree with known analytical solutions. For the dispersive load type, FDTD solutions were compared to experimental measured argon discharge data. The simulations model the interactions between cavity characteristics, such as natural frequency and quality factor, and the properties of the plasma in microwave resonating cavities. Finally, the FDTD simulation results of a compact ECR ion source loaded with a helium discharge will be presented.

4.2 Simulation of electromagnetic fields inside empty cavities

In order to demonstrate the application and validity of the above FDTD formulation in the microwave plasma cavity, empty resonant cavity solutions are first described. Consider a cylindrical cavity geometry with perfectly conducting walls as shown in Figure 4-1. The boundary condition for the electric fields in such a cavity is that only the normal component of electric fields exists on the perfectly conducting wall and the tangential electric fields at the wall are zero, i.e., $E_z = 0$ and $E_\phi = 0$ when $r = a$, and E_r and $E_\phi = 0$ when $z = 0$ and L .

The way chosen to numerically incorporate an electromagnetic field excitation source inside the cavity for these empty cavity simulation is based on the specific cavity mode of resonance. The resonant mode depends on the diameter and height of the cylindrical cavity. The natural frequency (or so called eigenfrequencies) of a lossless, empty cavity are given by:

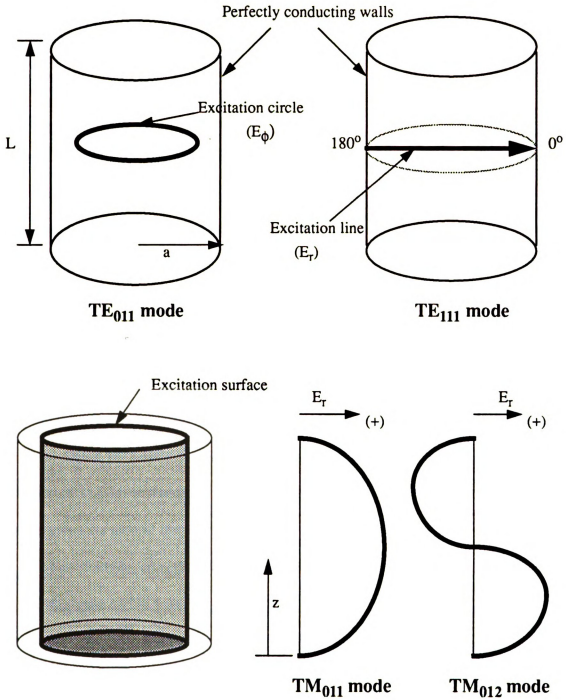


Figure 4-1: TE₀₁₁, TE₁₁₁, TM₀₁₁, and TM₀₁₂ mode excitation techniques in a cylindrical cavity.

$$\begin{aligned}
 f_{npq}^{TM} &= \frac{1}{2\pi\sqrt{\mu\epsilon}} \sqrt{\left(\frac{\lambda_{np}}{a}\right)^2 + \left(\frac{q\pi}{L}\right)^2} \\
 f_{npq}^{TE} &= \frac{1}{2\pi\sqrt{\mu\epsilon}} \sqrt{\left(\frac{\lambda'_{np}}{a}\right)^2 + \left(\frac{q\pi}{L}\right)^2}
 \end{aligned} \tag{4.1}$$

where TE and TM are the transverse electric mode and transverse magnetic mode respectively, npq are integers for TE and TM mode specification, λ_{np} is the p^{th} root of the Bessel function $J_n(x)$, and λ'_{np} is the p^{th} root of the first derivative of the Bessel function $J_n(x)$ ($J'_n(x)$).

One way to implement a source is selecting several lattice points as source points and assigning magnitudes of an electric field component at these points based on theoretical cavity field solutions [24]. These source points are driven a few cycles at a frequency close to the resonant frequency, then turned off. The electromagnetic fields then resonant inside the cavity at a frequency which depends on the cavity size as given by equation (4.1). This technique of exciting a mode inside the cavity and then turning off the source gives the natural frequency response.

For example, consider the excitation of the TE_{011} mode. Assume a cavity is 15.25 cm in diameter and 6.5 cm height, the resonant frequency for the TE_{011} mode can be calculated using equation (4.1) as 3.33 GHz. The source points are chosen along a circle in the middle of the cavity height as shown in Figure 4-1, where the E_ϕ component has its maximum amplitude based on the theoretical resonant cavity field distribution. A uniform amplitude of E_ϕ is assigned along this circle and forced to oscillate at this frequency for a few cycles. The electromagnetic fields propagate from these points and resonant inside the cavity. The electromagnetic field energy U stored in the cavity is defined as

$$U(t) = 0.5 \int_V (\epsilon(r) (E(r, t))^2 + \mu(r) (H(r, t))^2) dV \quad (4.2)$$

where the integration is performed over the volume of the cavity, V . The electromagnetic field energy starts to increase as shown in Figure 4-2 until the source is turned off (0.5 nanosecond), at which time the stored energy remains constant because no energy loss occurs on the perfectly conducting walls. From the plots of the electric field variation versus time, the oscillation frequency after the source is turned off at 0.5 nsec can be obtained as the natural resonant frequency (3.33 GHz) as shown in Figure 4-2. The electric field has E_ϕ components only, and its spatial variation in the r - z plane matches the theoretical empty cavity results as shown in Figure 4-3. The theoretical empty cavity mode solution can be obtained by solving the time-harmonic Maxwell's equation in cylindrical coordinates as mentioned in Chapter 2. For TE_{011} mode, the electric field solution is given by

$$E = E_\phi = B \frac{\lambda'_{01}}{a} J'_0 \left(\lambda'_{01} \frac{r}{a} \right) \sin \left(\frac{\pi}{L} z \right) \quad (4.3)$$

where λ'_{01} is the first zero of the first derivative of the Bessel function J_0 , and B is the amplitude.

The number of grids used is 31 by 36 by 31 in the r , ϕ , and z directions, respectively. The grid spacing in each direction is uniform. The grid structure is shown in Figure 4-4. The unit time step is chosen as 0.5 psec to satisfy the finite difference stability condition as discussed in Section 2.3.

Other examples of mode excitation are the TM_{011} , TM_{012} and TE_{111} modes. For

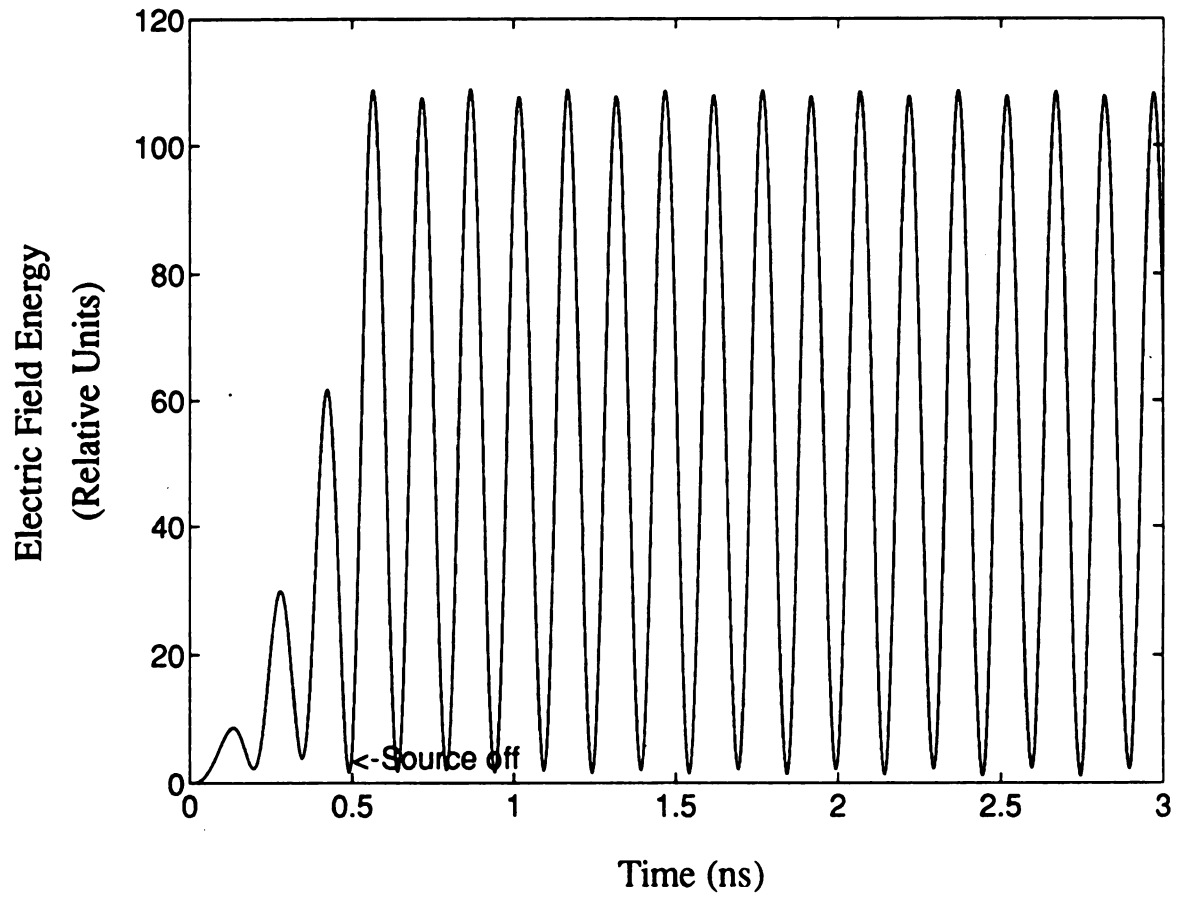


Figure 4-2: Electric field energy, $\frac{1}{V} \int_V \epsilon_0 E^2 dV$, versus time for the TE₀₁₁ mode. The empty cylindrical cavity was 15.25 cm in diameter and 6.5 cm high.

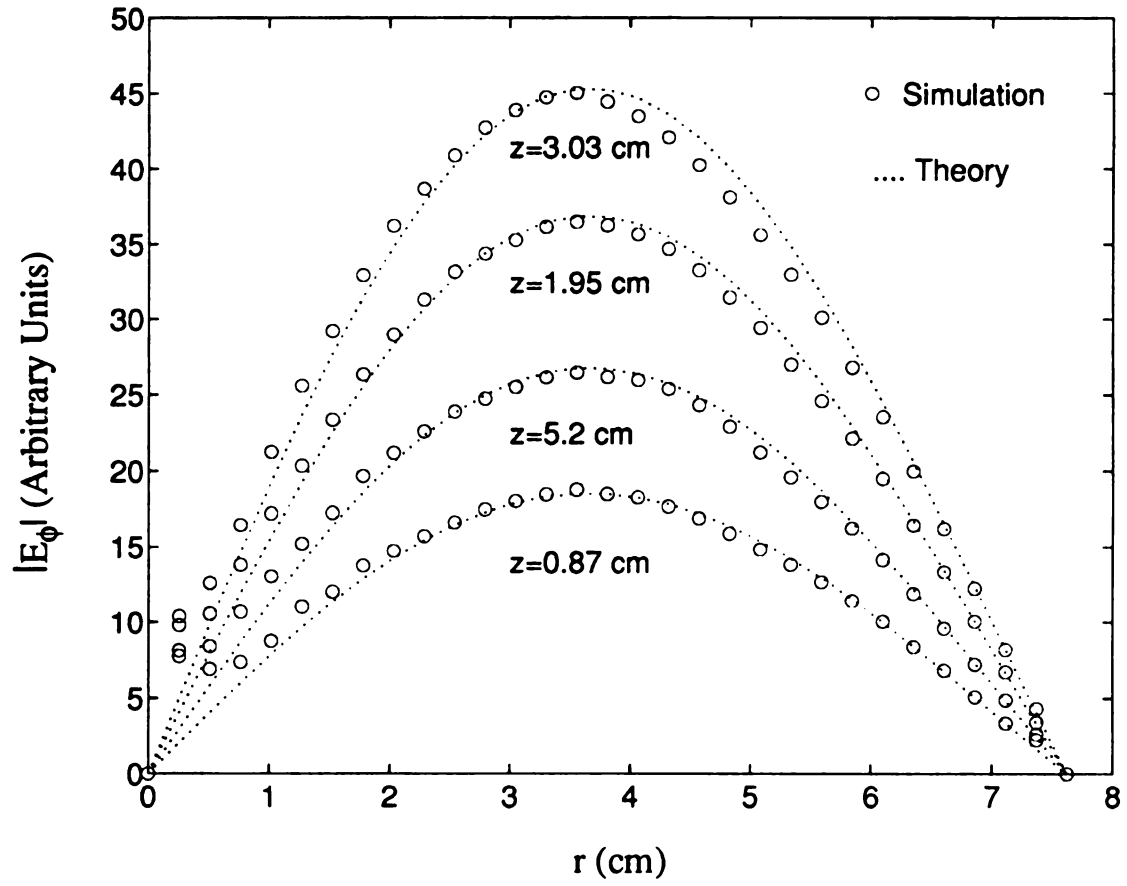
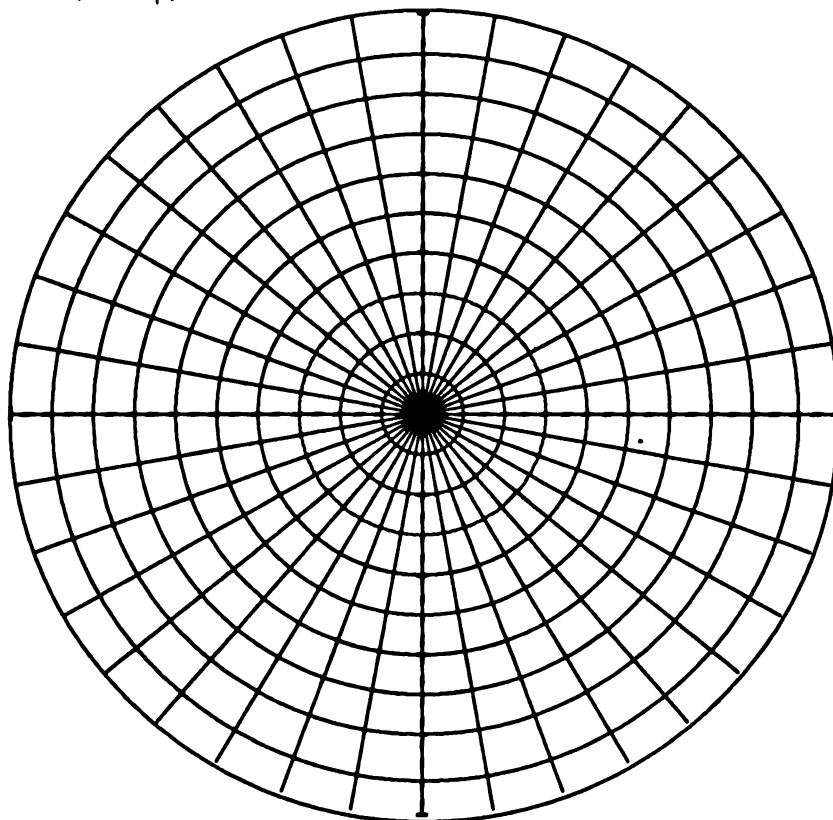


Figure 4-3: Radial dependence of $|E_\phi|$ at four different z locations for the TE_{011} mode.

(r - ϕ) Plane:



(r - z) Plane:

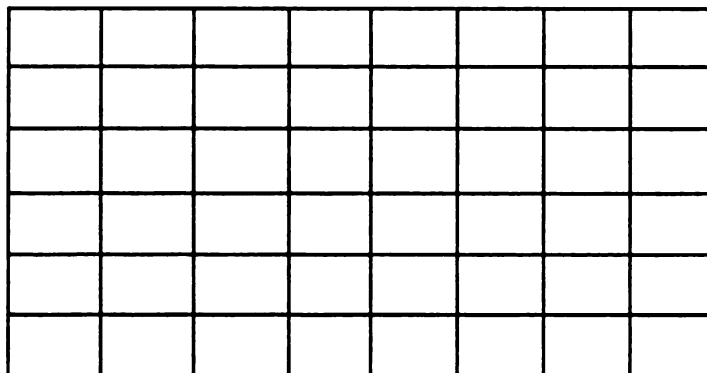


Figure 4-4: Grid structure for FDTD simulation in cylindrical coordinate.

TM_{01m} modes, instead of using a circle as a source, a cylindrical surface can be used as an excitation source as shown in Figure 4-1. This surface has a height equal to the cavity height, and a radius where E_r has a maximum for these modes. E_r is varied sinusoidally along the excitation surface based on theoretical resonant solutions. Using the same procedures mentioned above, the simulation results of the resonant electric field variations with time and space for the TM_{011} mode are shown in Figure 4-5 to Figure 4-7. In particular, the total stored energy as shown in Figure 4-6 is constant versus time after the excitation source is turned off at 1.25 nsec. Figure 4-8 shows the electrical field variation found using the FDTD technique and ideal empty cavity solutions versus r and z for the TM_{012} mode. Figure 4-9 shows the simulated E_r variation versus ϕ for the TE_{111} mode. The TM_{011} , TM_{012} , and TE_{111} modes solved by the FDTD method are all well matched with the theoretical solutions.

Due to the perfectly conducting wall assumptions, there is no energy loss for the empty cavity model, and the total energy inside the cavity remains constant once the source is turned off as shown earlier in Figure 4-6. Steady state solutions which are obtained by the source being always in an “on” condition can not be obtained for these ideal empty cavity simulations because no loss exists. The simulation technique which gives the steady-state response (the source is always on) for loaded cavities will be shown in the next chapter.

4.3 Natural frequency response for loaded lossy cavity

One application of this FDTD model is to investigate the power absorption inside a cavity when a lossy non-dispersive load is present, i.e., the dielectric property of the load

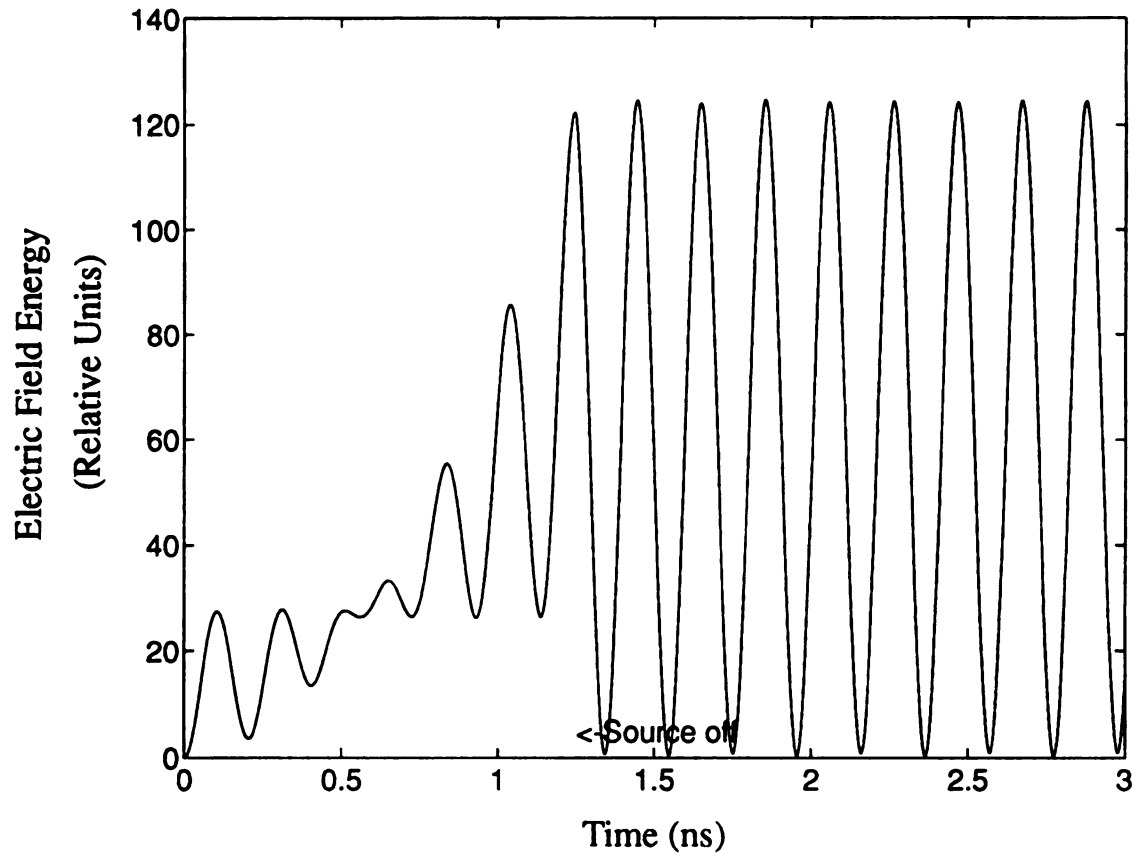


Figure 4-5: Electric field energy, $\frac{1}{V} \int_V \epsilon_0 E^2 dV$, versus time for the TM_{011} mode. The cylindrical empty cavity was 17.8 cm in diameter and 7.2 cm high. The resonant frequency was 2.45 GHz.

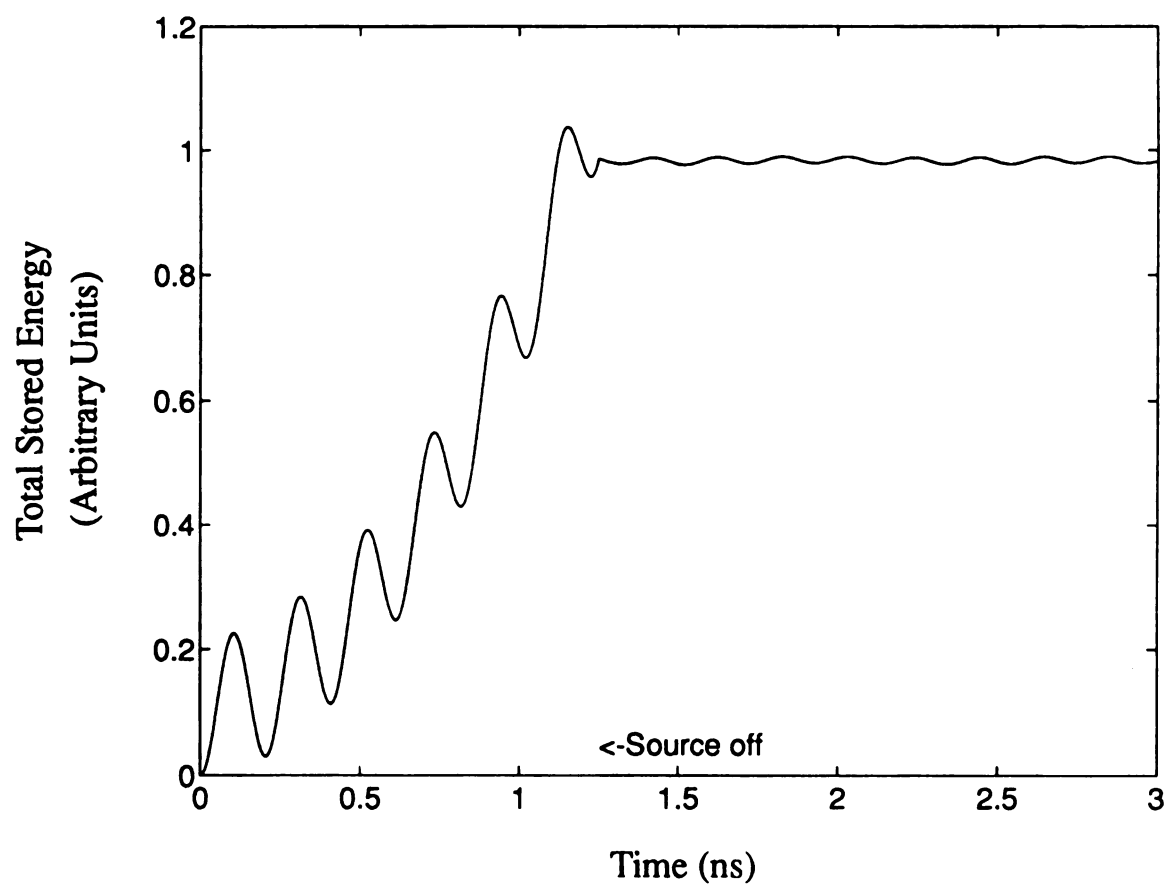


Figure 4-6: Total stored energy, U , versus time for the TM_{011} mode.

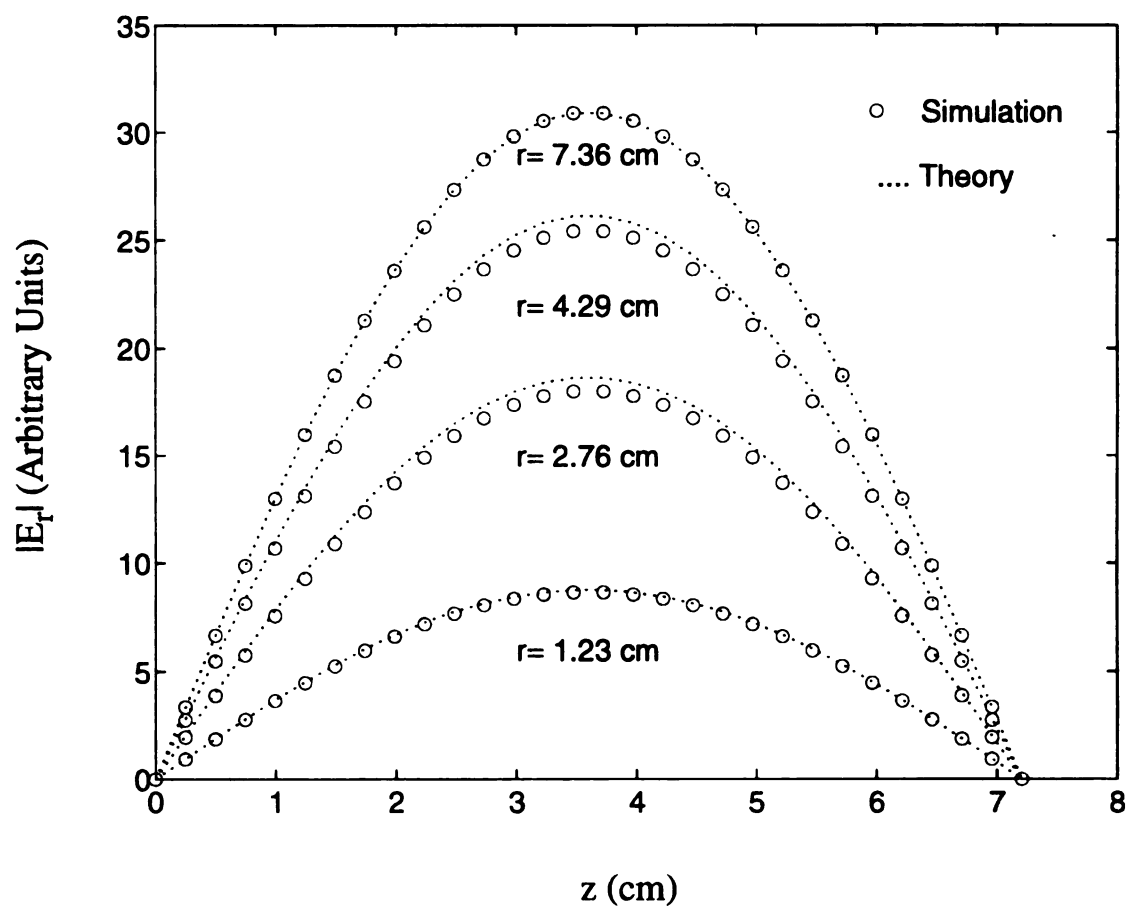


Figure 4-7: $|E_r|$ (arbitrary units) versus z at four different r locations for the TM_{011} mode.

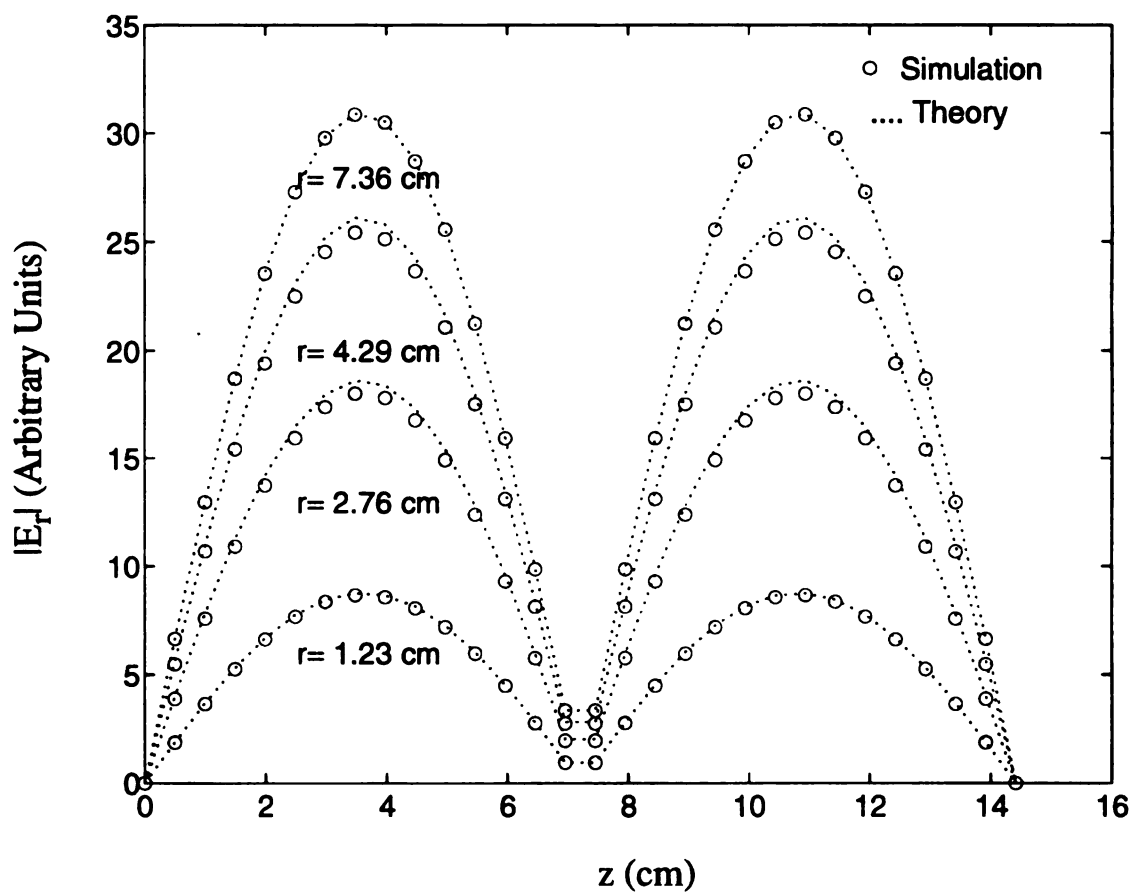


Figure 4–8: $|E_r|$ (arbitrary units) versus z at four different r locations for the TM_{012} mode. The cylindrical empty cavity was 17.8 cm in diameter and 14.41 cm high. The resonant frequency was 2.45 GHz.

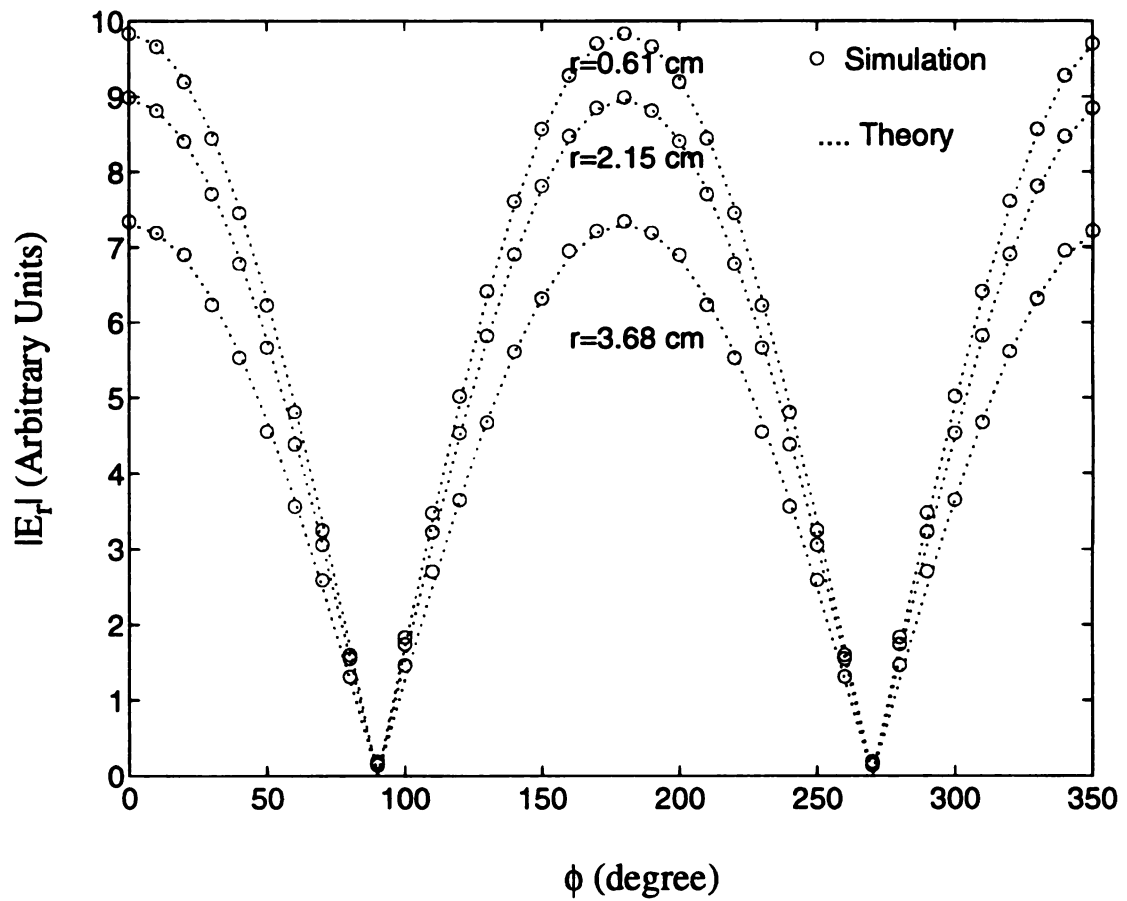


Figure 4–9: $|E_r|$ (arbitrary units) versus ϕ at three different r locations for the TE_{111} mode. The cylindrical empty cavity was 8.9 cm in diameter and 6.9 cm high. The resonant frequency was 2.45 GHz.

is independent of the resonant frequency. The natural frequency describes the transient response of the cavity to a pulse or to having a CW source shut off. For a cavity with a lossy load, the natural frequency is no longer a real number, but a complex number which can be written as

$$\hat{\omega} = \omega' + j\omega'' \quad (4.4)$$

where the real part ω' of the natural frequency $\hat{\omega}$ describes the frequency of field oscillation while the imaginary part ω'' of the natural frequency $\hat{\omega}$ is the exponential decay coefficient due to power absorption.

The FDTD model described in Chapter 2 can be used to analyze the natural frequencies of a lossy loaded cavity, by assigning a set of parameters including ϵ , μ and σ , at each lattice point inside the cavity. For a natural frequency response simulation, after the source is turned off, the electromagnetic fields inside the cavity will decay at a natural oscillating frequency, and the stored field energy will decrease due to energy dissipated into the lossy material. The relations can be expressed as follows:

$$\begin{aligned} E(t) &= E_0 e^{-\omega''t} e^{j\omega't} \\ U(t) &= U_0 e^{-2\omega''t} \end{aligned} \quad (4.5)$$

where E_0 is the initial electric field amplitude and U_0 is the initial stored energy at the time the source is turned off. By studying the electric field oscillation frequency after a source is turned off and the rate of the stored energy decay, the real part and imaginary part of the natural frequency $\hat{\omega}$ can be obtained.

As a specific example, consider a 15.24 cm diameter cavity loaded with a lossy, homogeneous, non-dispersive load. The cavity is the same size as the TE_{011} mode empty cavity demonstrated in the previous section. The lossy load is 2.54 cm in diameter and it is loaded coaxially with the same height as the cavity, as shown in Figure 4-10. To study the effect of the load conductivity on the electromagnetic fields inside the load region, the permittivity ϵ in equations (2.15) to (2.20) is set equal to $3.0\epsilon_0$, and σ is varied from zero to several hundred. Near the boundary of lossy dielectrics, where the most power is absorbed, fine grids are used to improve the accuracy of results. This fine grid structure is shown in Figure 4-11. The plots of electric field strength and total stored energy decay are shown in Figure 4-12 and Figure 4-13. It is clear from these plots that the decay rate and oscillation frequency varies with different conductivities. For example, at $\sigma = 0.1$ mho/m the result was $\omega' = 20.68 \times 10^9$ rad/sec and $\omega'' = 0.09 \times 10^9$ rad/sec, at $\sigma = 1.0$ mho/m the result was $\omega' = 21.13 \times 10^9$ rad/sec and $\omega'' = 0.45 \times 10^9$ rad/sec, and at $\sigma = 10$ mho/m the result was $\omega' = 21.59 \times 10^9$ rad/sec and $\omega'' = 0.16 \times 10^9$ rad/sec. The radial variation of E_ϕ for different conductivity loads is shown in Figure 4-14. For the case of the larger conductivity the electric field decays rapidly into the 2.5 cm diameter load.

A s-plane frequency chart can be used to further demonstrate the effect of conductivity variations on the electromagnetic fields. As shown in Figure 4-15, the horizontal axis represents the imaginary part of the conjugate of the complex natural frequency, i.e. $-\omega''$, and the vertical axis is the real part of the conjugate of the complex natural frequency, i.e. ω' . For $\sigma = 0$, the cavity is lossless and hence $\omega'' = 0$. When σ increases from zero, ω'' starts to increase, which is due to power dissipated into the lossy material. After σ is larger than 1.0, ω'' starts to decrease, because the cavity load

TE_{011} mode
 $B=15.24$ cm
 $A=2.54$ cm
 $L=6.5$ cm

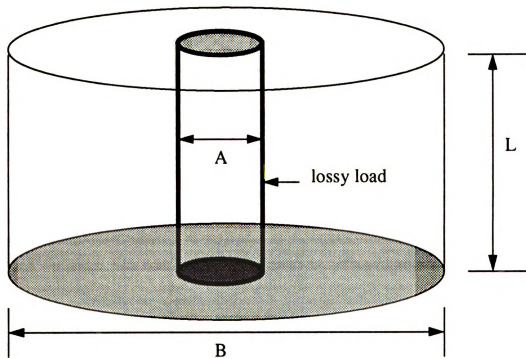
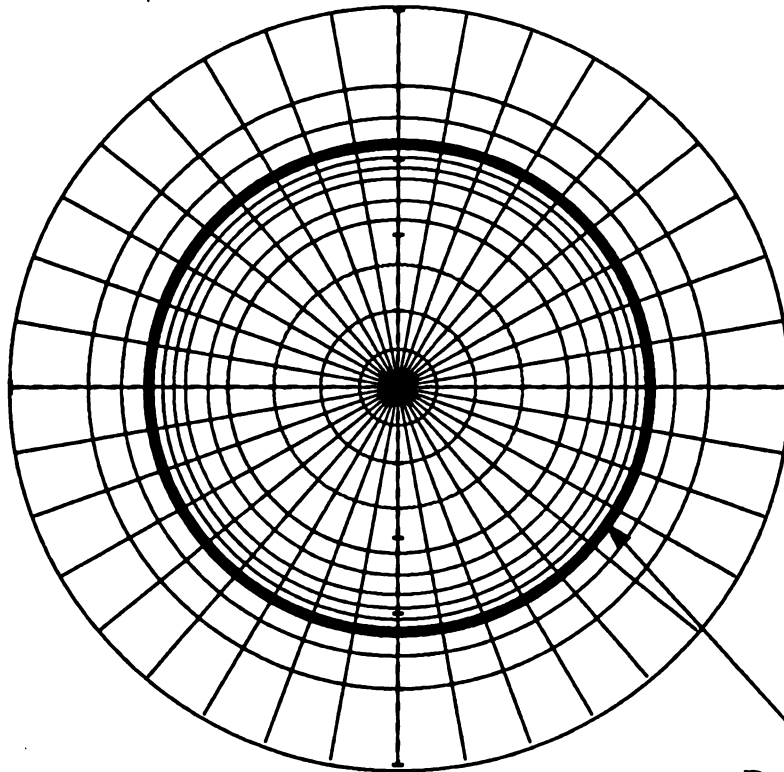


Figure 4-10: Configuration of a coaxially loaded cylindrical cavity.

(r - ϕ) Plane:



(r - z) Plane:

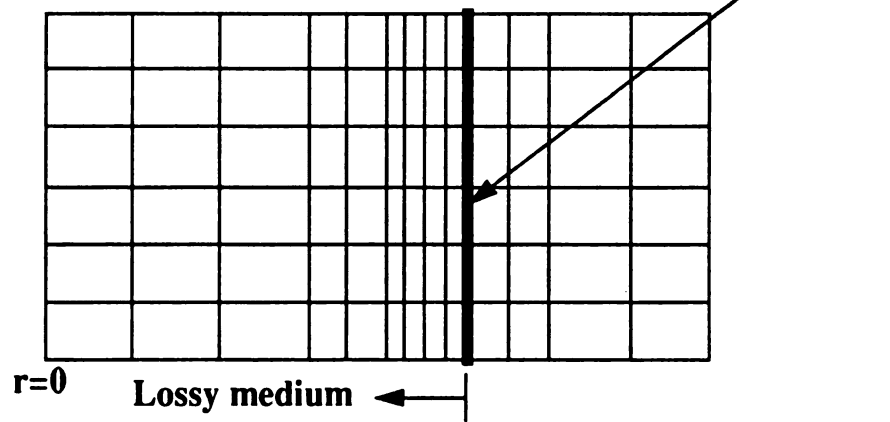


Figure 4-11: Fine grid structure for TE_{011} mode lossy cavity simulation.

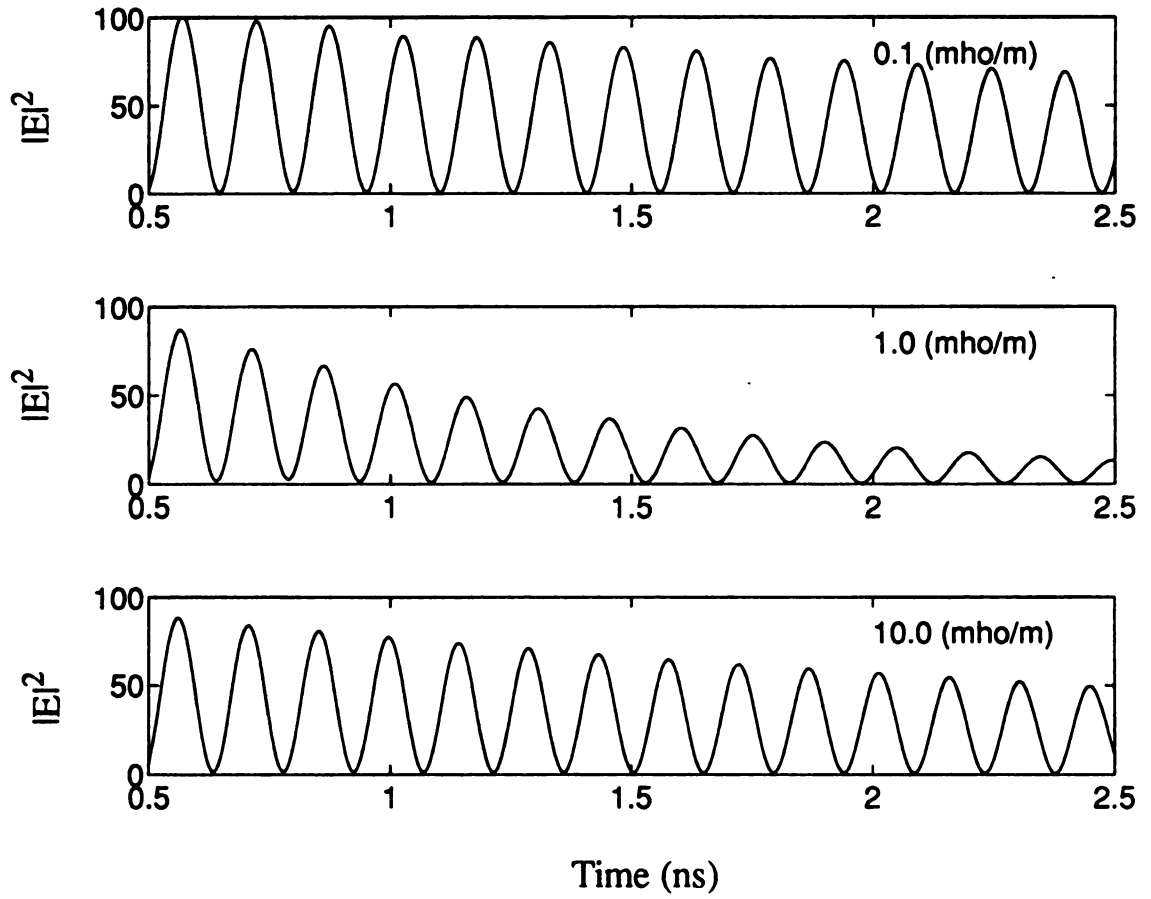


Figure 4-12: Space averaged $|E|^2$ (arbitrary units), versus time, for the TE_{011} mode. Results are shown for three different load conductivities after the source is turned off.

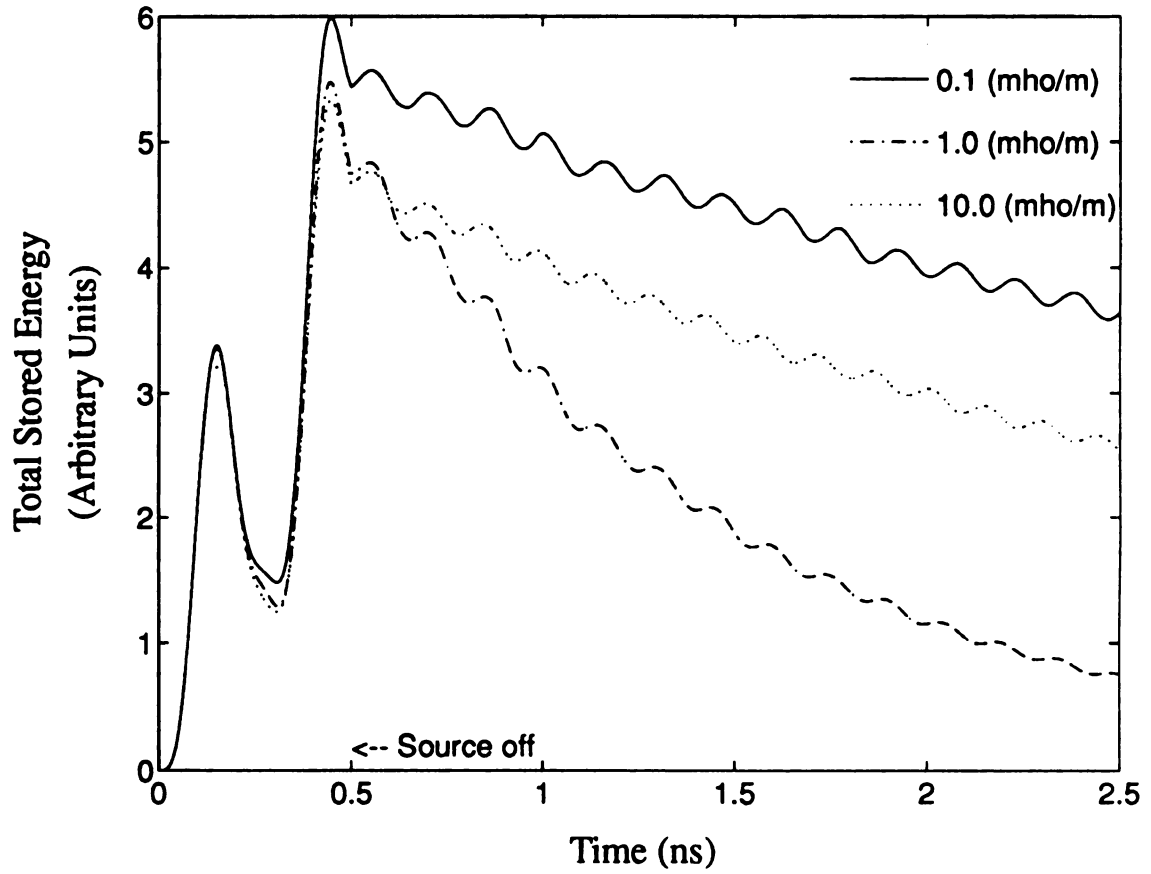


Figure 4-13: Total stored energy, U , versus time for the TE_{011} mode for three different load conductivities.

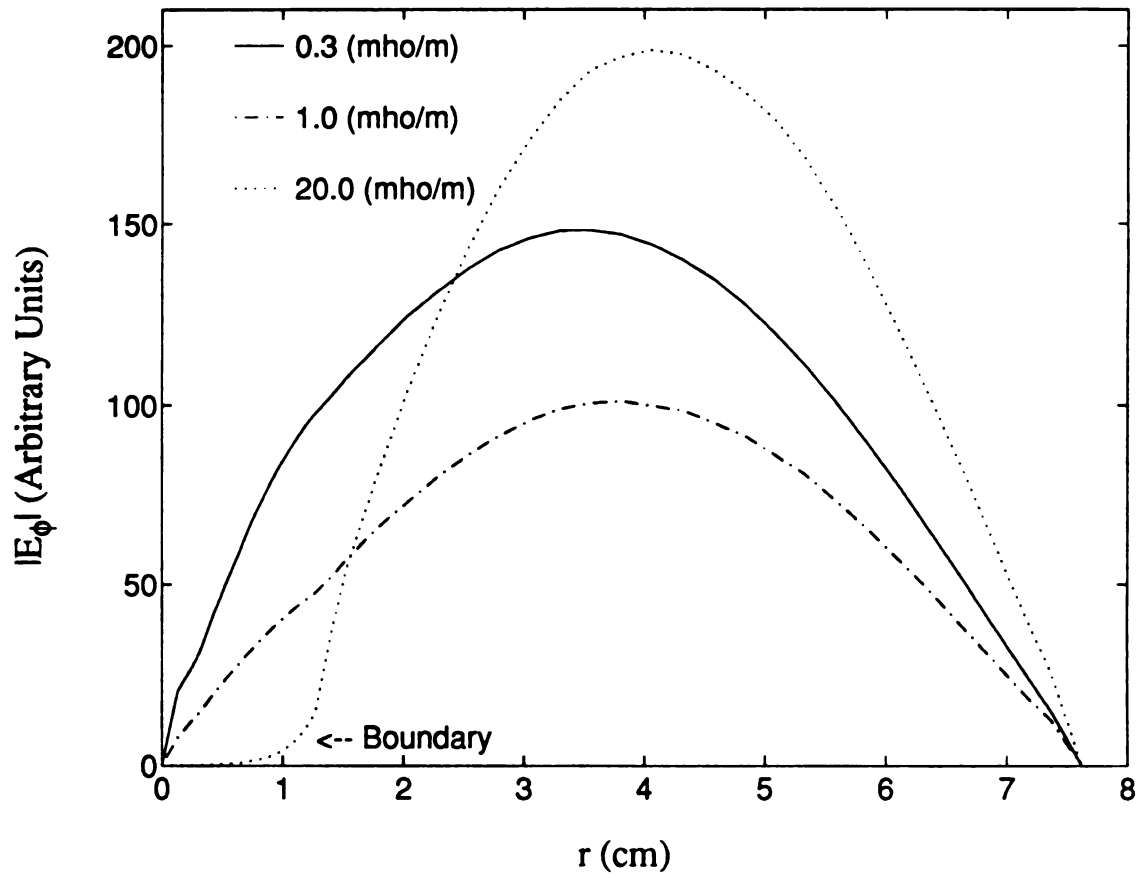


Figure 4-14 Radial dependence of $|E_\phi|$ (arbitrary units) for the TE_{011} mode for three different conductivity loads in a 15.25 cm i.d. cylindrical cavity.

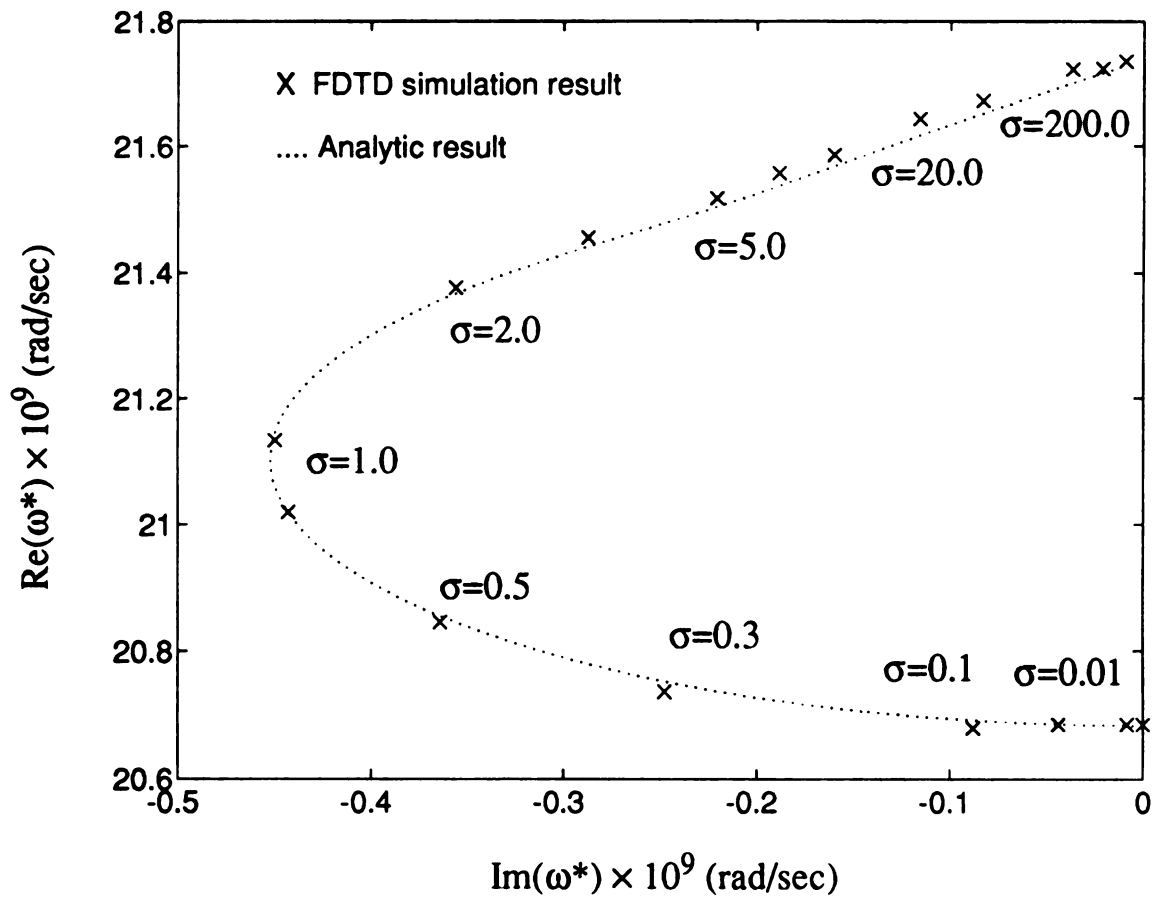


Figure 4-15: S-plane plot for the complex frequency as a function of load conductivity for the TE_{011} mode.

becomes a conducting-like material and the electromagnetic fields only penetrate the load a small amount (i.e. a skin depth). Thus, the resonant frequency changes (increases) as the TE_{011} empty cavity mode ($\sigma = 0$) varies to a coaxial type mode when σ is large.

For the case of a cavity loaded by a lossy, non-dispersive coaxial load, analytical solutions of ω' and ω'' exist. The FDTD technique solutions are compared to an analytical solution in Figure 4-15. In particular the FDTD result is compared with Marning's data [8], which is solved by an analytical method in the frequency domain. In the analytical method, the electric and magnetic fields are solved in cylindrical coordinates in terms of a set of Bessel function type solutions. The boundary conditions are applied to form a characteristic equation which is used to determine ω' and ω'' of the various modes. This method provides analytical solutions for non-dispersive lossy loads. The analytical solution and FDTD solution show agreement. However, if a more complex plasma with dispersive, inhomogeneous properties is used, the problem becomes very difficult to solve using analytical solutions. Moreover, if the geometry of the load is more complicated, it is also hard to solve for an analytical solution. Hence, the analytical solutions are only used in this work to verify the FDTD solution on simple geometry, non-dispersive loads.

4.4 Simulation results of an argon plasma loaded cavity

A FDTD calculation has been done to compare with the experiment results of Rogers [6]. In Rogers' study, a 17.78 cm i.d., microwave cavity excited at 2.45 GHz was coaxially loaded by an argon plasma in a 12 mm i.d. quartz tube with the plasma extending from the top to the bottom of the cavity as shown in Figure 4-16. The radial

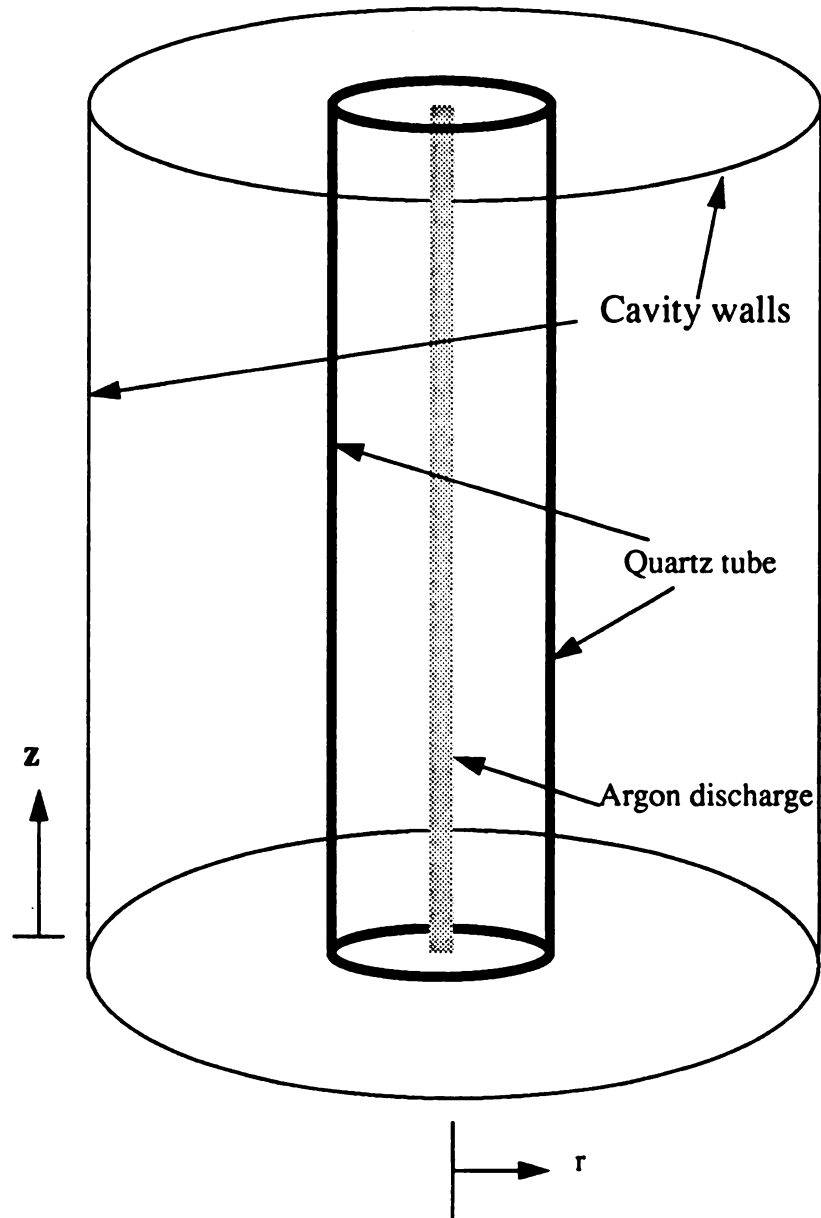


Figure 4-16: The geometry of a 17.8 cm i.d. cylindrical cavity with a 12 mm i.d. quartz tube loaded with an argon plasma.

component of electric field strength was measured by micro-coax electrical probes inserted through the cavity wall versus z and ϕ . The measured field distribution was compared with theoretical results to verify the mode sustained in the cavity with the discharge present was approximately a TM_{012} mode. The discharges inside the quartz tube had diameters of 2-4 mm depending on the pressure which was varied from 40 to 200 Torr. Rogers measured the cavity resonant length, average discharge diameter, total power absorption, cavity quality factor and calibrated electrical field strength at a reference point versus variations in pressure. This measured data was then used to extract the electron density and effective collision frequency versus pressure using (2.44) as shown in Figure 4-17.

Treating these values of electron density, effective collision frequency, and discharge diameter as input data, the cavity Q and the power density of the discharge can be simulated using the FDTD model. The definition of the quality factor, Q , is the time average energy stored in the cavity divided by time average energy dissipated in the cavity per cycle. Therefore, by calculating the time average energy stored and the time average power dissipated in the cavity for the first cycle after the source is turned off, a quality factor can be determined. In the simulation of the discharge loaded cavity, the electron density and the effective collision frequency are assumed uniform across the discharge volume. Additionally, the discharge volume is evaluated as a cylindrical rod with the same height as the cavity. The quartz tube was assumed lossless with a relative permittivity of $\epsilon_r = 3.78$ and a tube wall thickness equal to 1.0 mm. The electromagnetic source excitation used is the same as the TM_{012} mode empty cavity shown earlier in Figure 4-1. Current densities are calculated in time domain by equations (2.53) and (2.54) and coupled with a

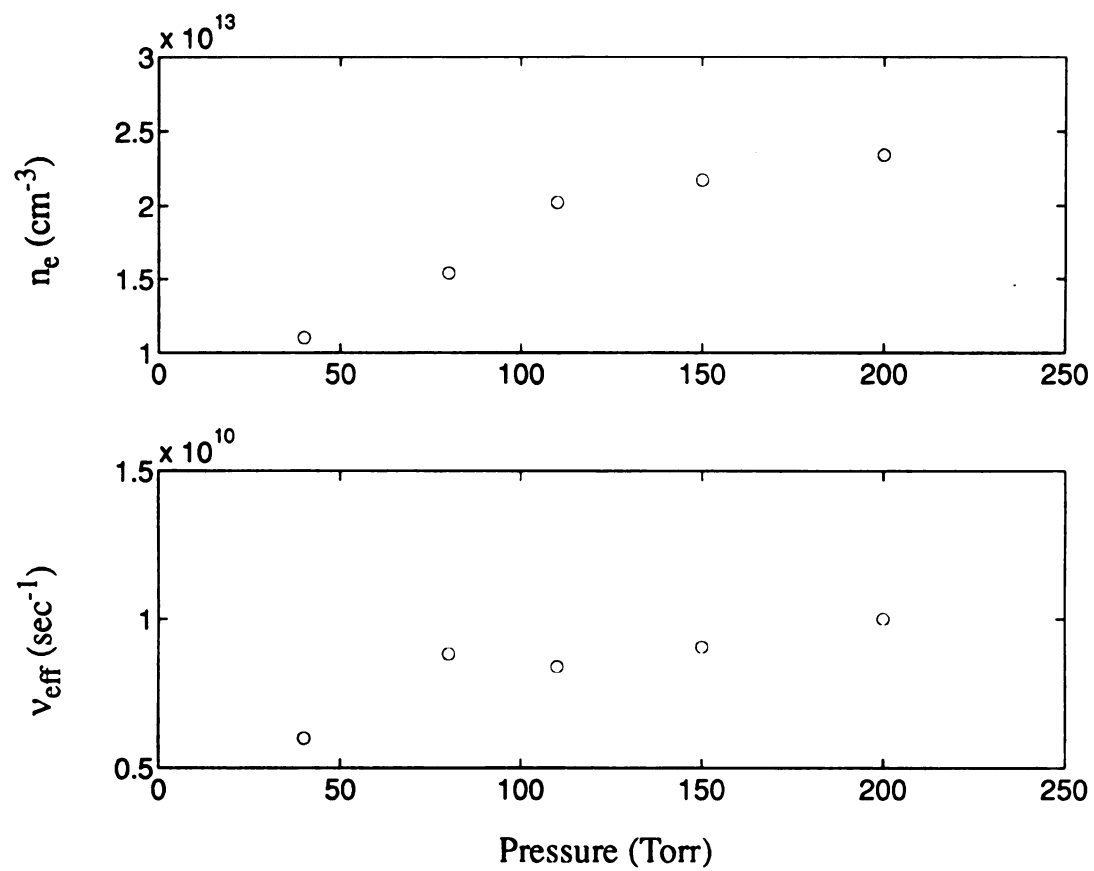


Figure 4-17: Electron density, n_e , and effective collision frequency, ν_{eff} , versus pressure for the argon plasma shown in Figure 4-16 (from Rogers' data [6]).

FDTD solution of Maxwell's equations to solve the electromagnetic fields inside and outside the discharge volume. Then, the power absorbed by the discharge is determined by equation (2.35), and the absorbed power density is evaluated by dividing the power absorbed in the discharge by the discharge volume. The simulation data of loaded cavity Q and absorbed power density is compared to experimental data in Figure 4-18 and Figure 4-19. The FDTD calculations show good agreement with the experimental data, which demonstrates the applicability of the FDTD technique to model plasma loaded microwave cavities.

4.5 Implementation and results for a compact ECR ion source

The FDTD model also has been used to investigate the electric field distribution inside a compact ion source [56]. The simplified ion source geometry for the FDTD simulation is shown in Figure 4-20. Basically, this ion source is 5.4 cm in diameter and 12.4 cm in height, with a 3.0 cm id., 3.5 cm high quartz disk which is used to confine the plasma discharges. The electromagnetic field boundaries for the structure in Figure 4-20 are the sliding short, center conductor, and the outer shell. Again, all the boundaries are assumed perfect conducting, therefore only the normal component of the electric field exists on these boundaries. The amplitude of an electric field component assigned on the source points is based on the TEM mode wave solution for a cylindrical coaxial waveguide. After an initial period of a few microwave oscillations (2.45 GHz), the source term is turned off and the natural response for an empty ion source is observed as in Figure 4-21. The field excitation plane chosen for electromagnetic field generation is shown in Figure 4-20. The resonant frequency is calculated from Figure 4-21 to be approximately

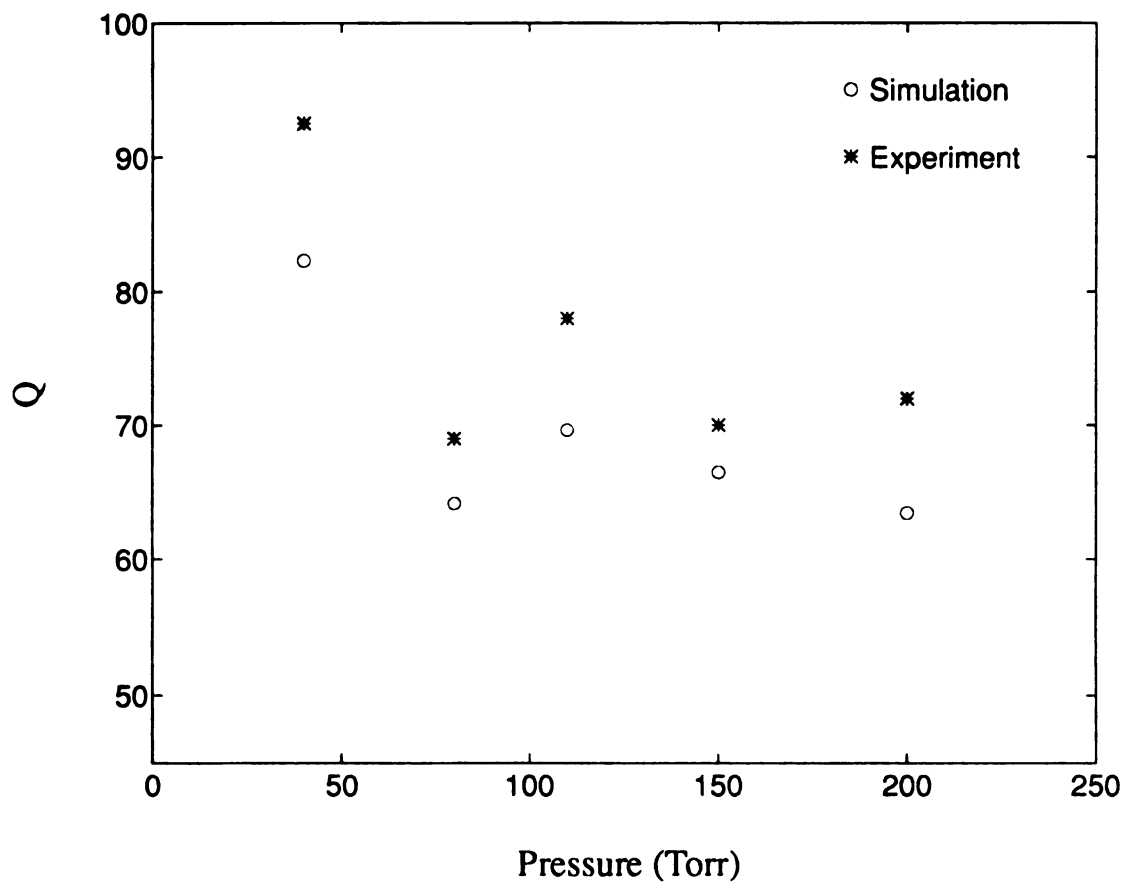


Figure 4-18: Loaded cavity quality factor, Q , versus pressure.

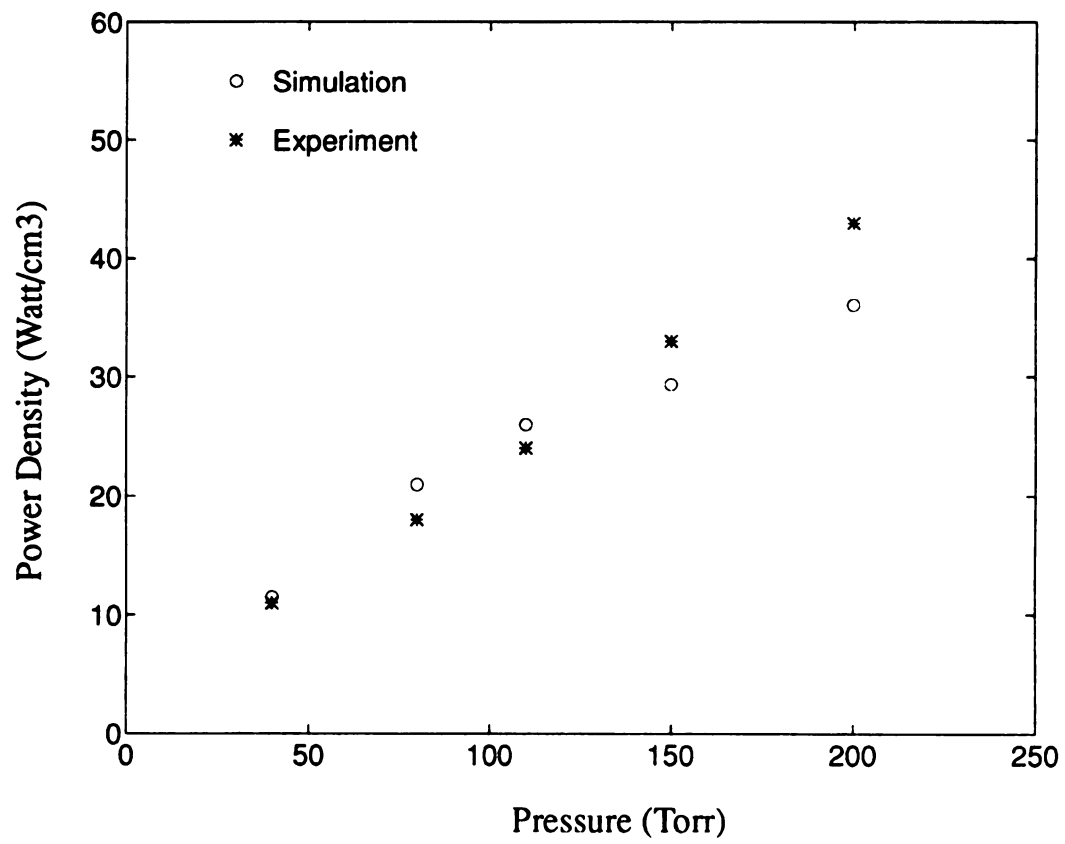


Figure 4-19: Absorbed power density versus pressure.

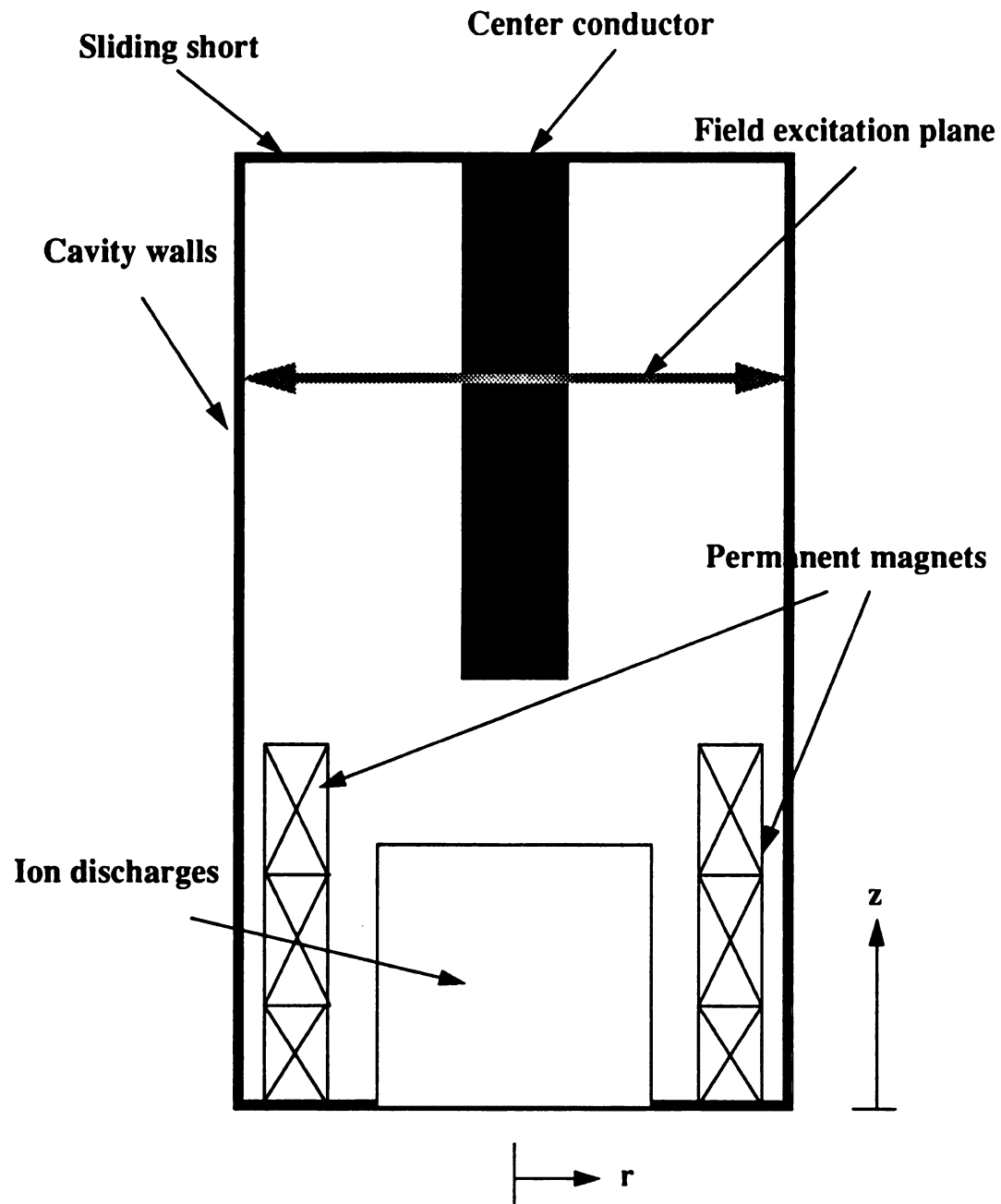


Figure 4-20: Simulation structure for an compact ECR ion source.

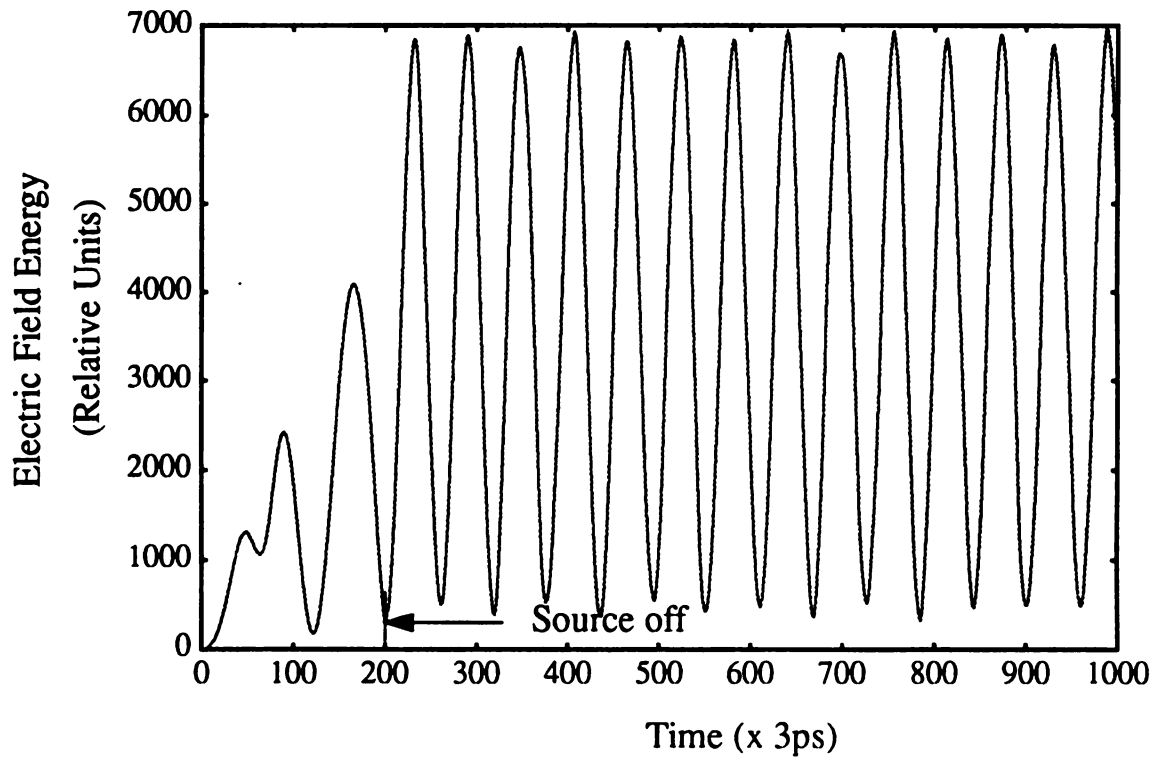


Figure 4-21: Electric field energy, $\frac{1}{V} \int_V \epsilon_0 E^2 dV$, versus time for the structure shown in

Figure 4-20 with no plasma load present. The excitation of the source was turned off at time = 0.6 nsec.

2.6 GHz. The electric field magnitude inside the resonating source is shown in Figure 4-22 and Figure 4-23.

The electromagnetic fields inside the resonant source when a helium plasma load is present have also been simulated. The conductivity of the magnetized plasma is determined based on equations (2.49) and (2.50), where the static magnetic fields produced by the permanent magnets were simulated by T.A. Grotjohn [41]. The plasma density and electron temperature of the helium discharge are measured by plasma diagnostic techniques in order to determine the effective collision frequency and subsequently the conductivity of helium discharges [56]. The calculated conductivity for the helium discharge has a peak value equal of 178 mho-m around the ECR region where the microwave electric field is perpendicular to the permanent magnetic field. The simulation results of the electric field distribution are shown in Figure 4-24 and Figure 4-25. The electric fields maintain the general structure shown for the empty source, although the influence of the plasma load can be seen. Also, the cavity was simulated as having a high quality factor, Q value, (several hundred to 1000) for the lower density helium discharges. For a more accurate simulation, a particle plasma model would need to be used to simulate the characteristics of this low pressure discharge and ECR heating mechanism.

4.6 Summary

In this chapter, simulation results for transient state solutions of lossless and lossy microwave cavities, i.e., the sources are turned off after several microwave excitation cycles, were presented. These solutions provide information for studying the

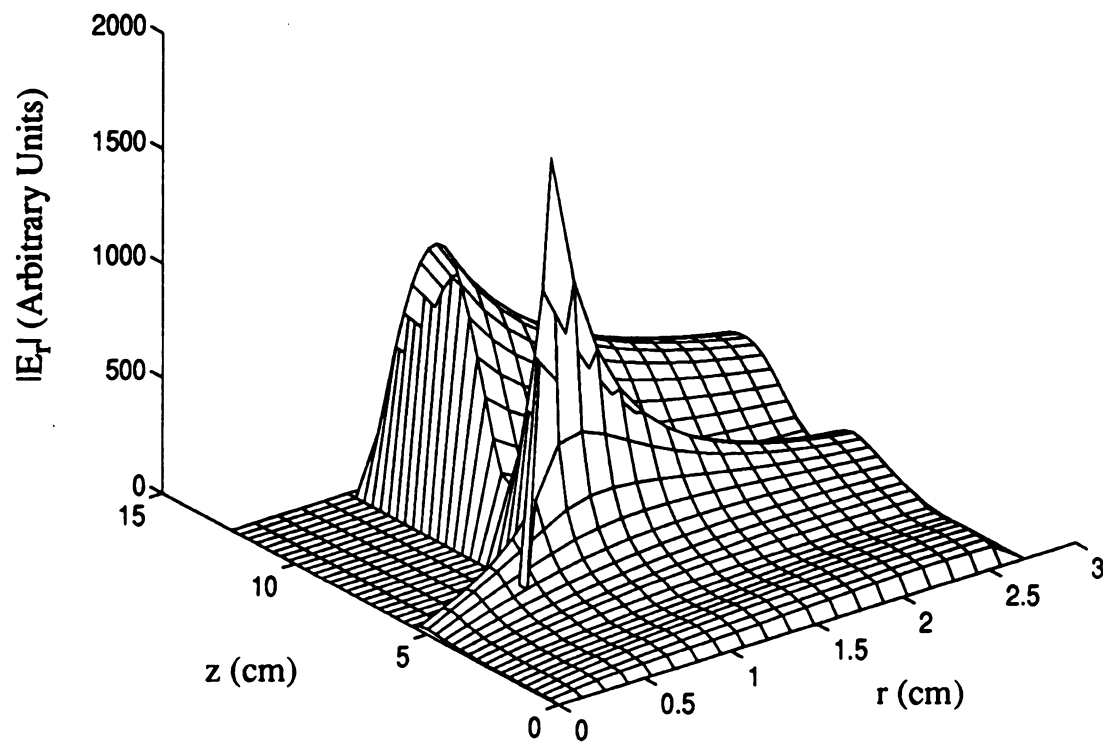


Figure 4-22: $|E_r|$ (arbitrary units) versus r and z .

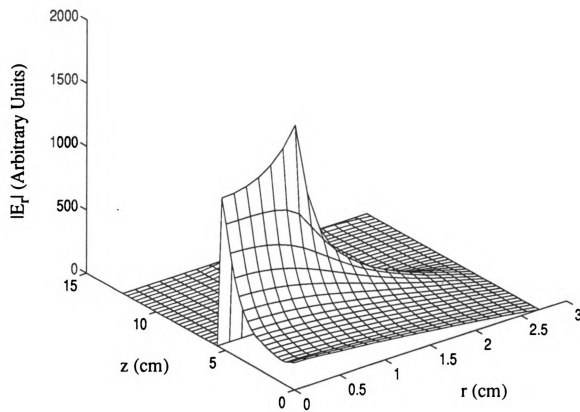


Figure 4-23: $|E_z|$ (arbitrary units) versus r and z .

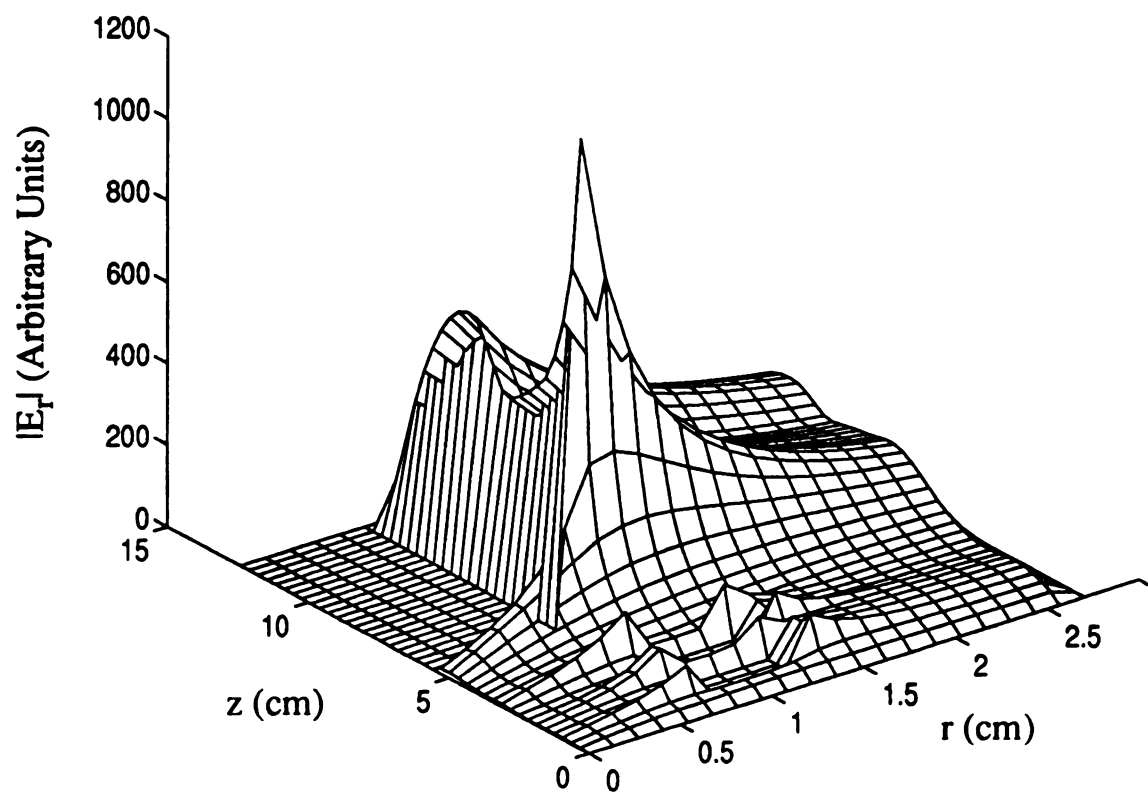


Figure 4-24: $|E_r|$ (arbitrary units) versus r and z for the compact ion source operated with a helium plasma discharge.

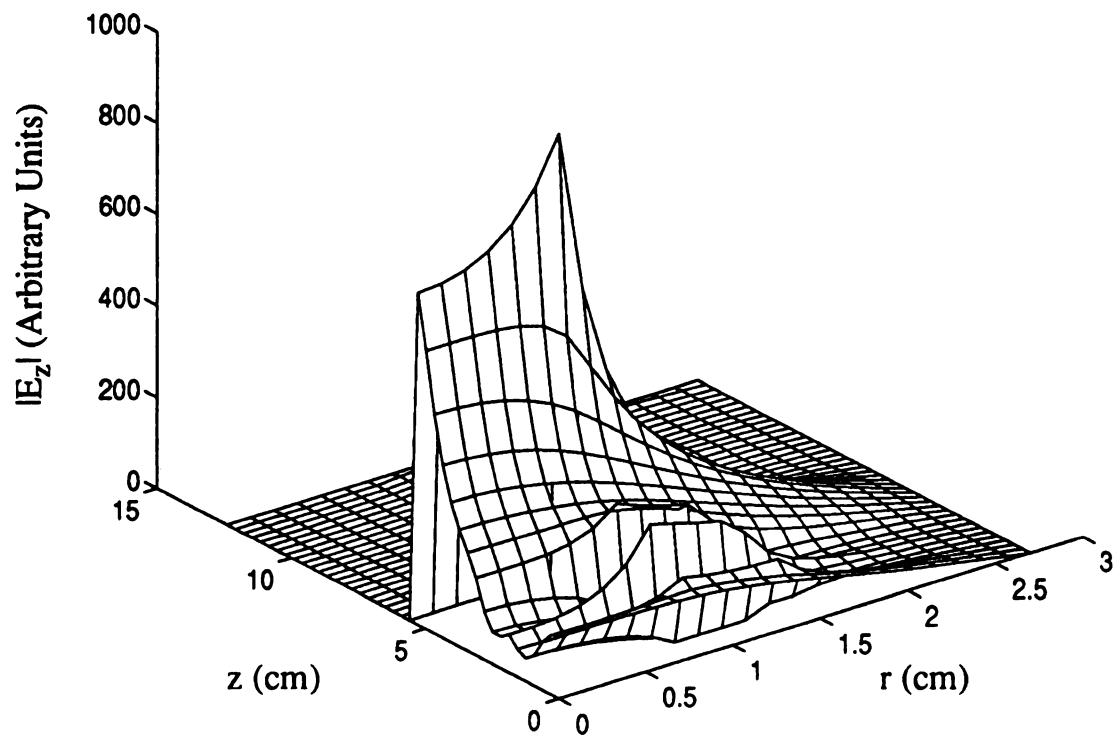


Figure 4-25: $|E_z|$ (arbitrary units) versus r and z for the compact ion source operated with a helium plasma discharge.

electromagnetic field distributions of empty cavities and the natural frequency responses of lossy cavities. The application of transient simulations to two different plasma sources was detailed.

Chapter 5

Steady State Simulation of Electromagnetic Fields Inside Plasma Loaded Microwave Resonant Cavities

5.1 Introduction

In Chapter 4, all the electromagnetic field simulations of empty or lossy-loaded cavities were based on transient state solutions, i.e., the source is turned off after several microwave cycles. An alternative simulation approach is the steady state method where the source is always on. This approach can not be used inside an ideal empty cavity because no losses exist. However, if a loss is present inside the cavity, it is possible to get a steady state excitation when the input power (from the source points) is equal to the power absorbed by the lossy material. For steady state solutions, the source points which were described in Chapter 4 are kept oscillating all the time at a frequency equal to or close to the natural frequency of the lossy loaded cavity. The stored energy increases and achieves a steady state when the total stored energy is a constant versus time. This occurs when the rate of power absorption matches the power input. One example is given in Figure 5-1. The excitation mode, the cavity and the cavity load size are the same as that used in natural frequency simulations discussed in Section 4.3 (see Figure 4-10). For the data shown in Figure 5-1, the lossy material had $\sigma = 1.0$ and $\epsilon = 3.0\epsilon_0$.

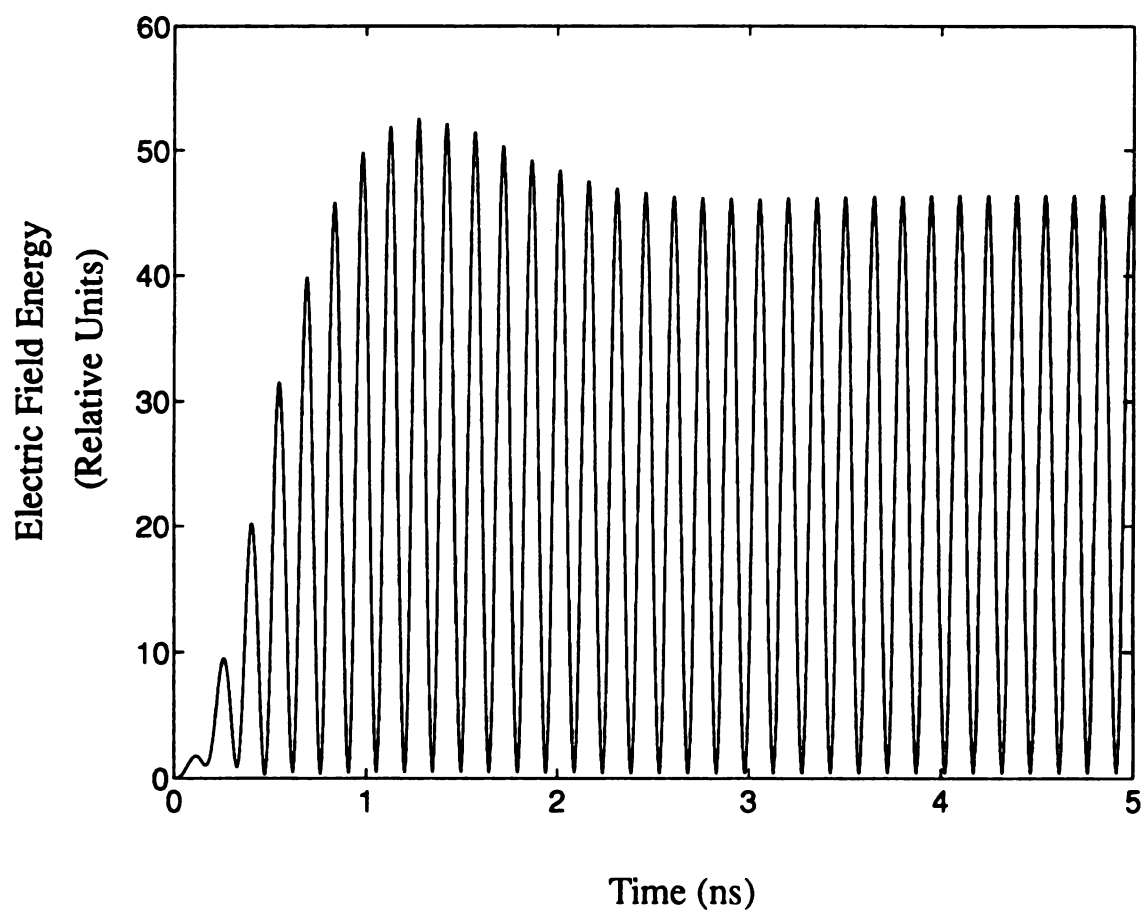


Figure 5-1: Steady-state response of the electric field energy, $\frac{1}{V} \int_V \epsilon_0 E^2 dV$, versus time, for the TE_{011} mode.

Another consideration for plasma-loaded resonant cavity simulation is the method of exciting the fields. For a microwave resonant cavity, the electromagnetic fields in the cavity are excited by an external circuit or waveguide, by means of coaxial-line probes, loops and small apertures. Moreover, the input power tuning (or matching) methods are important to adjust the cavity input impedance and control the microwave power reflected from the cavity.

In this chapter, the steady state electromagnetic excitation of discharge loaded microwave plasma reactors is numerically modeled including the input power coupling structure. The inclusion of the input coupling structure, which must be terminated in the simulation at some position, creates an open boundary in the simulation. For this open boundary, a non-reflecting (absorbing) boundary condition is used for truncation of the grid points in the FDTD model. The methods to excite input electromagnetic wave for simulation and to evaluate net power coupling into the plasma-loaded cavity are investigated. The simulation results of microwave discharge reactor sources used for diamond film deposition will be provided. For simplicity, the discharges used in this chapter are assumed to be a uniform, cold plasmas by using the simple conductivity model discussed earlier in Chapter 2. The self-consistent plasma model which is coupled with the steady state electromagnetic model will be present later in Chapter 6. The techniques used to experimentally determined the electromagnetic mode and cavity factor Q are introduced here and also in Chapter 6.

5.2 Non-reflecting boundary conditions

The simplified geometry for plasma cavity plasma reactor simulation in this study has been shown earlier in Chapter 2 (Figure 2-1). The electromagnetic waves are coupling into the cavity via an input coaxial probe. The plasma confined in the quartz chamber can be treated as a lossy material. The cavity walls serve as electromagnetic boundaries where only perpendicular electric field components can exist based on perfectly conducting wall assumptions. All the electromagnetic waves propagate to this boundary will be totally reflected under this assumption and no field can penetrate through these boundaries. Therefore, the grids used for FDTD simulation can be truncated at these region because no wave or field can exist outside these boundaries. However, at the input end of the coaxial probe is an open boundary, i.e., the domain in which the field has to be computed is unbounded. The electromagnetic waves, either incident or reflected, do exist outside this boundary and the number of grids needed for simulation becomes unlimited. Therefore, at this open boundary a truncation method must be used for limiting the domain in which the field is computed. Moreover, this method has to prevent any artificial reflection of the outgoing wave. Boundary conditions of this type are called absorbing boundary conditions, or non-reflecting boundary conditions. This absorbing boundary condition has been investigated extensively in solving electromagnetic wave scattering problems [13][14][15]. One technique which is widely used is provided by Mur [15].

From the FDTD cell shown in Figure 2-2, it can be found that all components of the electric field vector E applied to a particular point on the boundary of the mesh are tangential to this boundary while the relevant components of the magnetic field vector H are normal to it. For grid points on the mesh boundary, the E field components which are

tangential to the boundary plane cannot be evaluated by the finite-difference techniques since this would require \mathbf{H} field components that are outside the mesh. Therefore, the non-reflecting boundary conditions for Maxwell's equations on the mesh require the boundary conditions for the electric field components tangential to the boundary surface. Mur proposed that each of the \mathbf{E} field components satisfy the three-dimensional scalar wave equation independently

$$\left(\frac{\partial^2}{\partial x^2} + \frac{\partial^2}{\partial y^2} + \frac{\partial^2}{\partial z^2} - c^{-2} \frac{\partial^2}{\partial t^2} \right) W = 0 \quad (5.1)$$

where W is the \mathbf{E} field component and c is the wave propagation speed, which is equal to $1/\sqrt{\epsilon\mu}$. Assuming that the mesh is located in the region $z \leq k_0$, and given the boundary conditions for the plane $z = k_0$, then a space-time plane-wave constituent traveling in the direction of increasing z , with inverse velocity components s_x, s_y, s_z such that $s_x^2 + s_y^2 + s_z^2 = c^{-2}$, can be written as

$$W = \text{Re} \left(\psi \left(t + s_x x + s_y y + \left(c^{-2} - s_x^2 - s_y^2 \right)^{1/2} z \right) \right) \quad (5.2)$$

with $\text{Re} \left(c^{-2} - s_x^2 - s_y^2 \right)^{1/2} \leq 0$, where ψ is a function of time. For this outgoing wave, the first-order boundary condition

$$\left(\frac{\partial}{\partial z} + c^{-1} \left(1 - (cs_x)^2 - (cs_y)^2 \right)^{1/2} \frac{\partial}{\partial t} \right) W|_{z=k_0} = 0 \quad (5.3)$$

would, for fixed values of s_x and s_y , determine a W on the outer surface that is consistent with an outgoing wave, i.e., it is absorbed. Assuming

$$\left(1 - (cs_x)^2 - (cs_y)^2\right)^{1/2} = 1 + O\left((cs_x)^2 + (cs_y)^2\right), \quad (5.4)$$

the first order approximation can be obtained as

$$\left(\frac{\partial}{\partial z} + c^{-1} \frac{\partial}{\partial t}\right) W|_{z=k_0} = 0. \quad (5.5)$$

For the grid termination structure shown in Figure 5-2, which is in three dimensional cylindrical coordinates, the finite-difference approximation of (5.5) can be derived using centered differences in both the space and time increments as

$$\begin{aligned} E_r^{n+1}(i, j, k_0) &= E_r^n(i, j, k_0 - 1) + \left(\frac{\Delta t}{\sqrt{\epsilon\mu}} - \Delta z\right) \left(\frac{\Delta t}{\sqrt{\epsilon\mu}} + \Delta z\right) \\ &\quad \times \left(E_r^{n+1}(i, j, k_0 - 1) - E_r^n(i, j, k_0)\right) \end{aligned} \quad (5.6)$$

and

$$\begin{aligned} E_\phi^{n+1}(i, j, k_0) &= E_\phi^n(i, j, k_0 - 1) + \left(\frac{\Delta t}{\sqrt{\epsilon\mu}} - \Delta z\right) \left(\frac{\Delta t}{\sqrt{\epsilon\mu}} + \Delta z\right) \\ &\quad \times \left(E_\phi^{n+1}(i, j, k_0 - 1) - E_\phi^n(i, j, k_0)\right) \end{aligned} \quad (5.7)$$

where k_0 is the grid terminating point in the z direction. Note that only two \mathbf{E} field components needed to be evaluated at the boundary since they are the only components tangential to the grid truncation plane, i.e., $z = k_0$ plane.

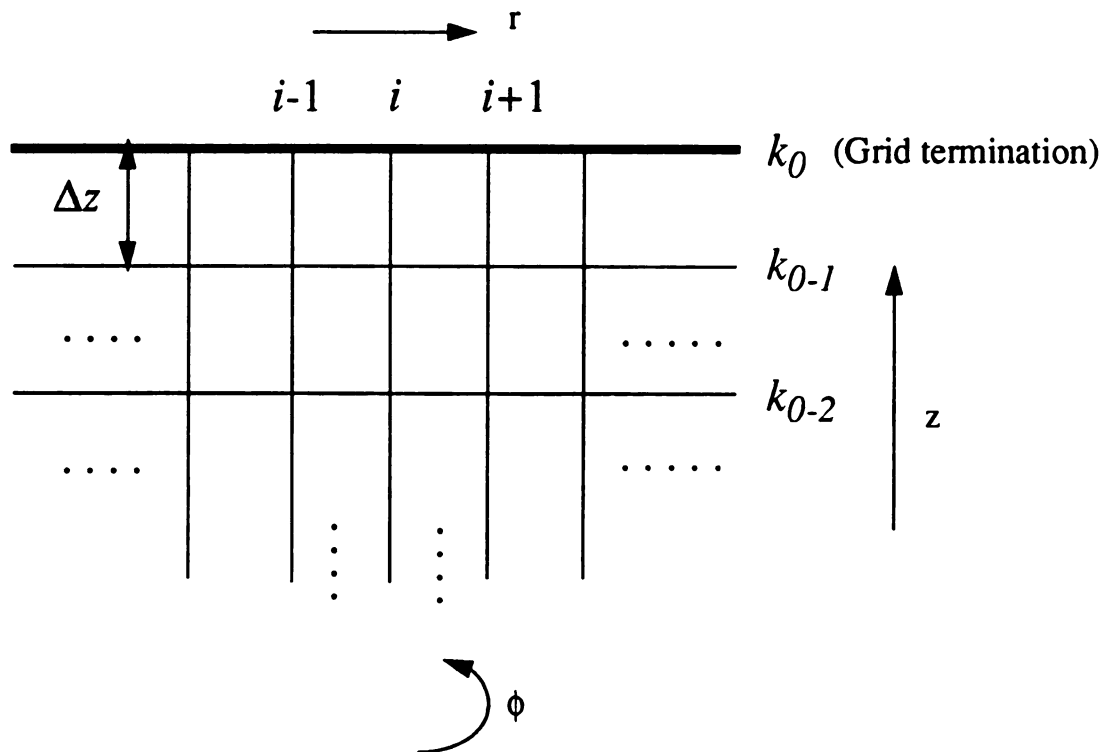


Figure 5-2: Grid termination structure.

5.3 Implementation for a coaxial waveguide

The non-reflecting boundary condition described in (5.6) and (5.7) was implemented in a coaxial waveguide in order to verify its validity and accuracy. The reason for using a cylindrical waveguide as the simulation structure is because the microwave input power coupling probe discussed in this study can be view as a cylindrical coaxial probe where the TEM mode electromagnetic waves propagate inside. The simulation structure for the cylindrical coaxial waveguide is shown in Figure 5-3. The coaxial waveguide (9 cm in length) consists of an inner cylindrical conductor and an outer conducting shell, and the electromagnetic waves propagate between these two conductors. The diameter for the outer shell is 9 cm, and for the inner conductor is 3 cm. The electromagnetic wave is excited at the $z = 0$ plane by assigning the time-varying electric field component at the grid points on this plane based on theoretical TEM wave solutions in a coaxial structure. The electric field for the TEM wave in a cylindrical coaxial waveguide has an E_r component only, which is constant in the z and ϕ directions and proportional to a $1/r$ variation in the r direction. The electromagnetic wave will then propagate to the end of the coaxial waveguide which is at the $z = 9$ cm plane, and be terminated by the boundary condition without any artificial wave reflection. One way to check the direction of wave propagation, as well as, the power flow is using Poynting's theorem:

$$W = \oint_s (\mathbf{E} \times \mathbf{H}) \cdot d\mathbf{s} \quad (5.8)$$

where W is the total power flow through a surface, S , which is the cross sectional plane of

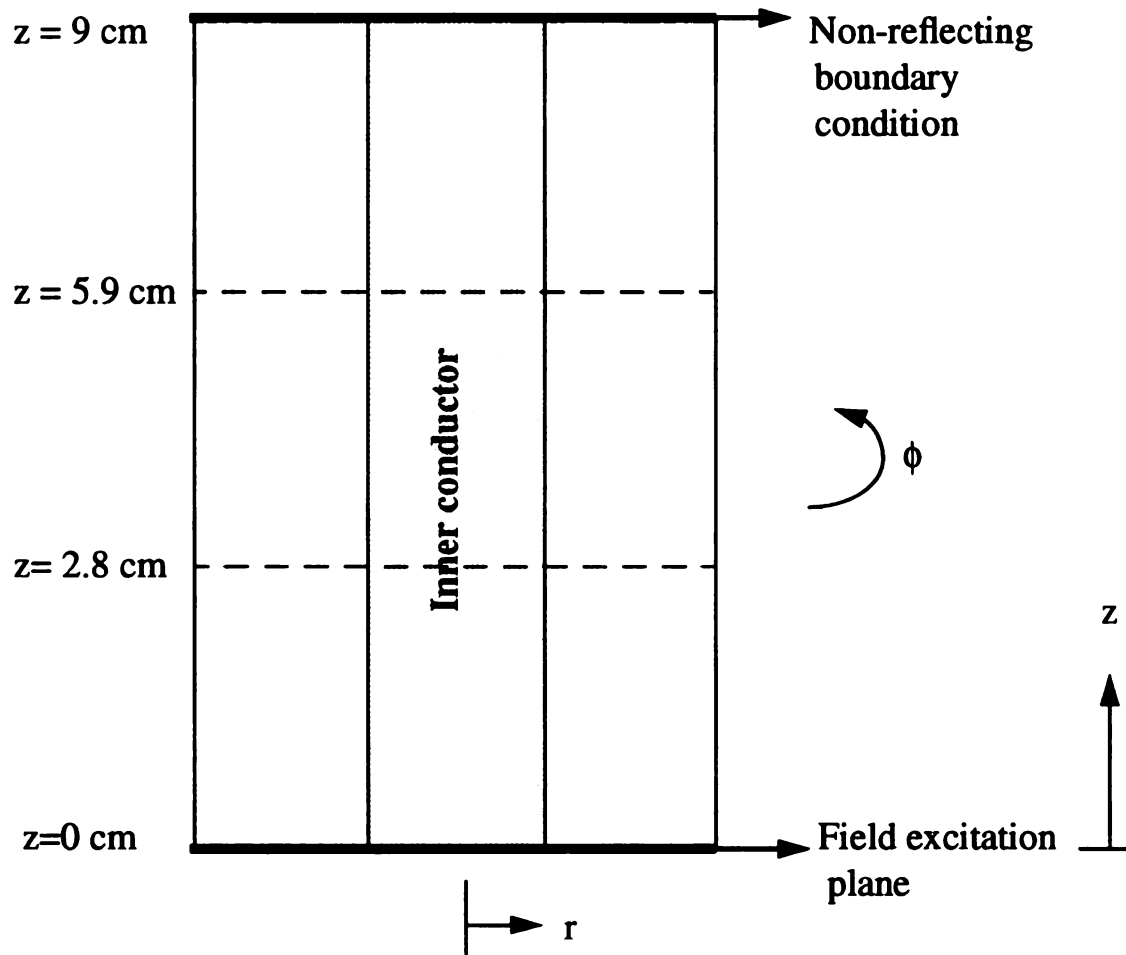


Figure 5-3: Simulation structure for the cylindrical coaxial waveguide.

the coaxial waveguide, such as the $z = 2.8$ cm and $z = 5.9$ cm planes shown in Figure 5-3. The direction of the surface S is toward the $+z$ direction for the power flow to the end of the waveguide.

The simulation grid structure is the same as shown in Figure 4-4, and the total grids are $30 \times 36 \times 30$ in r , ϕ and z directions respectively. The inner and outer conductors are assumed to be perfect conductors. The source points on the $z = 0$ plane oscillate at 2.45 GHz and the time step used here is one picosecond. The simulation results are obtained after several microwave cycles and are shown in Figure 5-4 and Figure 5-5. In Figure 5-4, the spatial average E_r field at the excitation plane ($z = 0$) kept the same shape and amplitude as the one on the absorption plane ($z = 9$ cm) all the time. These waveforms also kept a constant phase difference between the $z = 0$ and $z = 9$ cm plane due to the wave propagation distance of 9 cm. This shows that the waveform generated on the excitation plane propagated through the open end of the waveguide without any interference or distortion resulting from unwanted reflecting waves. Figure 5-4 also shows that the electromagnetic power flow through the waveguide is always positive, and the amplitude of the power flow is constant. This proves the power flow is toward the end of the waveguide and no other wave sources exist inside the waveguide and at the open boundary. Figure 5-5 shows the time-average spatial variation of the r component of the electric field. The E_r is constant in the z direction and follows a $1/r$ decay in the r direction, which is the same behavior as the theoretical TEM wave in a cylindrical coaxial structure [53].

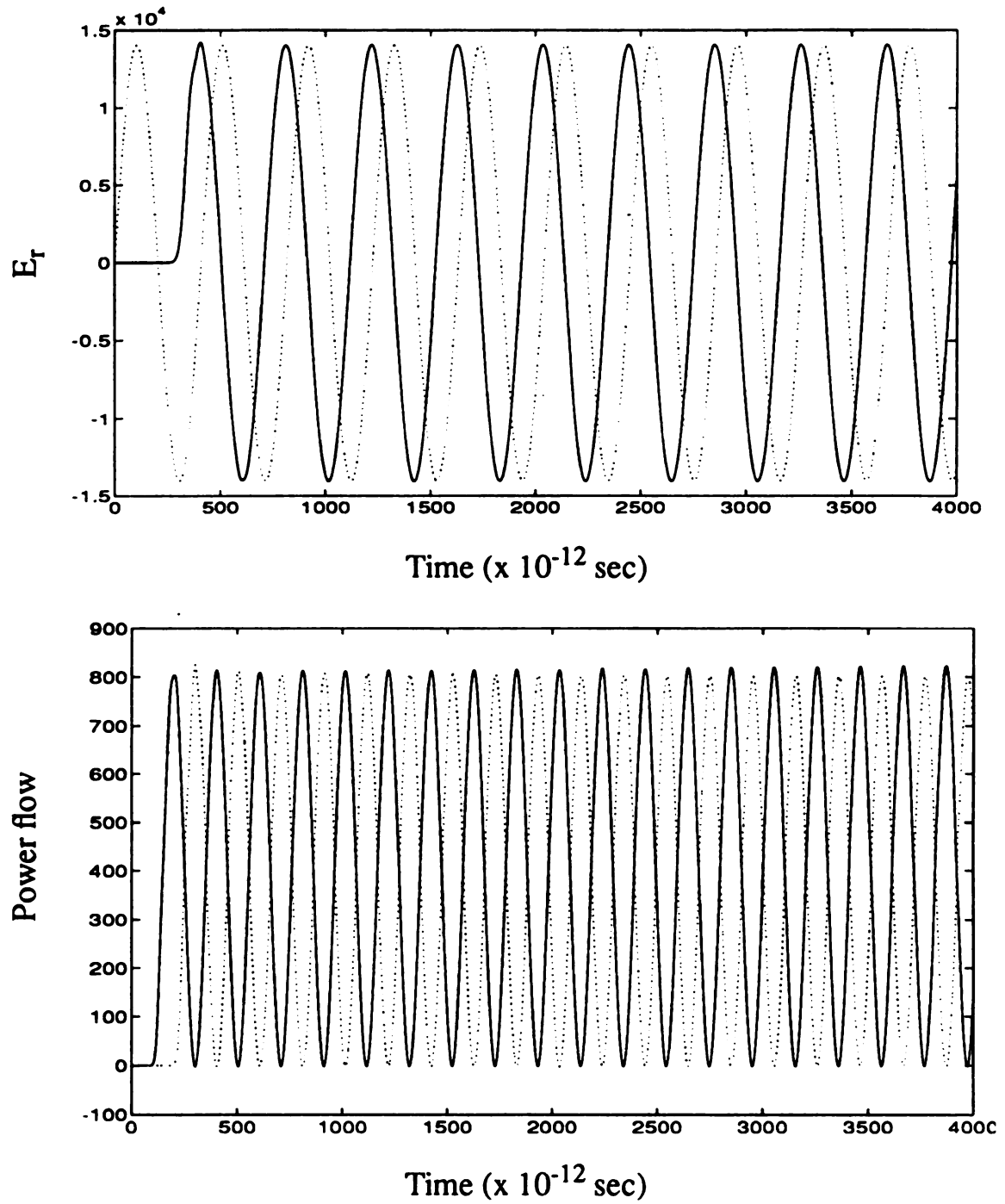


Figure 5-4: Non-reflecting boundary simulation results: (above) spatial average E_r vs. time at two different cross section (solid: $z=30$, dash: $z=0$). (below) spatial average power flow vs. time (solid: $z=10$, dash: $z=20$).

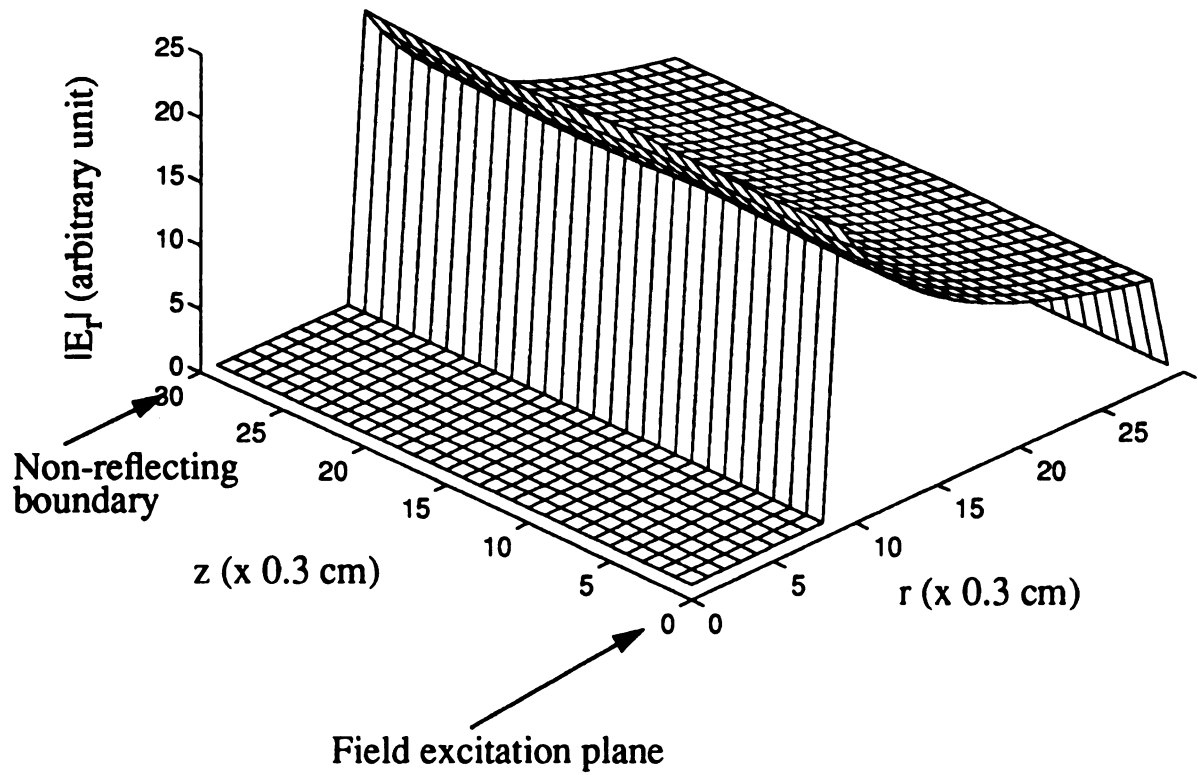


Figure 5-5: Spatial variation (r vs. z) of the $|E_r|$ component for the TEM mode in a cylindrical coaxial waveguide.

5.4 Implementation for a Microwave Cavity Plasma Reactor

The FDTD model is implemented for a microwave cavity plasma reactor such as used for diamond thin film deposition as shown schematically in Figure 5-6. This cylindrical microwave cavity plasma reactor has a symmetrical construction which can be excited in single electromagnetic modes. As shown, the reactor consists of a cylindrical sidewall which forms the outer conducting shell of the cavity reactor which has an inside diameter of 17.78 cm. The sliding short, the baseplate and the cavity sidewalls, form the cylindrical excitation cavity. Microwave energy at 2.45 GHz is coupled into the cavity through the coaxial input probe. The specific resonant mode is determined by the geometrical size of the cylindrical cavity and it can be adjusted by the movable sliding short. Generally, the electromagnetic resonant modes of this type of microwave cavity plasma reactor for diamond thin film deposition are TM_{01n} modes.

The simplified simulation structure of this reactor used in this section is shown in Figure 5-7. The cavity is assumed to be a simple cylindrical cavity with a movable sliding short on the top of the cavity. The short is used to adjust the height of the cavity (L_s) for cavity resonant condition control[1]. A coaxial probe structure, including the inner and outer conductor, are taken into account in the FDTD simulation region. The cavity sidewalls, bottom, sliding short and coaxial probe (both the inner and outer conductor) are assumed to be made of perfectly conducting material, so only the normal components of the electric fields exist on these surface. These surfaces make up the electromagnetic boundaries for the FDTD simulation model, and the only unbounded region (open boundary) is at the input end of the coaxial probe. The non-reflecting boundary condition discussed in the previous section is implemented at this boundary for grid truncation. The

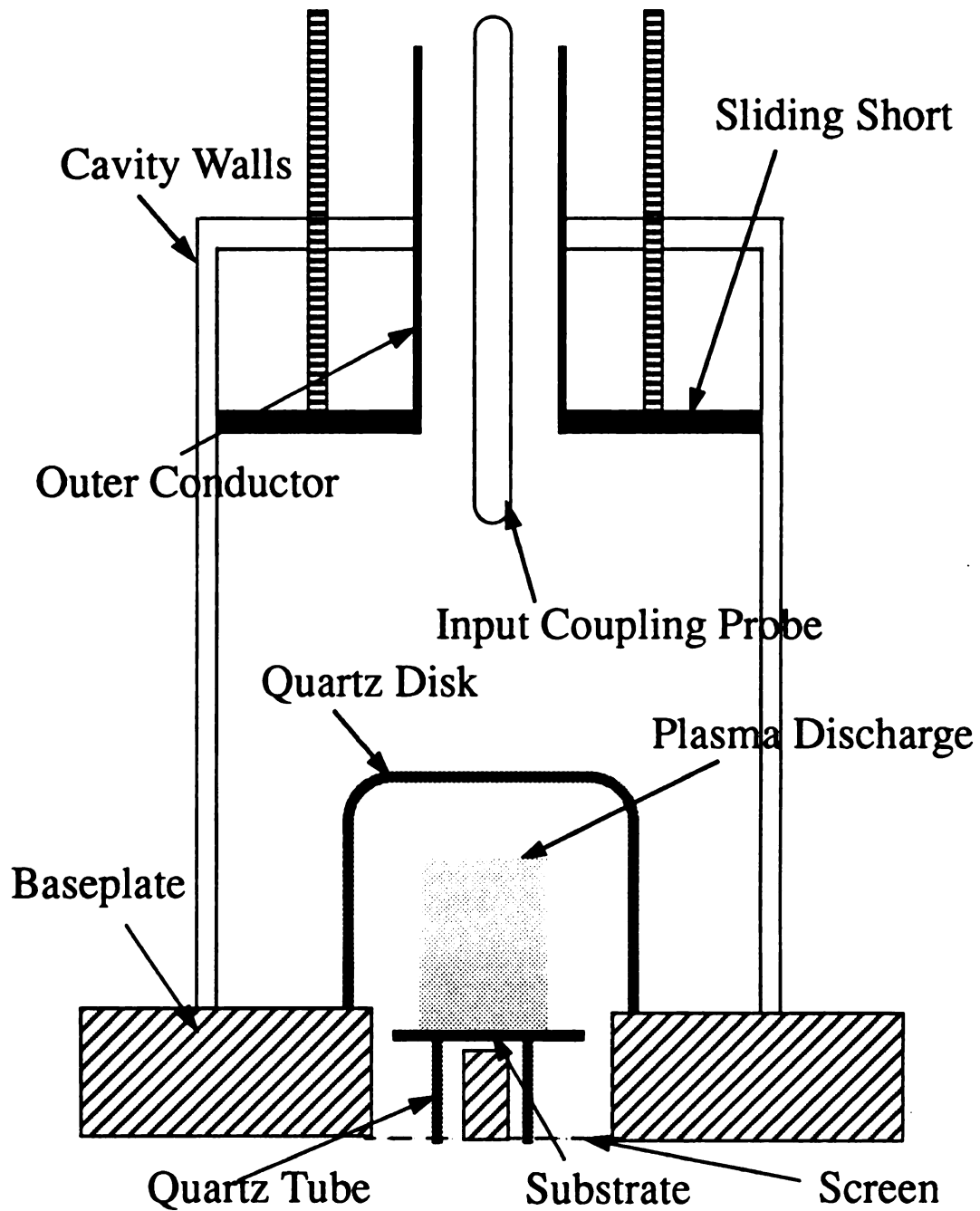


Figure 5-6: Configuration of a microwave cavity plasma reactor used for diamond film deposition. The cavity diameter is 17.78 cm.

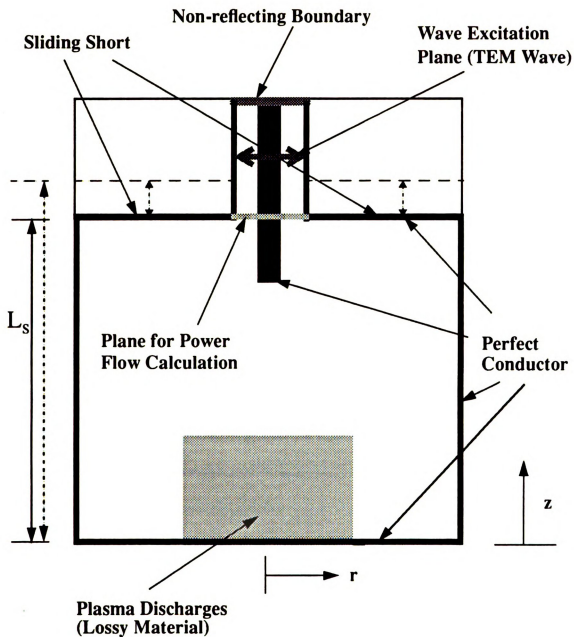


Figure 5-7: Simplified simulation structure for a microwave cavity plasma reactor.

plasma discharge region, at this point, is treated as a uniform lossy material with a specific assigned conductivity and a constant dielectric constant ($\epsilon=\epsilon_0$).

The major difference between this electromagnetic field model and the model discussed in Chapter 4 for cylindrical resonant cavity simulation is, instead of selecting several points inside the cavity region based on theoretical resonant cavity mode solutions for electric field generation, the electric field here is provided by the coaxial probe which is outside the cavity region. Hence, this method allows the simulation of the real electromagnetic coupling mechanism for discharge excitation in the microwave cavity plasma reactor. The technique used to excite the electromagnetic field in this numerical model is to select grid points on a cross sectional plane of the coaxial probe as source points and assign the time-varying electric field component at these points based on theoretical TEM wave solutions in a coaxial structure. The electromagnetic wave then propagates down into the cavity region where power is absorbed by the discharge. Any reflected electromagnetic wave will propagate to the end of the open boundary of the input power probe and be terminated by the non-reflecting boundary condition without producing any artificial wave reflection. In order to prevent the reflection of waves from the source points, the electric fields on the source points are assigned as [13]

$$E_r^{n+1}(i, j, k_1) = E_r^n(i, j, k_1) + C \sin(2\pi ft) \quad (5.9)$$

where C is the amplitude of the electric field source, k_1 is the grid points where the source plane is located, and f is the excitation frequency.

For the microwave cavity plasma reactor simulation discussed in this section, the inner diameter of the cavity is 17.78 cm, and the excitation frequency is 2.45 GHz. The

discharge (or lossy material) is located at the center of the bottom of the cavity and is assumed 8.85 cm in diameter and 2.0 cm in height. The conductivity and the cavity height are treated as input parameters to investigate the steady state electric field patterns and resonant characteristics of the loaded cylindrical cavity. The number of grids used in this simulation is 30 x 36 x 45 in the r , ϕ and z direction respectively, and the time step is 0.5 psec.

The simulation results of a 14.41 cm high cavity loaded with a 0.5 mho/m lossy material are shown in Figures 5-8 to 5-10. This height (14.41 cm) is basically the height for the theoretical TM_{012} mode in an empty cylindrical cavity with the excitation frequency and diameter mentioned previously. This empty cavity mode is described by equation (4.1). Figure 5-8 shows the electric field energy stored in the cavity versus time. After several microwave cycles, the power transfer to the cavity is equal to the power absorbed by the lossy materials. When this balance occurs, the amplitude of the electric field energy is constant and the system has reached its steady state. The spatial electric field distribution in the r - z plane are shown in Figure 5-9 and Figure 5-10. The simulation results are in agreement with the theoretical TM_{012} mode pattern as shown in Figure 5-11. Especially for the E_r component in the z direction, which follows a $\sin\left(\frac{2\pi z}{L_s}\right)$ variation profile as expected for the theoretical TM_{012} mode variation in the z direction. Inside the discharge region, the electric field strength decays due to microwave power dissipated in the lossy materials (or discharges). Moreover, the calculated E_r and E_z components are symmetric in the ϕ direction, and the E_ϕ components remain zero all the time during the simulation. Therefore, the three dimensional FDTD model used here can be further simplified to be a two dimensional model, that is, the simulation domain are considered in

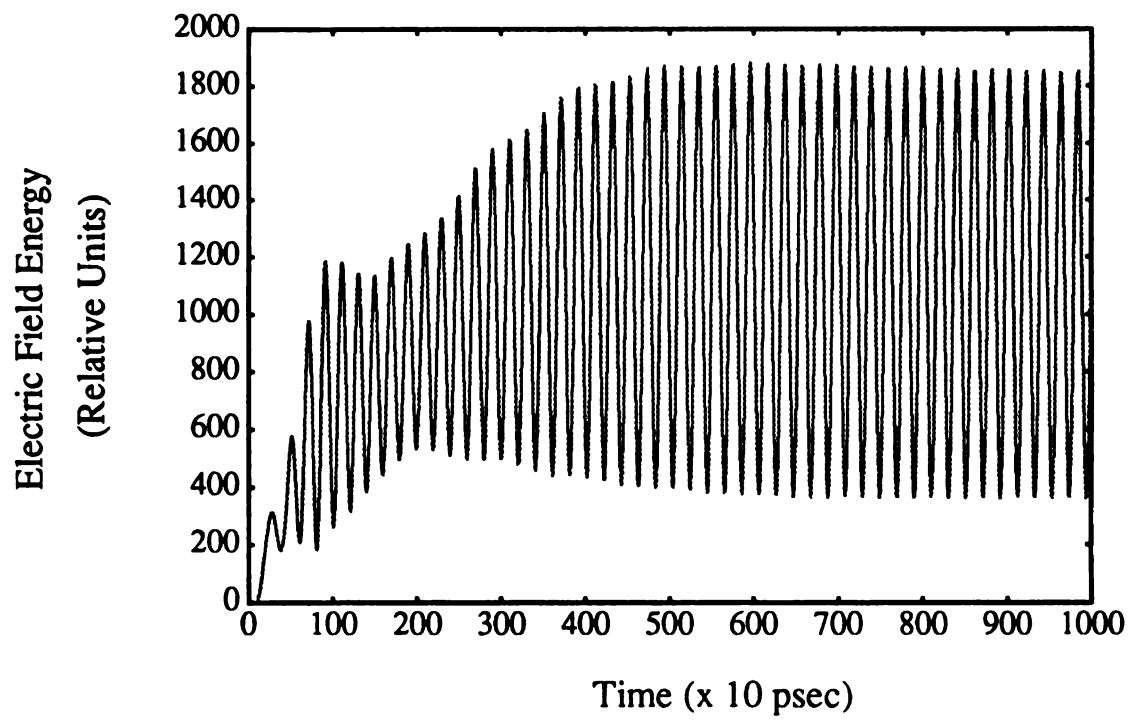


Figure 5-8: Electric field energy vs. time for TM₀₁₂ mode cavity simulation.

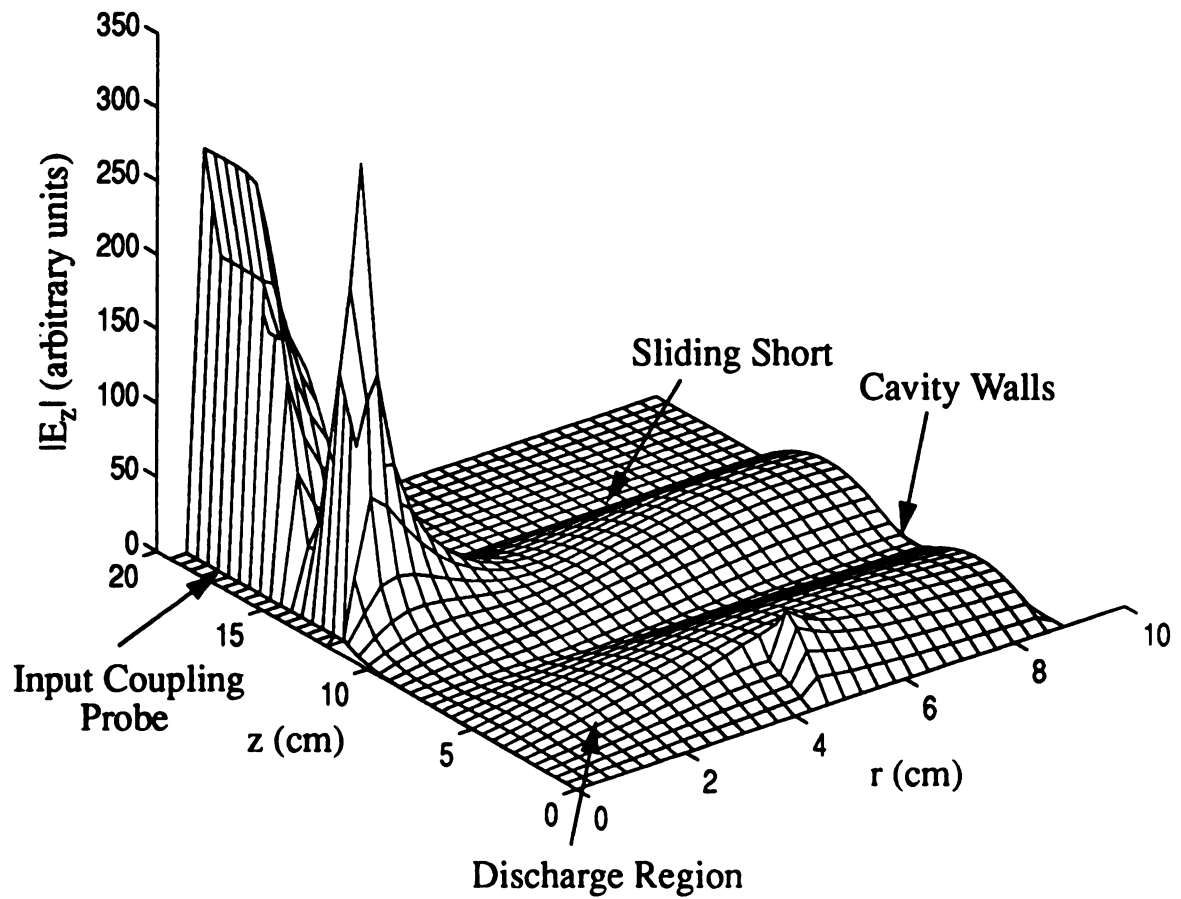


Figure 5-9: $|E_z|$ field distribution for a TM_{012} mode microwave cavity plasma reactor.

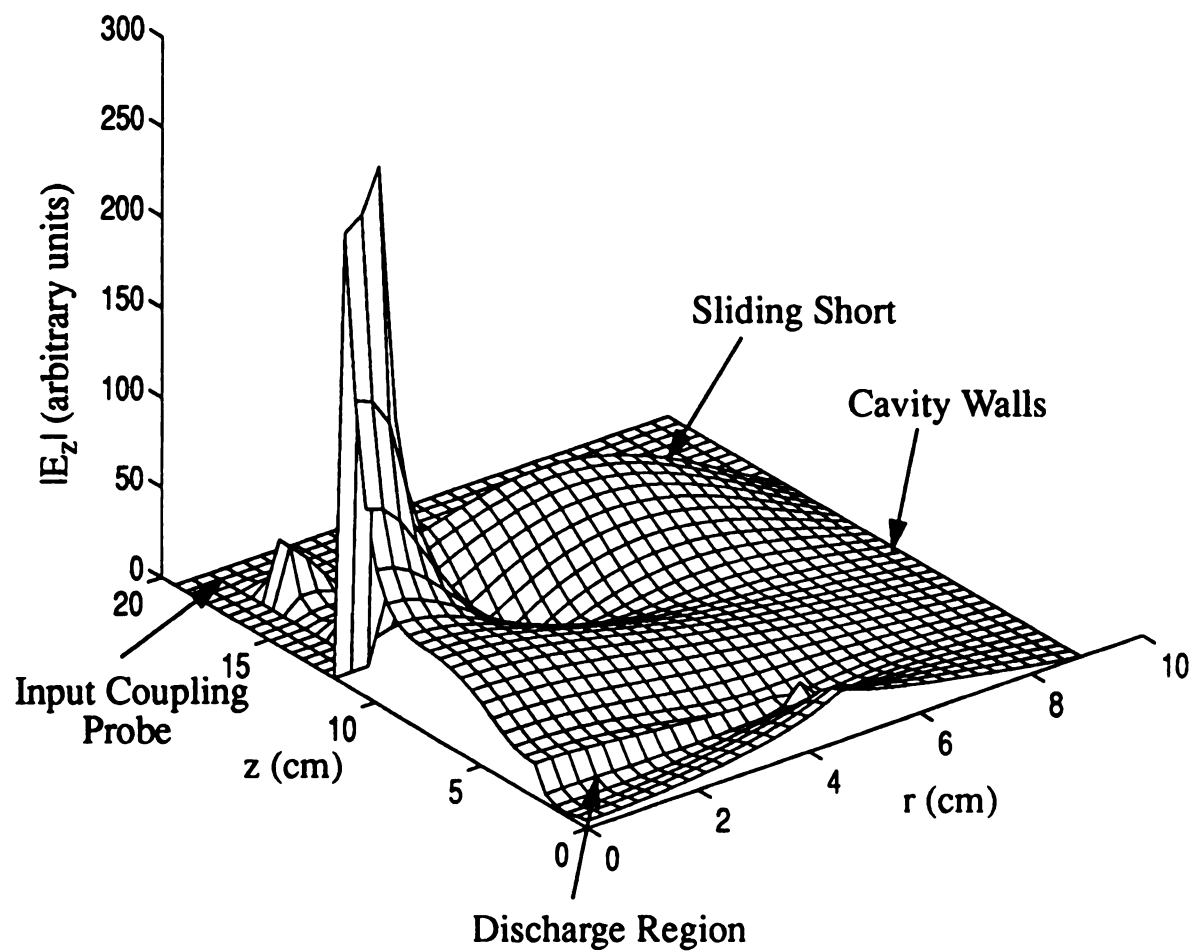


Figure 5-10: $|E_z|$ field distribution for a TM_{012} mode microwave cavity plasma reactor.

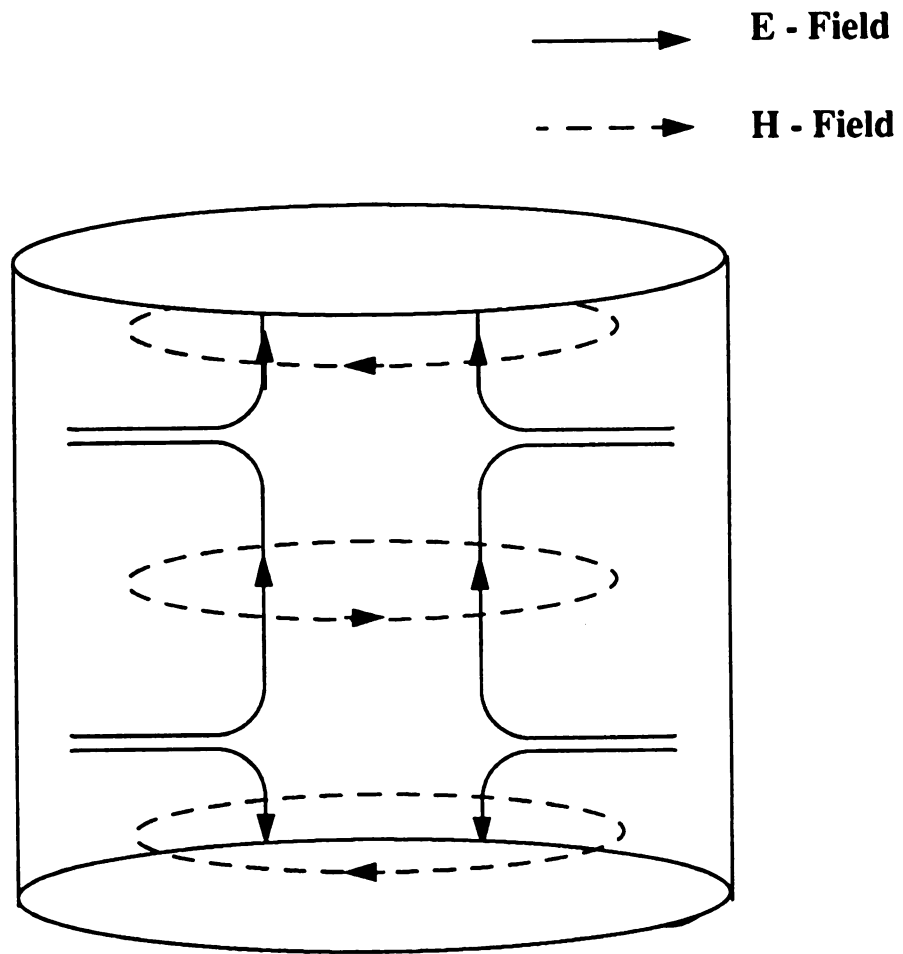


Figure 5-11: Field patterns of TM_{012} mode cylindrical cavity.

the r and z direction only. This model can be built based on solving the two-dimensional FDTD equations developed in Chapter 2 ((2.27) to (2.32)).

By using the two-dimensional FDTD model, the quality factor Q of the cavity, which is determined from the stored electromagnetic energy and the power absorbed by the lossy materials as discussed in Chapter 4, can be analyzed for various discharge conductivities and cavity heights. The simulation results of Q vs. cavity height for three different conductivity materials are shown in Figure 5-12. For a load with a given conductivity, the cavity Q changes as the cavity length varies. When the Q value drops, that means power is absorbed more efficiently by the lossy load. Figure 5-12 shows that the lowest Q value occurred at a cavity height of about 14 cm, which is close to the TM_{012} resonant empty cavity height of 14.41 cm. The lowest Q value doesn't exactly occur at the theoretical TM_{012} mode empty cavity height (14.41 cm) due to the loaded lossy material changing the resonant behavior of the cavity. This phenomenon has also been shown earlier in Figure 4-15, where the resonant frequency of a cylindrical cavity changes with the conductivity of material loaded inside the cavity. When the cavity height increases beyond 14 cm, the Q value increases, which means less power is coupled into the load and the more power is reflected from the cavity. The increase of reflected power is shown in Figure 5-13. The reflecting power is determined by using Poyting's vector in (5.8). The cross section plane used for determining the power reflected from the cavity is the open boundary surface and the direction of the surface is toward the $+z$ direction for the reflected power flow out of the cavity. When the height approaches 21 cm, the Q value drops again because the cavity is reaching another resonant condition, namely, TM_{013} mode, where the theoretical resonant cavity height is about 21 cm. Figure 5-12 also shows

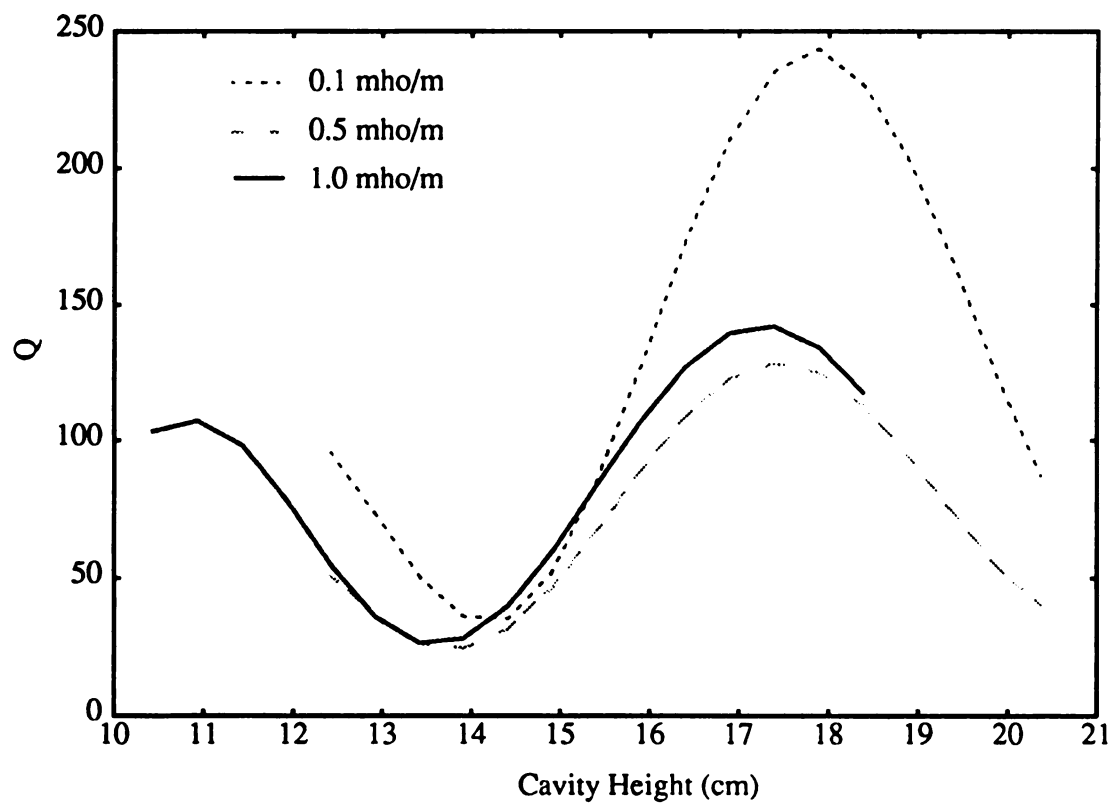


Figure 5-12: Q vs. cavity height for three different conductivity loaded TM_{012} mode cavity simulation.

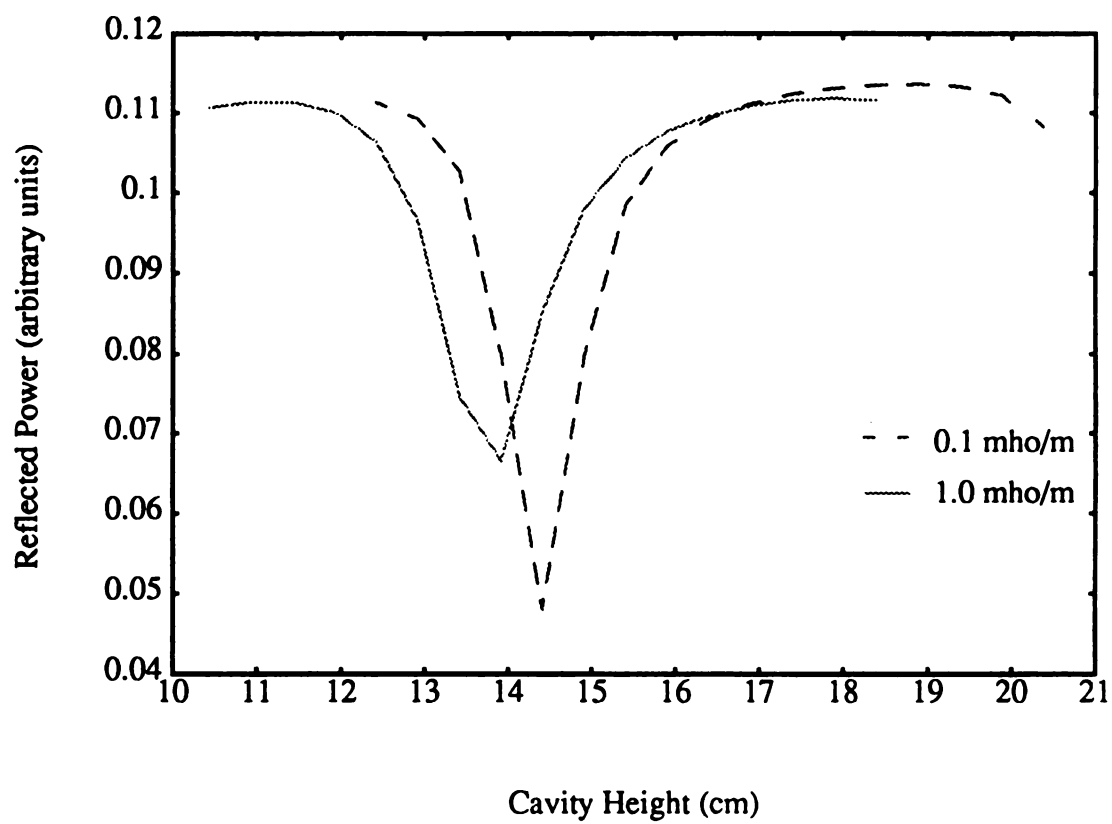


Figure 5-13: Reflected power vs. cavity height for TM_{012} mode cavity simulation.

the resonant behaviors for different conductivities. When $\sigma = 0.1$ mho/m, less power is absorbed by the loaded material, i.e., less perturbation for the resonant cavity, and the Q is higher and cavity height for resonant condition is about equal to that of the TM_{012} mode empty cavity. When σ increases, more power is absorbed by the loaded material. Therefore, the Q values drop, and the cavity height is starting to shift away from the empty cavity height in order to achieve the resonant condition for the lossy loaded cavity.

5.5 Simulation results for a cavity reactor loaded with a H_2 discharge

Another application made of this FDTD model was to simulate the power absorption and electric field distribution in a microwave cavity plasma reactor which was investigated by Zhang, et. al [3]. In Zhang's study, a 17.78 cm i.d. microwave cavity excited at 2.45 GHz was loaded by a hydrogen dominated plasma in a 9.25 cm i.d., 4.35 cm high quartz disk. The radial component of electric field strength at the cavity outer wall was measured by a micro-coax electric probe inserted through the cavity wall versus z and ϕ . The measured field distribution was compared with theoretical results to verify that the mode sustained in the cavity with the discharge present was approximately a TM_{011} mode. The discharge inside the quartz disk had volumes as estimated visually of 30 cm^3 to 100 cm^3 depending on the pressure which was varied from 20 Torr to 70 Torr. Zhang also found the quality factor, Q, of the cavity by measuring the absolute microwave electric field amplitude and the electromagnetic field mode distribution to determine the stored electromagnetic energy according to (4.2). The stored energy, U, and the input (or total absorbed) microwave power, P, then determined the Q value as $Q=\omega U/P$. In particular, Q values determined this way were about 60 and they varied little over the

pressure range studied (20 - 70 Torr). Additional details of the experimental Q value derivation and coax-probe calibration method will be discussed in next chapter.

The simulation structure of this reactor is shown in Figure 5-14, which is similar to the structure used in the previous section. However, in this section, the baseplate included in the numerical model is a more realistic reactor structure. The substrate holder is assumed to be aligned with the bottom surface of the baseplate, and to have approximately the same diameter as the quartz disk. Therefore, the sliding short, the baseplate, the substrate holder, the coaxial probe (both the inner and outer conductor), and the cavity sidewalls form the boundary of the FDTD simulation region. The boundary conditions for the electric fields on these surfaces and the open boundary condition are the same as in last section. A discharge is excited and sustained inside the disk-shaped quartz dome region by the input microwave power. Moreover, the quartz disk is included in this model and assumed lossless with a relative permittivity of $\epsilon_r = 3.78$.

The simulation of electromagnetic fields requires knowledge of both the electron density, n_e , and effective collision frequency, ν_{eff} , in order to solve the electron momentum transport equation and induced current density ((2.53) and (2.54)). A plasma discharge description which includes several idealizing assumptions has been adopted for this section. The discharge is assumed to have a cylindrical volume shape with a size found from visual observation. The density and effective collision frequency within this volume are assumed uniform. The idealizing assumptions ignore such behaviors as gas flow, non-constant plasma temperature profile and plasma density variations. Hence, care must be used in interpreting the simulation results in the plasma discharge on a local or small scale. However, the macroscopic quantities such as electromagnetic field mode, Q,

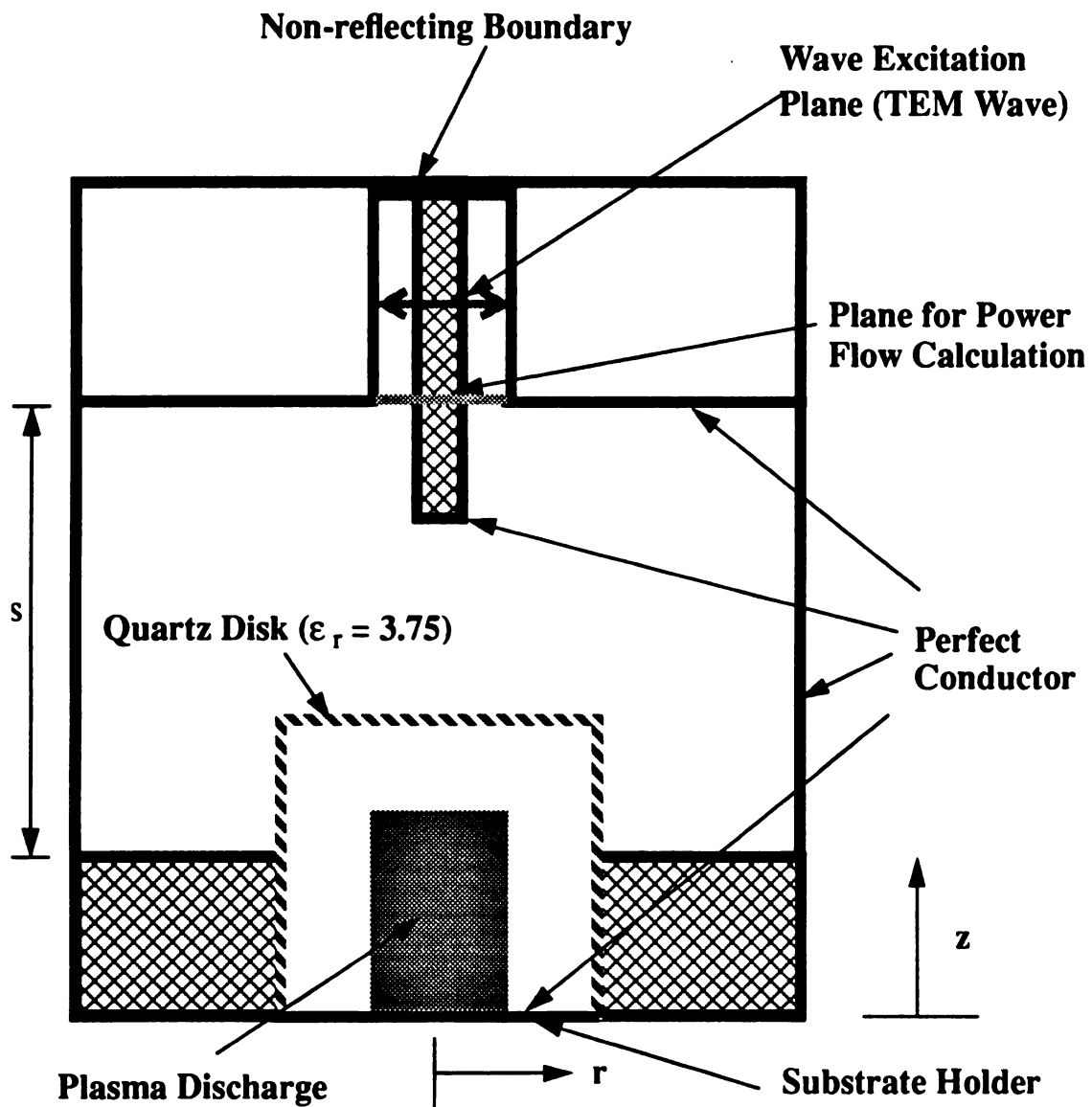


Figure 5-14: Simulation structure cross-section for microwave cavity plasma reactor.

and absorbed power are expected to be simulated accurately by using the measured values for plasma quantities. A more accurate plasma discharge model in the next chapter will remove this restriction.

From the measured gas temperature [54] and the corresponding gas pressure, the effective collision frequencies in hydrogen discharges at different pressures can be calculated approximately as $\nu_{eff} = 1.44 \times 10^{12} \times \frac{P}{T}$ (P is the pressure in Torr and T is the temperature in Kelvin) according to [50]. Treating the discharge volume, collision frequency and electron density (assumed uniform) as input data, the microwave absorption properties can be evaluated by (2.35), and the electric field distributions, power deposition distributions and the quality factor Q of the cavity are simulated using the FDTD model. By calculating the time average energy stored and the time-average power dissipated in the cavity using equations (2.35) and (4.2) after the simulation reaches steady state, a quality factor can be determined. Moreover, at steady state, the power dissipated in the cavity is equal to the net power transfer to the cavity, which can be calculated by Poynting's theorem given by (5.8).

For the hydrogen discharges in this study, the electron density has not been measured experimentally yet with high accuracy so it is treated as a variable parameter. The cavity quality factor Q is simulated versus electron density under different pressure conditions using the corresponding measured gas temperature and discharge volume. The results are shown in Figure 5-15 and Figure 5-16. These simulations are done by using the two-dimensional FDTD model since ϕ symmetry exists for the TM_{011} mode cavity. The Q values calculated by using either the power dissipation model (2.35) or the power flow model (5.8) are consistent with each other. For these simulations, when the electron

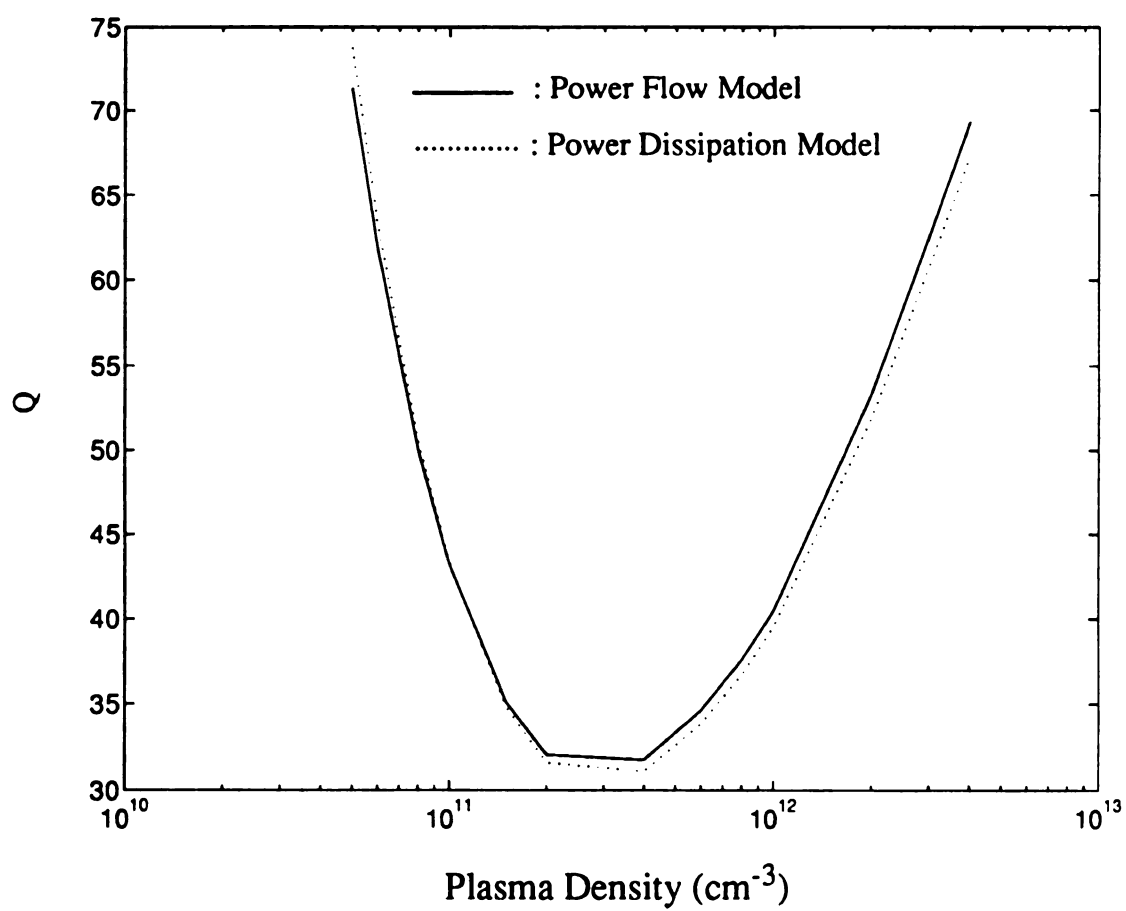


Figure 5-15: Q value vs. electron density at a pressure of 20 Torr.

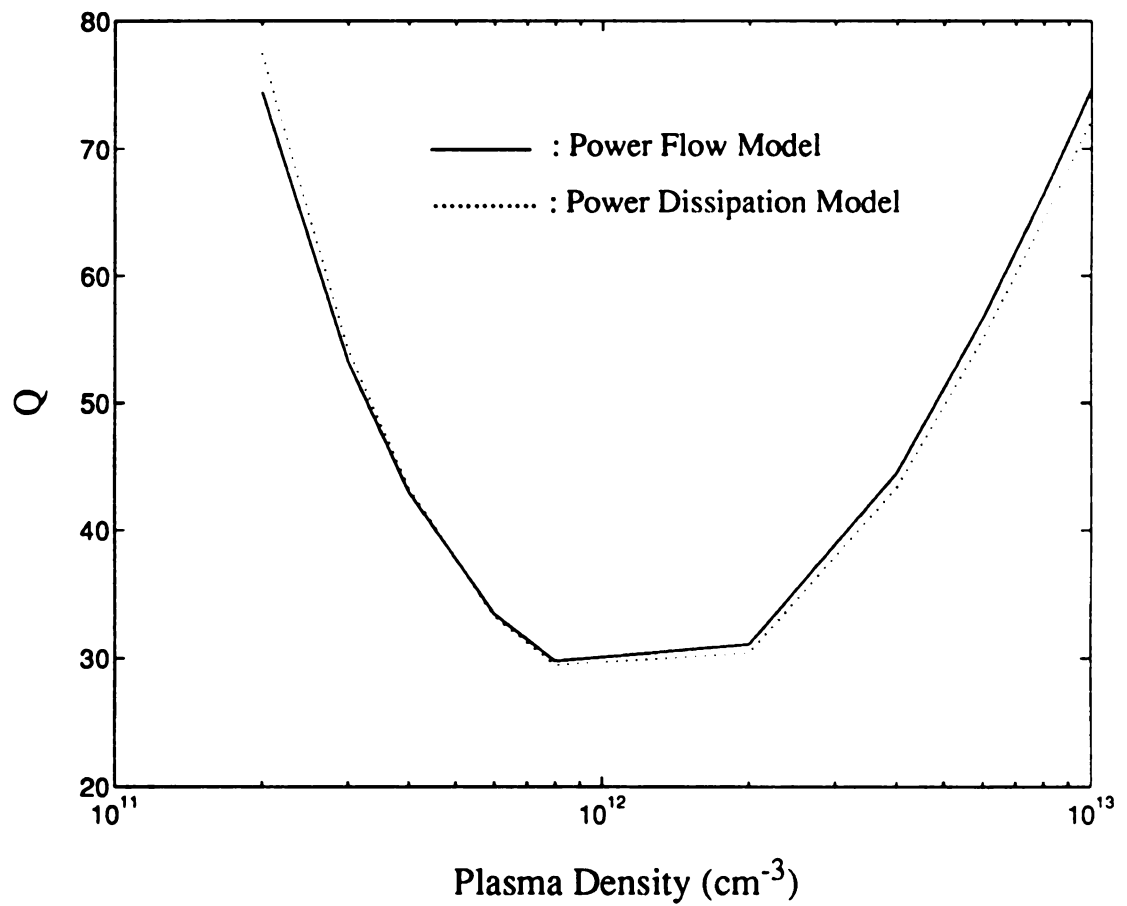


Figure 5-16: Q value vs. electron density at a pressure of 70 Torr.

density increases, the conductivity of the discharge increases. At lower electron densities the increase in conductivity results in increased total power absorbed. As the electron density increases further, the Q value reaches a minimum and then increases. The increase of Q occurs because the plasma has a high conductivity, and hence power absorption occurs primarily at the plasma boundaries and not throughout the entire plasma volume as the microwave skin depth decreases. The skin depth is defined as the depth at which the magnitude of the penetrating electric fields decrease to $1/e$ (about 36.9%) of their value at the boundary surface [53]. Following this definition, the skin depth can be obtained from the simulation data by examining the magnitude of electric field inside the discharge and at discharge boundary. For example the simulated skin depth for transverse waves is about 0.7 cm at a plasma density of $3 \times 10^{12} \text{ cm}^{-3}$. Theoretically, the skin depth δ for transverse waves penetrating into plasmas is given by [62]

$$\delta = c/\omega_{pe} \quad (5.10)$$

where ω_{pe} is the plasma frequency defined in (2.46). Equation (5.10) is valid under the assumption $\omega \ll \omega_{pe}$. For plasma density of $3 \times 10^{12} \text{ cm}^{-3}$, ω_{pe} is 9.75×10^{10} , then the skin depth is calculated to be 0.3 cm, which is on the order of the simulation result. By matching the calculated Q values with the experimental data (~ 60), the electron densities can be predicted around $3 \times 10^{12} \text{ cm}^{-3}$ at 20 Torr and about $8 \times 10^{12} \text{ cm}^{-3}$ at 70 Torr. At a Q value of about 60, the higher plasma density value is selected based on initial experimental measurements[54].

The spatial electric field distributions in the r-z plane are shown in Figure 5-17 to Figure 5-20 for the discharge maintained at 20 Torr with an electron density equal to $3.0 \times$

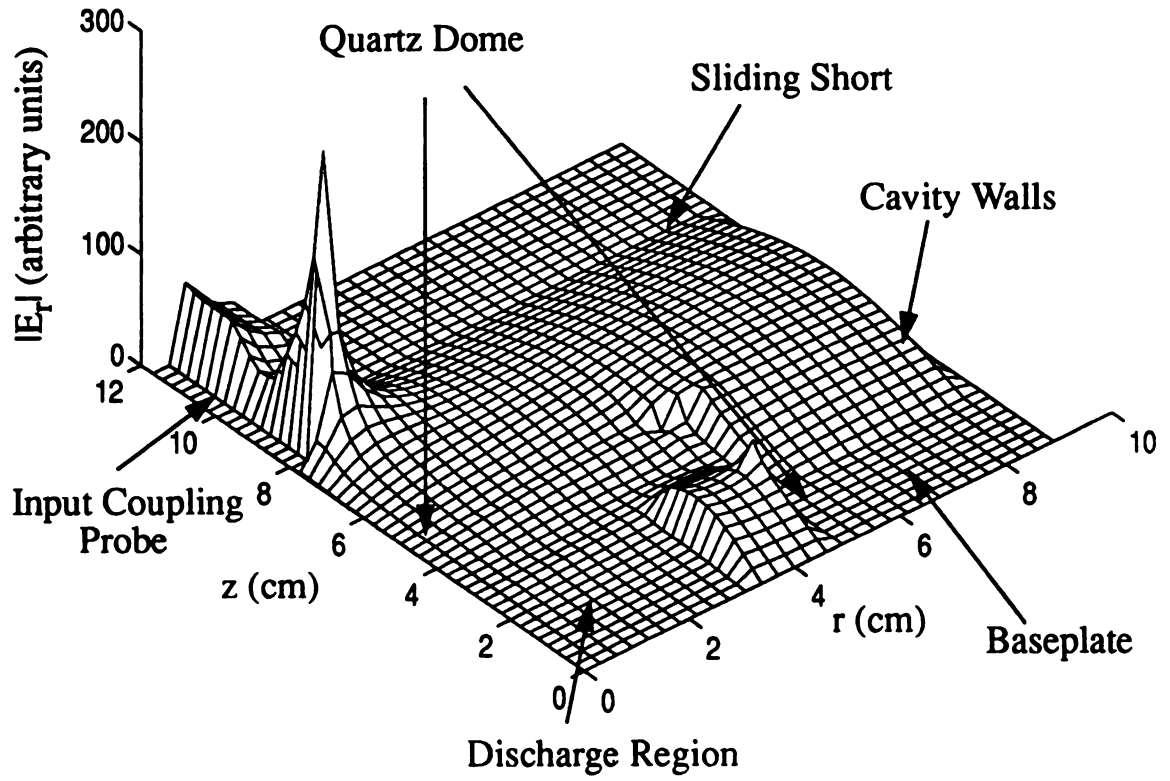


Figure 5-17: $|E_r|$ distribution in the $r - z$ plane at 20 Torr for a plasma density = $3 \times 10^{12} \text{ cm}^{-3}$.

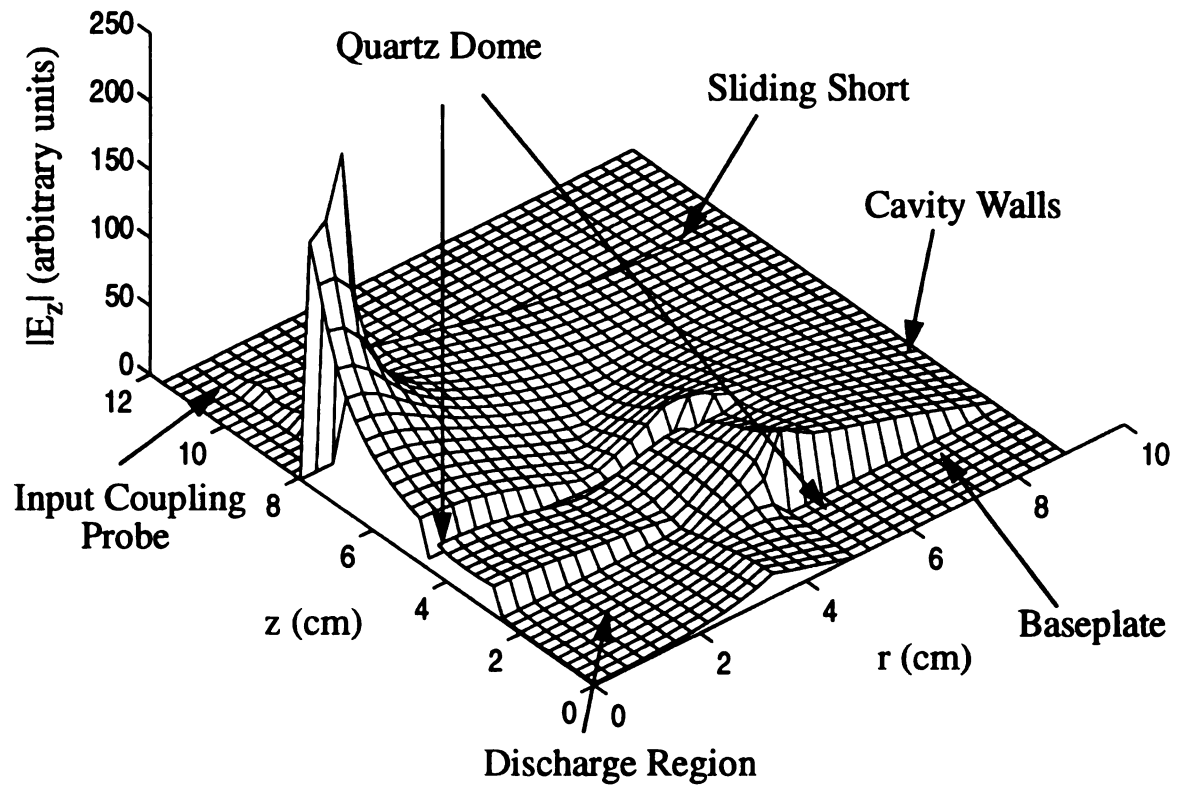


Figure 5-18: $|E_z|$ distribution in the $r - z$ plane at 20 Torr for a plasma density $= 3 \times 10^{12} \text{ cm}^{-3}$.

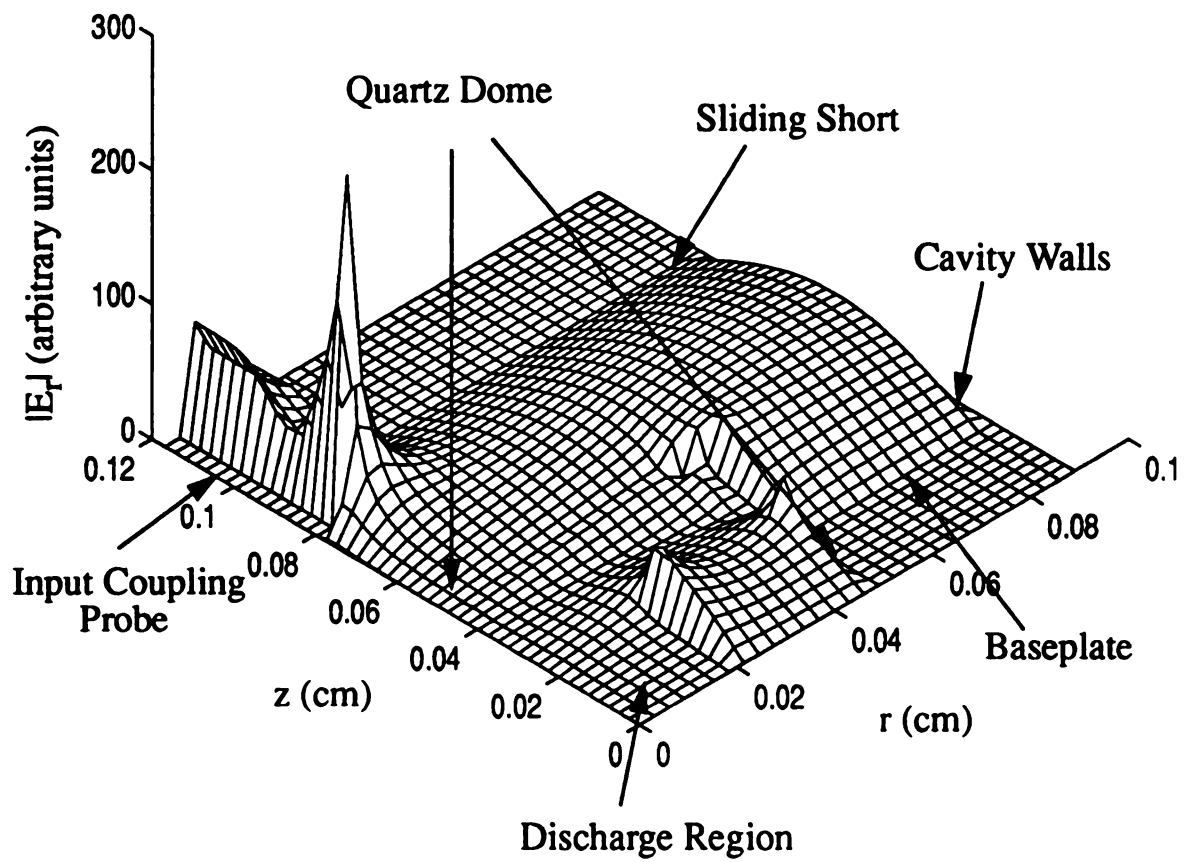


Figure 5-19: $|E_r|$ distribution in the $r - z$ plane at 70 Torr for a plasma density = $8 \times 10^{13} \text{ cm}^{-3}$.

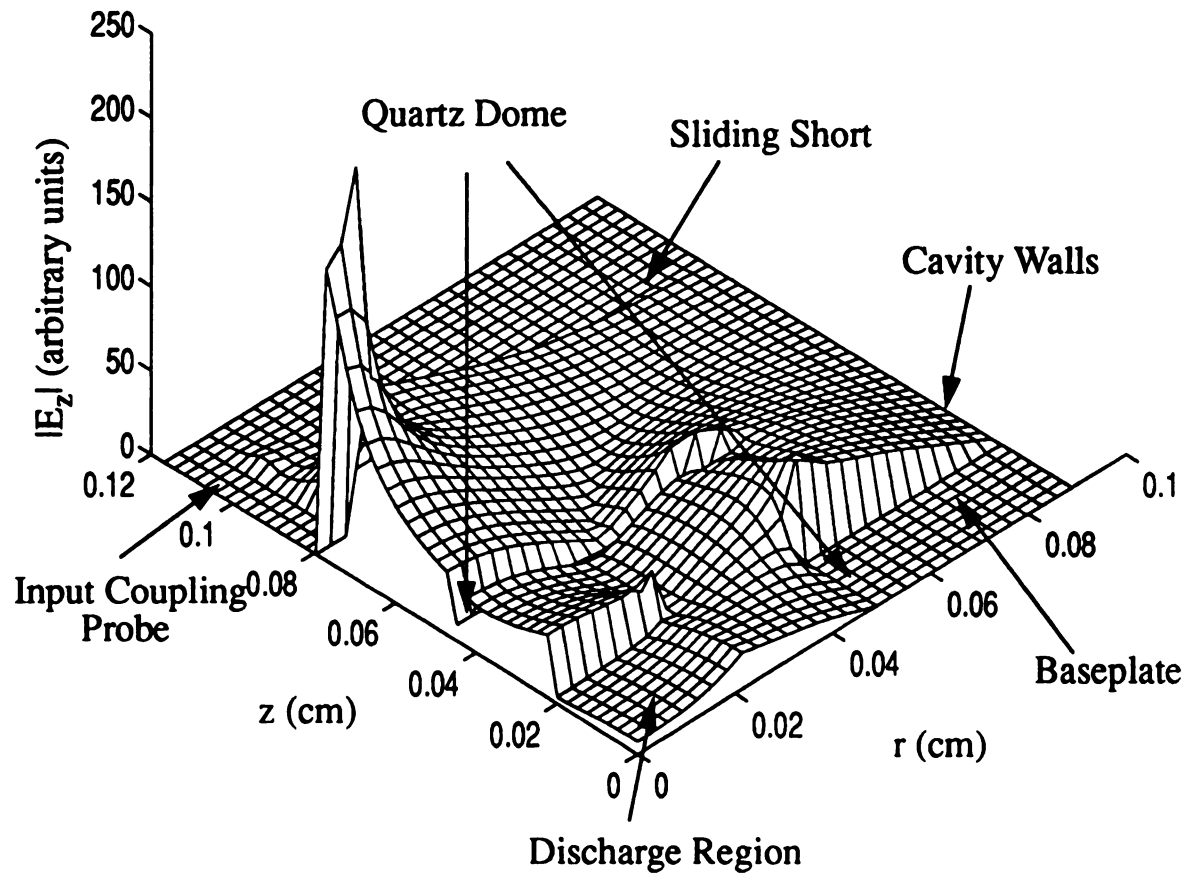


Figure 5-20: $|E_z|$ distribution in the $r - z$ plane at 70 Torr for a plasma density = $8 \times 10^{13} \text{ cm}^{-3}$.

10^{12} cm^{-3} , and for the discharge maintained at 70 Torr with an electron density equal to $8.0 \times 10^{13} \text{ cm}^{-3}$ respectively. The calculated E_r and E_z components are symmetric in the ϕ direction, and the E_ϕ components are zero during the simulation. The simulation is in approximate agreement with the theoretical TM_{011} mode wave pattern. In particular, from these figures, the distribution of E_r and E_z fields along the z and r directions are in approximate agreement with the theoretical electric field distribution for the TM_{011} mode which was the experimentally measured mode[3]. Due to the presence of the discharge, the electric fields decay further into the plasma region as microwave energy is absorbed by the plasma. Examples of absorbed power distribution for the substrate location indicated in Figure 5-14 are shown in Figure 5-21 and Figure 5-22 for 20 Torr and 70 Torr conditions respectively.

5.6 Conclusions

The FDTD numerical model has been applied to solve the steady state electromagnetic fields inside a plasma loaded microwave cylindrical resonant cavity in this chapter. The simulated structure included the input coupling power probe, as well as, the geometry of the base plate, substrate location, and quartz disk structure. The simulation results of a hydrogen discharge loaded plasma reactor, as compared to experimental data, showed good agreement for the electric field distributions. The FDTD electromagnetic model described in this paper will next be coupled with a more complete plasma continuum model to obtain a more accurate simulation of microwave plasma discharges, especially the spatial variations in the plasma. This self-consistent electromagnetic field and plasma model will be discussed in the next chapter.

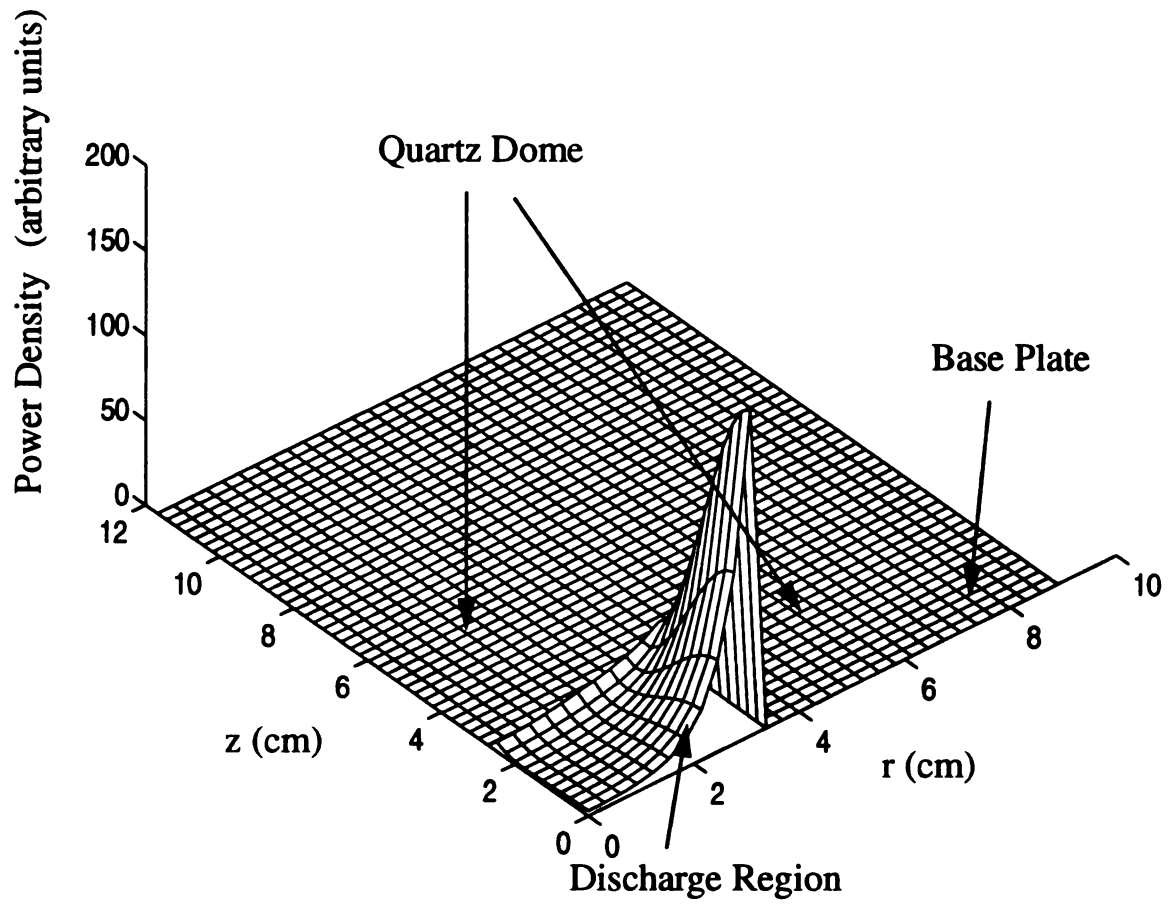


Figure 5-21: Power density distribution in the r - z plane at 20 Torr for a plasma density $= 3 \times 10^{12} \text{ cm}^{-3}$.

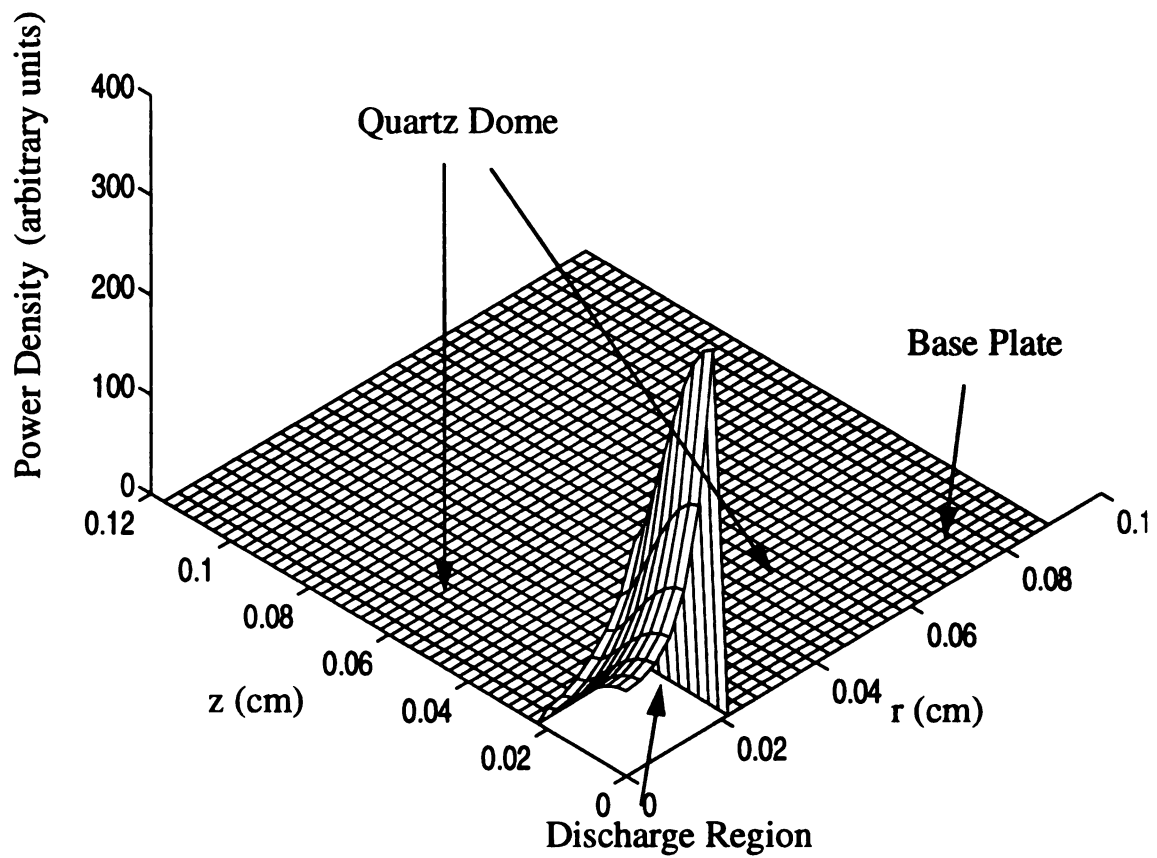


Figure 5-22: Power density distribution in the r - z plane at 70 Torr for a plasma density $= 8 \times 10^{13} \text{ cm}^{-3}$.

Chapter 6

Self-consistent Simulation of a Microwave Cavity Plasma Reactor

6.1 Introduction

In this chapter, a self-consistent model is presented which couples the FDTD electromagnetic field model and the fluid plasma model together in order to investigate the electromagnetic excitation of discharges inside a microwave cavity plasma reactor. The techniques used to coupling these two model are discussed in detail. The simulated plasma reactor is loaded with a H_2 discharge which is used for diamond thin film deposition. Simulation results are provided and compared with diagnostic results.

6.2 Model description

The numerical model used in this chapter for microwave cavity plasma reactor simulation combines the FDTD model described in Chapter 2 and the fluid plasma model described in Chapter 3. The FDTD model which solves the electromagnetic fields inside the discharges can provide output information such as the microwave power absorption of the discharges by using an appropriate plasma conductivity model. This absorbed microwave power is the input to the fluid plasma model, which is the heating term of the

electron energy balance equation (3.33). The discharge characteristics such as the plasma density and electron temperature are determined in steady state under this power absorption condition. The discharge characteristics information is then sent to the FDTD model to modify the plasma conductivity and calculate a new discharge power absorption. Therefore, in this iterative manner, the power absorbed by the discharges will converge to a stable value, and the electromagnetic fields inside the reactor source and the plasma characteristics can be solved self-consistently. The plasma conductivity model which is the link between the FDTD model and the fluid plasma model determines the relationship between the microwave field and induced microwave current inside the discharges. This relation can be determined by solving the electron momentum transport equation (Langevin equation) equations (2.39) and (2.40) in the time domain as stated in Chapter 2.

The fluid plasma model describes the characteristics of discharges by solving the steady state electron continuity equation, ion continuity equation, electron energy balance equation, and Poisson equation (3.30)-(3.36). Finite difference techniques are used to discretize these equations in cylindrical coordinates, and the resulting discretized equations were shown in (3.37)-(3.43). To solve these non-linear type, discretized equations, both direct method (Newton's method) and iterative method techniques are used (see section 3.4.2). In particular, the Poisson equation, electron continuity equation and ion continuity equation are tightly coupled and solved by Newton's method. The unknowns solved at each grid point are the electron density, ion density and plasma potential, and the electron and ion flux (steady state DC flux) can be determined by (3.34) and (3.35) using the solution of these unknowns. Then, the electron density and flux are coupled into the discretized electron energy balance equation (3.41) to solve the electron

temperature. Another input for the discretized electron energy balance equation is the absorbed microwave power density P_{abs} which comes from the FDTD electromagnetic field model. The calculated electron temperature is then feedback to the continuity equations and Poisson equation to modify the reaction rates and parameters and update the electron density, ion density, and plasma potential. The final stable solution of density and temperature is achieved by iteratively solving the continuity/Poisson equations and energy balance equation.

The flow chart of the microwave cavity plasma simulation is shown in Figure 6-1. The initial plasma density and potential data are determined by solving the Poisson equation and electron and ion continuity equations with some given constant reaction rates, such as the ionization rate and recombination rate. This information is coupled with initial absorbed microwave power, which might be assumed constant, to be the input data of the energy balance equation of electrons. Then, as previously discussed, the steady state electron density and temperature are determined by repeatedly solving the fluid plasma equations. These two quantities are then used to evaluate the microwave induced conductivity of the discharges in the FDTD model. Next, new power absorption data is obtained after a few microwave cycles of FDTD simulation, and it is coupled back to the fluid plasma model to update the plasma density and electron temperature. These processes form a closed loop and are repeated until the steady state absorbed microwave power converges to a stable value.

Since the solution of electron temperature and plasma densities are loosely coupled, the damping technique discussed in Chapter 3 is used during the simulation in order to prevent divergence phenomenon from occurring. The damping factors for

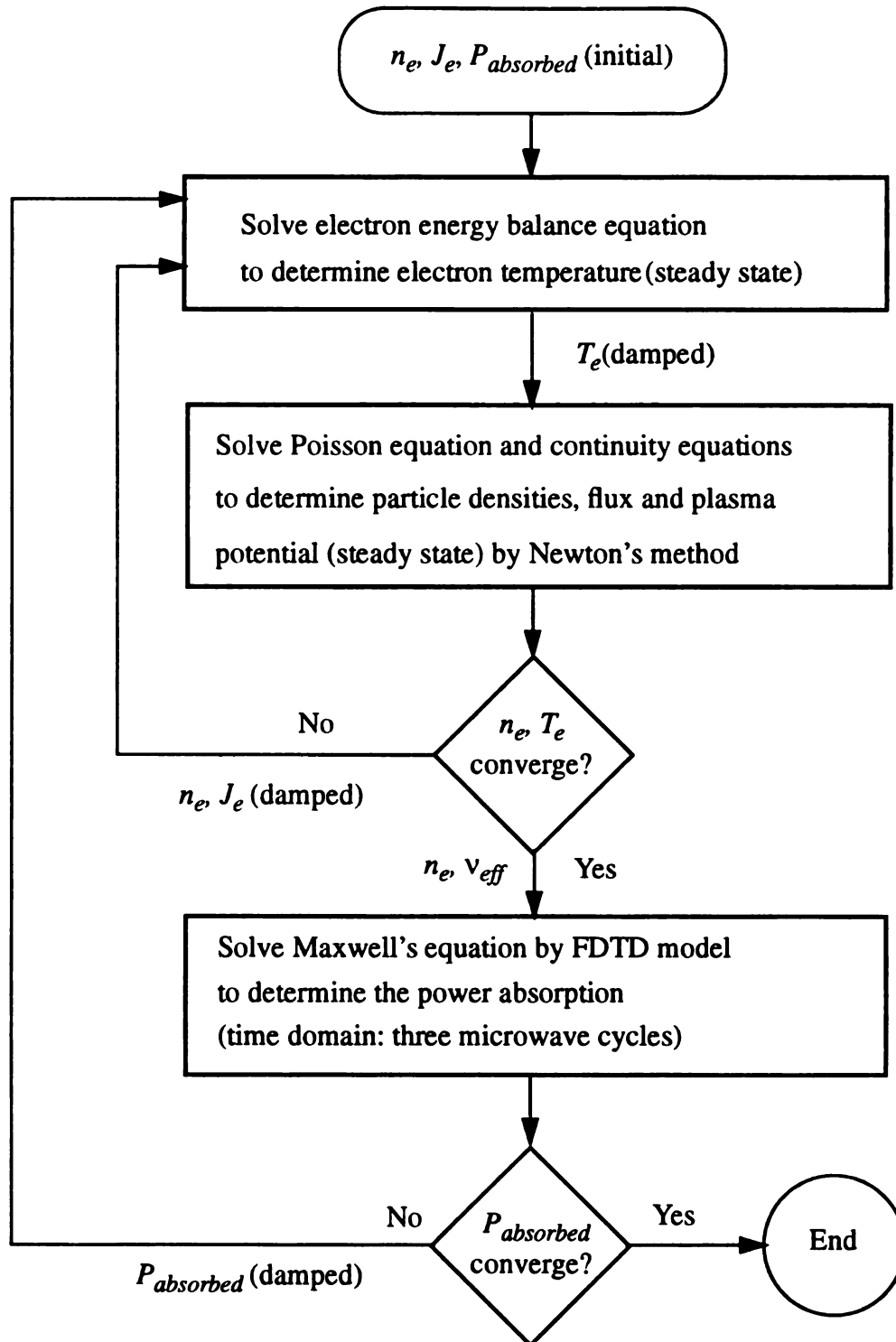


Figure 6-1: Flow chart for microwave cavity plasma reactor simulation.

electron temperature and density is normally 0.01, and might reduce to 10^{-5} if severe oscillation or divergence occurs. The damping factor of the absorbed power density, P_{abs} , which is the input to the fluid plasma model, is normally 0.1 to 0.01. For solving the Poisson equation and continuity equations, since they are tightly coupled by the Newton method, the damping factors are normally set to 1, and might be reduced to 0.01 if divergence occurs.

6.3 Reactor description and Q value measurement

The basic structure of the microwave cavity plasma reactor for diamond thin film deposition investigated in this chapter is similar to that in Chapter 5, which is shown in Figure 5-6. The inner diameter of the cavity is still 17.78 cm, but the height of the cavity, L , is usually adjust to 20.4 cm for TM_{013} mode excitation with 2.45 GHz input frequency. The plasma discharge is confined by a quartz disk which is 14.1 cm in diameter and 10.3 cm in high. The substrate holder and wafer size is 10.4 cm diameter, and the location of the substrate holder can be adjusted in the z direction.

The electromagnetic resonant mode and cavity quality factor Q for this cavity reactor are experimentally investigated by inserting a micro-coaxial probe into small holes drilled though the resonant cavity walls. The center conductor of the probe is inserted 2mm beyond the inside surface of the cavity side walls, and the other end is connected to a power meter during the experiment, as shown in Figure 6-2. This probe samples a small amount of electromagnetic power near the cavity inner side walls which can be measured by the power meter. Since the probe power reading is proportional to the square of the rms electric field strength normal to the inside cavity, the cavity resonant mode and the cavity

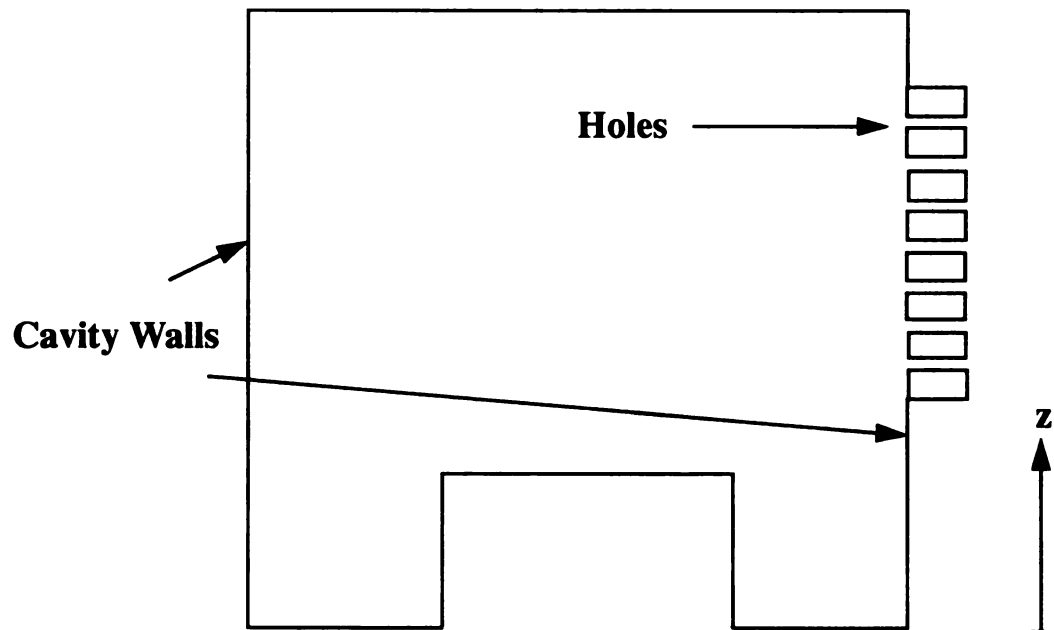
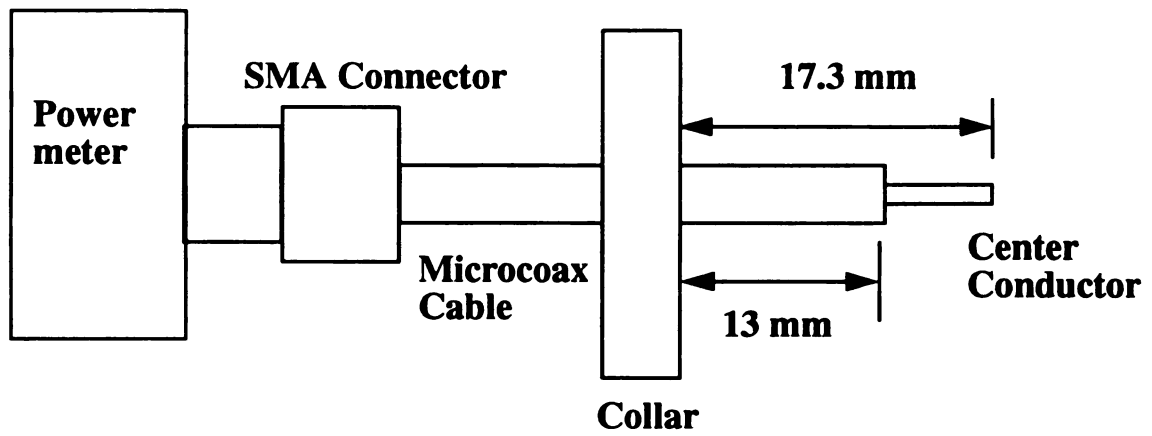


Figure 6-2: Microcoax probe and holes in the cavity walls.

stored energy can be determined using this techniques.

In order to establish the relationship between the power reading of the probe and the strength of electric field, a calibration procedure has to be performed. In this procedure, the calibration of the probe is done by using a 17.78 cm i.d. empty cylindrical brass cavity which is excited by a 2.45 GHz microwave frequency. This is the same brass cavity used on the diamond deposition system to take electric field measurements. The bottom of the cavity was covered with a brass plate in order to form a microwave resonant cavity. The cavity height is adjusted to 20.4 cm for TM_{112} mode excitation. The TM_{112} mode was selected since it gave the highest empty cavity quality factor (about 5000). This quality factor was determined by the resonant frequency f_0 and the bandwidth Δf of the reflected power measured from a frequency sweep of the resonant cavity, i.e., $Q = f_0/\Delta f$. By inserting the micro-coax probe into the hole at $z = 17.3$ cm above the cavity bottom surface on the cavity side walls, the probe power (P_p) was read from the connected power meter. In order to established the relation between the electric field strength E near the cavity inside cavity walls and the probe power reading P_p , the relationship between E at the probe sampling position on the cavity walls and the absorbed power P_a has to be first derived. The power absorbed by the empty cavity, P_a , is defined by $P_a = P_i - P_r$, where P_i is the incident power imparted to the cavity (approximately 100 mWatts) in this case and P_r is the reflected power from the cavity [48].

Using perturbation theory for the lossy conducting surfaces and assuming that the power absorbed by the empty cavity is dissipated on the cavity walls, the following power balance equation is established [49],

$$P_a = R \oint |H|^2 ds \quad (6.11)$$

where R is the surface resistance. For brass at 2.45 GHz excitation frequency,

$$R = 5.01 \times 10^{-7} \sqrt{f_0} = 0.0248. \quad (6.12)$$

For the TM_{112} mode, the components of the \mathbf{H} field are:

$$H_r = -A \frac{1}{r} J_1 \left(\lambda_{11} \frac{r}{a} \right) \sin(\phi) \cos \left(\frac{2\pi z}{L} \right) \quad (6.13)$$

$$H_\phi = -A \frac{\lambda_{11}}{a} J_1 \left(\lambda_{11} \frac{r}{a} \right) \cos(\phi) \cos \left(\frac{2\pi z}{L} \right) \quad (6.14)$$

and $H_z = 0$, where A is the amplitude constant, and λ_{11} is first root of the Bessel function J_1 . For $a = 8.85$ cm (cavity radius), $L = 20.4$ cm, and $\lambda_{11} = 3.83$, equation (6.11) can be evaluated by (6.12) to (6.14) giving

$$\begin{aligned} P_a &= R \int_0^{2\pi L} \int_0^a |H_\phi(r=a)|^2 r(d\phi) dz + 2R \int_0^{2\pi a} \int_0^L |H_\phi(z=0)|^2 r(d\phi) dr \\ &\quad + 2R \int_0^{2\pi a} \int_0^L |H_r(z=0)|^2 r(d\phi) dr \\ &= 0.3993A^2 \end{aligned} \quad (6.15)$$

This evaluation was performed using numerical integration. For a cylindrical cavity, the only component the electric field normal to the cavity side walls is the E_r field, which can be written for the TM_{112} mode as

$$E_r = -A \left(\frac{1}{j\omega\epsilon} \right) \left(\frac{2\pi}{L} \right) \left(\frac{\lambda_{11}}{a} \right) J_1 \left(\lambda_{11} \frac{r}{a} \right) \cos(\phi) \sin \left(\frac{2\pi z}{L} \right). \quad (6.16)$$

For $r = a$, $\phi = 0$, and $z = 17.3$ cm, (6.16) can be calculated to be:

$$|E_r|^2 \Big|_{r=a} = 1.0344 \times 10^7 A^2. \quad (6.17)$$

From (6.15) and (6.17), the relationship between the electric field strength E near the cavity inside walls and absorbed power is

$$|E_r|^2 \Big|_{r=a} = 2.59 \times 10^7 P_a. \quad (6.18)$$

Since the ratio of P_a to P_p , which is equal to 3243.24, is a constant, the relationship between the electric field strength E near the cavity inside walls and the probe power is obtained as

$$E^2 = |E_r|^2 \Big|_{r=a} = 8.4 \times 10^{10} \times P_p \quad (6.19)$$

where the unit of E is Volt/m and the unit of P_p is Watt.

After the probe calibration is completed, the electric field strength E near the inner side walls of the microwave cavity plasma reactor can be determined from the power reading of the micro-coax probe. Probe experiments are done by measuring the electric field strength at various z positions for the microwave cavity plasma reactor during diamond thin film deposition. The microwave excitation frequency is 2.45 GHz, and the cavity height is adjusted to a position near 20.4 cm for a minimum reflected power

condition. The result is shown in Figure 6-3 where the resonant condition for the microwave cavity during deposition process matches closely to the ideal TM_{013} mode. The field pattern for the TM_{013} mode is shown in Figure 6-4. Additionally, the electric field was probed circumferential around the cavity. The field strength showed no variation along the ϕ direction as expected for the TM_{013} mode.

The Q factor of the plasma discharge loaded cavity reactor can be estimated by calculating the electromagnetic energy stored in the cavity and the power dissipated in the cavity. The energy stored in the cavity is determined under the assumption that the electromagnetic fields are only slightly altered by the presence of the discharge and that the electromagnetic fields in the discharge are not much different from those when the discharge is not present. The electric field for the theoretical TM_{013} cavity mode is given by:

$$E_r = A \frac{\lambda_{01}}{j\omega\epsilon a} \left(\frac{3\pi}{L} \right) J_1 \left(\lambda_{01} \frac{r}{a} \right) \sin \left(\frac{3\pi z}{L} \right) \quad (6.20)$$

$$E_\phi = 0 \quad (6.21)$$

$$E_z = A \frac{\lambda_{01}^2}{j\omega\epsilon a^2} J_0 \left(\lambda_{01} \frac{r}{a} \right) \cos \left(\frac{3\pi z}{L} \right) \quad (6.22)$$

where λ_{01} is the first root of Bessel function J_0 , and A can be determined in (6.20) and (6.22) with the measured probe power P_p . Thus, the energy stored in the cavity can be determined by:

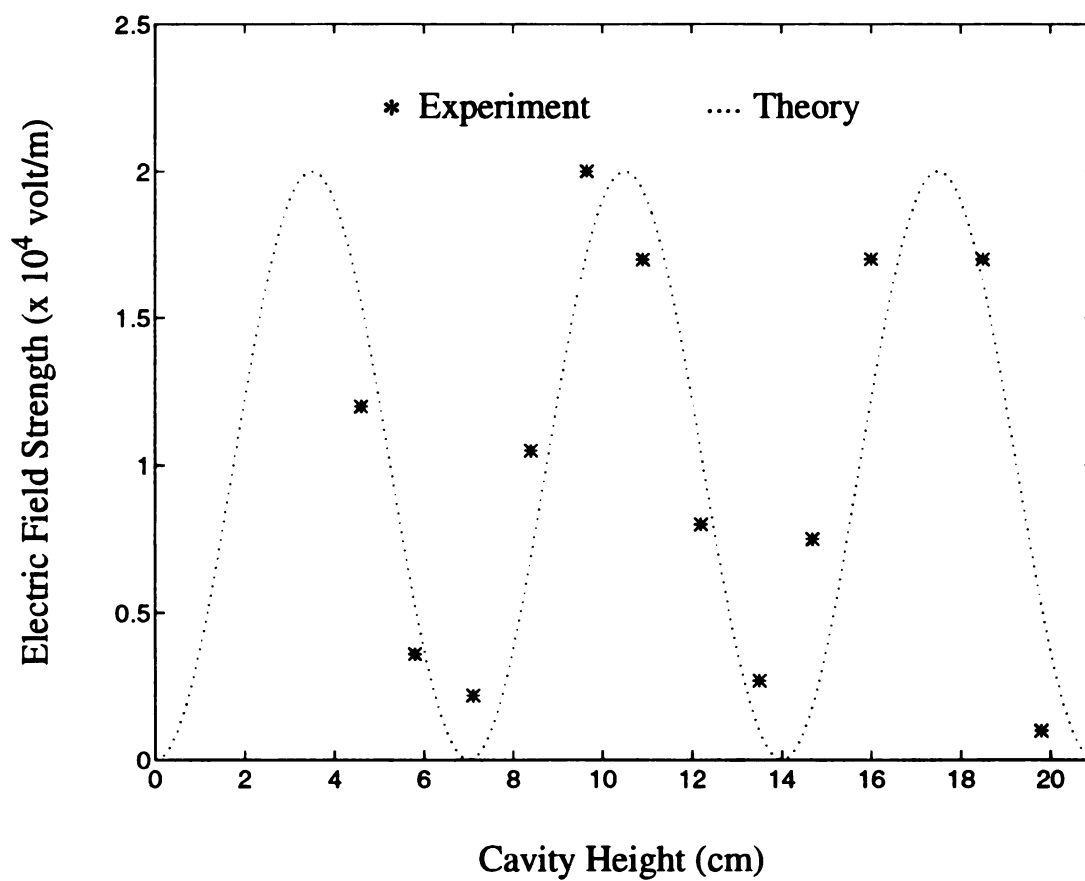


Figure 6-3: Electric field strength vs. cavity height for microwave cavity plasma reactor during diamond deposition process.

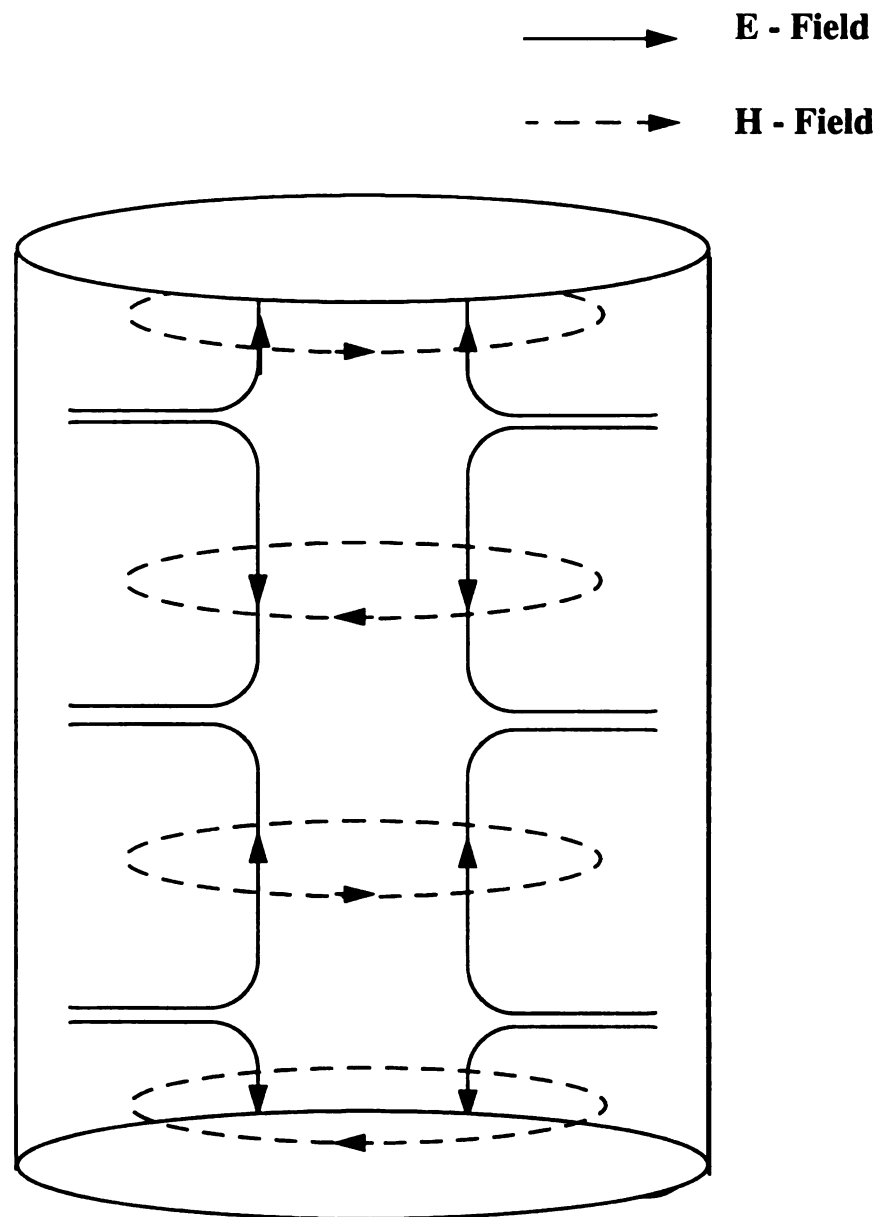


Figure 6-4: Field patterns for TM_{013} mode.

$$U = 2U_e = \epsilon \int |E|^2 dV = \epsilon \int |E_r|^2 dV + \epsilon \int |E_z|^2 dV \quad (6.23)$$

and the Q factor is given by,

$$Q = \frac{\omega U}{P_a} \quad (6.24)$$

where P_a is the power absorbed with the plasma discharge present.

6.4 Implementation for H₂ discharge simulation

The simulation structure for the FDTD model and the plasma fluid model are shown in Figure 6-5. The simulation structure for the FDTD model is basically the same as that discussed in Chapter 5, but the quartz tube which is used to adjust the height of the substrate holder is included in this chapter. The assignments of the perfect conductor boundary condition and non-reflecting boundary condition are the same as in Chapter 5. The location of substrate holder is again assumed as aligned with the upper surface of the base plate. The boundaries of the fluid plasma simulation are the quartz disk and the substrate holder, where the diameter of the substrate holder is the same as that of the quartz disk. The boundary conditions of the fluid plasma model are:

$$\text{at } r = 0: \quad \frac{\partial n_e}{\partial r} = \frac{\partial n_i}{\partial r} = \frac{\partial \Psi}{\partial r} = \frac{\partial T_e}{\partial r} = 0 \quad (6.25)$$

and

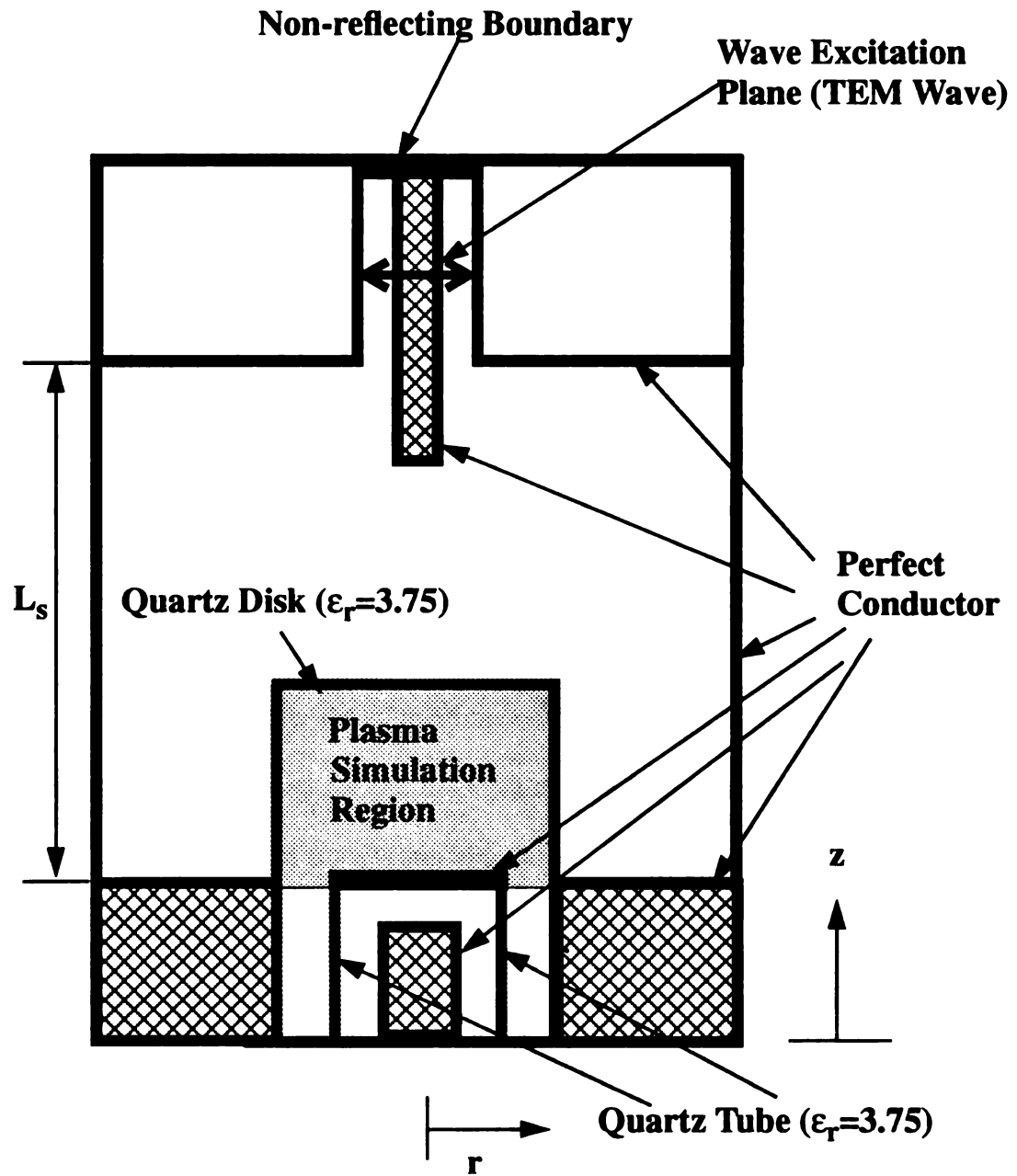


Figure 6-5: Simulation structure cross-section for microwave cavity plasma reactor with quartz tube.

$$\begin{aligned} \text{at the quartz wall and substrate: } n_e &= n_i = \Psi = 0 \\ T_e &= T_n \end{aligned} \quad (6.26)$$

At $r = 0$, which is the center of the cylindrical reactor, the boundary condition (6.25) is based on assuming all the unsolved quantities (n_e , n_i , T_e , and Ψ) have an r symmetry when r approaches to zero. The boundary conditions (6.26) at the quartz wall and substrate assume wall recombination occurs when electrons and ions reach the walls and assume that thermal equilibrium occurs at the walls. The potential is assumed zero on the substrate and on the quartz walls. This assumption is good for the conducting substrate. However on the insulating walls a floating potential is more appropriate. It was observed, though, that the plasma is confined mostly to the region just above the substrate with only weak interaction with the quartz disk walls. Hence, the selection of the quartz boundary condition of $\Psi = 0$ did not alter the simulation results significantly.

The grid structure used for the fluid plasma model is shown in Figure 6-6. The total number of grids used in the plasma simulation is 11 x 11 in the r and z direction respectively. In the z direction, a uniform grid spacing of 0.57 cm is used. In the r direction, the grids are constructed in such a way that all the unit cell areas (or volumes, $\Delta z r \Delta r 2\pi$) are equal. Therefore, the largest grid spacing in the r direction is 2.22 cm, and the smallest is 0.36 cm. Since the grid structure and grid space for the FDTD model are different from those of the fluid plasma model, a linear interpolation technique was used to interpolate the absorbed power to each grid point of the plasma model, and the plasma density and electron temperature to each grid point of the FDTD model.

For the partially ionized and partially dissociated H_2 plasma discharge simulation developed in this study, the major particle interaction processes are the electron- H_2 gas

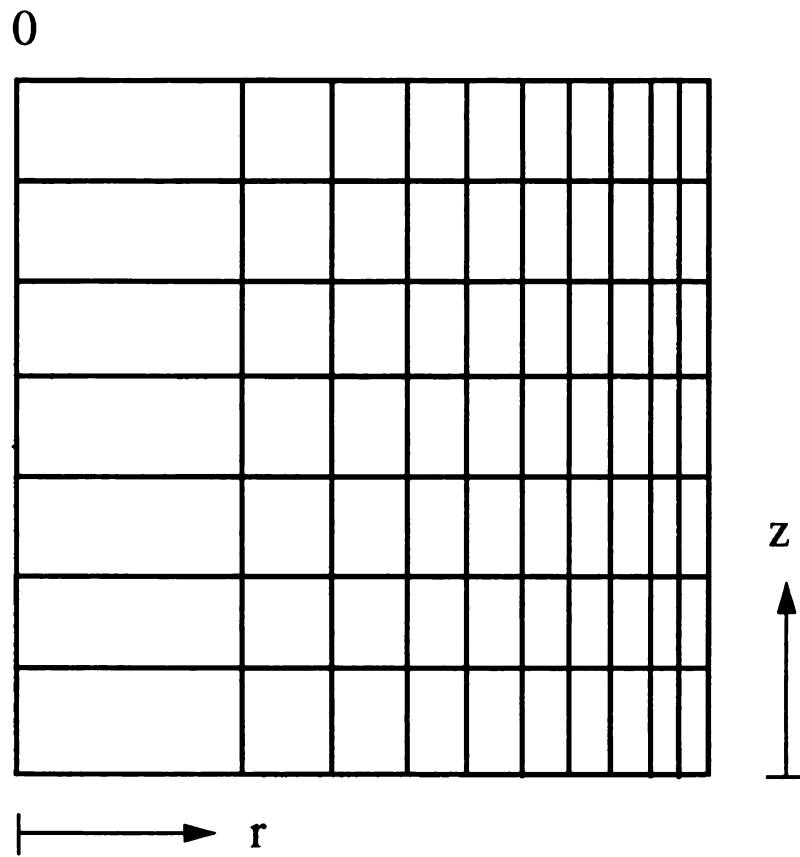


Figure 6-6: Grid structure for fluid plasma model.

inelastic collisions, electron-H₂ gas elastic collision and electron-hydrogen ion recombination. The electron-H₂ inelastic collisions include the H₂ gas ionization, excitation and dissociation processes. The rate coefficient for these collision processes are expressed using the Arrhenius relationship [51] as

$$\begin{aligned} k_{ion} &= A_{ion} \exp(-\epsilon_{ion}/K_B T_e) \\ k_{ext} &= A_{ext} \exp(-\epsilon_{ext}/K_B T_e) \\ k_{dis} &= A_{dis} \exp(-\epsilon_{dis}/K_B T_e) \end{aligned} \quad (6.27)$$

where k_{ion} , k_{ext} and k_{dis} are the collision rate coefficient with unit of m³/sec introduced in Chapter 3; ϵ_{ion} , ϵ_{ext} and ϵ_{dis} are the threshold energy for H₂ gas ionization, excitation and dissociation; and A_{ion} , A_{ext} and A_{dis} are the pre-exponential factors which are obtained by approximating the rate constant data at low T_e in Janev et al.[57] to these relationships. For simplicity, only the reactions with higher rate coefficients are considered in this study for H₂ gas. The types of inelastic collisions and their corresponding rate parameters are summarized in Table 1. The collision frequency for electron-H₂ gas momentum transfer ν_{en} is relatively independent of the electron temperature, so it can be written as [50]

$$\nu_{en}(H_2) \approx 1.44 \times 10^{12} \times \frac{Pressure(Torr)}{T_n(^{\circ}K)} \quad (6.28)$$

where T_n is the neutral temperature which can be represented by the translational temperature of H₂ gas. Since ν_{en} is relatively independent of the electron temperature, the effective collision frequency ν_{eff} is set equal to ν_{en} . It should be noted that the only neutral species considered in the ion and electron simulations was the H₂ species. Hence these simulations assume a low hydrogen dissociation percentage.

Table 1: H₂ Reaction Rates

Reaction	Expression	Threshold energy	pre-exponential factor or rate coefficient (m ³ /sec)
Ionization	$e + H_2 \rightarrow e + H_2^+ + e$	15.4 eV	1.0×10^{-14}
Excitation	$e + H_2 \rightarrow H_2^* + e$	12.0 eV	6.5×10^{-15}
Dissociation	$e + H_2 \rightarrow e + H + H$	10.0 eV	1.0×10^{-14}
Recombination	$e + ion \rightarrow neutral$	0 eV	1.0×10^{-14}

6.5 Simulation results for fluid plasma model

The simulation results for the microwave cavity plasma reactor loaded with a H_2 discharge are present in this section. Before coupling the FDTD electromagnetic model with the fluid plasma model to get self-consistent power absorption solutions, the validity and stability of the fluid plasma model will be examined first by providing a constant absorbed power, 500 Watt, as input data. The neutral temperature profile is assumed neutral as 2000 °K at the discharge center and 1000 °K at the quartz disk boundary. The 2000 °K neutral temperature and the volume of this 2000 °K region was selected based on experimental measurements of the hydrogen translational temperature and the plasma volume [54] as shown in Figure 6-7(d). Assuming the pressure is 50 Torr and the input absorbed power is 500 Watt, the electron density, ion density, and electron temperature are determined by solving the Poisson equation, the electron/ion continuity equations, and the electron energy balance equation. The results are shown in Figure 6-7. Part (a) and part (b) are the electron density and plasma potential. The electron density is higher at the center and drops gradually toward the boundary to match the boundary condition ($n_e = n_i = 0$). The plasma potential is quite uniform due to the quasi-neutral condition in the bulk plasma region. Part (c) shows the electron temperature profile. Basically, it is uniform over the discharge region. The stability of the numerical solution of the fluid plasma model is shown in Figure 6-8. The electron temperature, which is very sensitive to the plasma density oscillates severely during the beginning iterations since the electron energy equation and the continuity equations are loosely coupled. By using a damping factor equal to 10^{-5} for electron temperature during the beginning iterations, the electron temperature converges to a stable value after about 30 iterations.

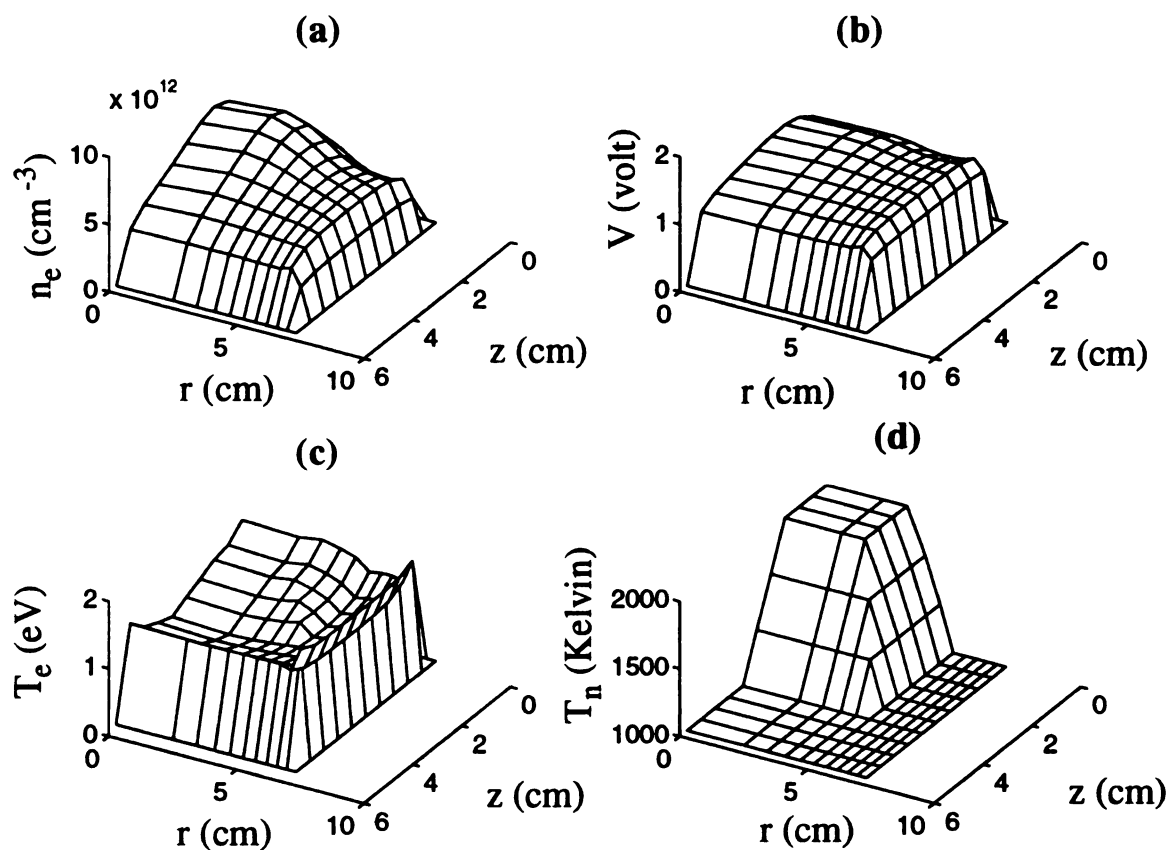


Figure 6-7: Simulation results of microwave cavity plasma reactor using fluid plasma model with uniform absorbed power density. (a) Electron density (b) Plasma potential (c) Electron temperature (d) Neutral temperature (assigned values).

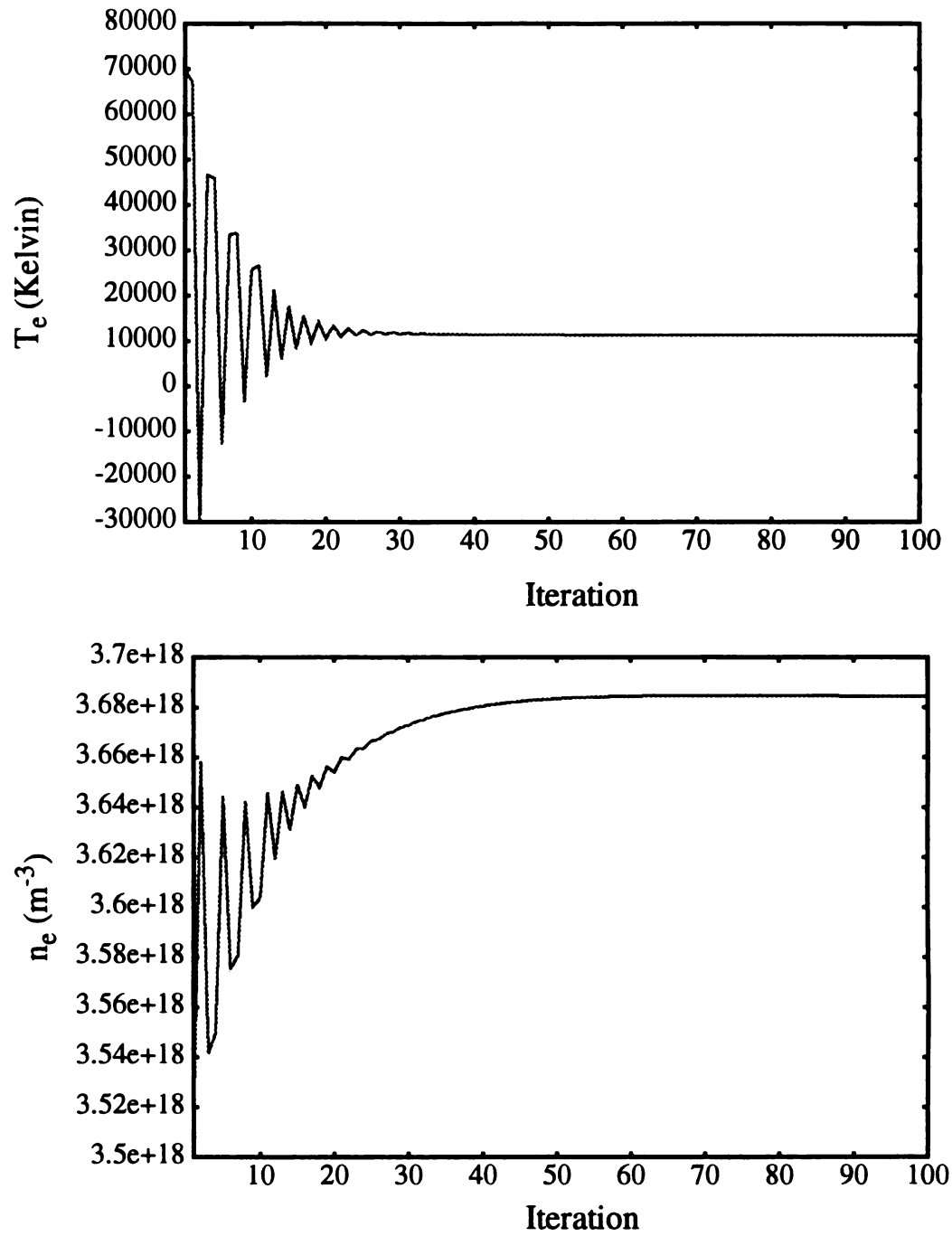


Figure 6-8: Electron temperature and density variations during fluid plasma simulation.

This example shows the application of the fluid model for microwave discharge simulation with a constant, uniform absorbed microwave power input. The resulting data of this simulation can be used as the initial conditions (shown in Figure 6-1) for the self-consistent microwave cavity plasma reactor simulation.

6.6 Self-Consistent results for microwave cavity plasma reactor simulation

The microwave cavity plasma reactor loaded with H₂ gas for diamond film deposition is simulated and investigated by a self-consistent numerical model which has been described in the previous sections. The input parameters for this model includes the pressure and input microwave power. A set of empirical equations developed by G. King [58] are used to establish the neutral temperature profile for this simulation. These empirical equations are based on the statistically-designed experimental data obtained by discharge diagnostics in a parameter space including pressure and input microwave power. The empirical equations used to predict the translational temperature of H₂ gas and the discharge volume are [58]:

$$\begin{aligned} \text{Translational Temperature } (^{\circ}\text{K}) = & 228.6 + 374.3 \times \text{Incident Power (kW)} + 16.5 \times \\ & \text{Pressure (Torr)} \pm 94.2 \end{aligned} \quad (6.29)$$

$$\begin{aligned} \text{Plasma Volume (cm}^3\text{)} = & 449.7 + 116.2 \times \text{Incident Power (kW)} - 18.1 \times \text{Pressure} \\ & \text{(Torr)} + 57.1 \times [\text{Incident Power (kW)}]^2 + 0.25 \times [\text{Pressure (Torr)}]^2 - 5.4 \times \text{Pres-} \\ & \text{sure (Torr)} \times \text{Incident Power (kW)} \pm 15.4 \end{aligned} \quad (6.30)$$

The plasma volume serves as a boundary for neutral temperature (T_n). Inside the plasma

volume region, the translational temperature given by (6.29) is the neutral temperature. Outside the volume, the neutral temperature is equal to the temperature assigned on boundaries ($T_n = 1000$ °K). Between these two regions, a linear temperature change profile is used to prevent an abrupt change of T_n . This is done by assigning the boundary temperature ($T_n = 1000$ °K) to the region several grids, namely three grids, away from the plasma volume in both the r and z directions. The temperature assigned on the grids between these two region are linearly interpolated from the neutral temperature given by (6.29) and boundary temperature ($T_n = 1000$ °K).

The simulation results for the electric field distribution are shown in Figure 6-9 and Figure 6-10 for E_r and E_z field components respectively. The input condition for this simulation is 50 Torr in pressure and 1500 Watts input microwave power. The electric field patterns basically follow the TM_{013} mode electric fields distribution. The affect of the electric field caused by the presence of discharge can be observed. It reduces the amplitude of the electric field in the plasma discharge region since electromagnetic power is absorbed in the discharge region. The discontinuity of the electric field resulting from the difference of dielectric constant between the quartz and air can also be seen. The conductivity of the plasma can be determined from (3.42) using the solved density and effective collision frequency. Figure 6-11 shows the maximum conductivity of the discharge is around 0.4 mho-m. Figure 6-12 shows the power absorption pattern and indicates that the most microwave power is absorbed in the center region and closed to the substrate. The electric field patterns inside the quartz disk (plasma simulation region) are shown in Figure 6-13 and Figure 6-14. It can be observed that the E_z field doesn't just decay into the discharge but also is concentrated in the region above the substrate. This is

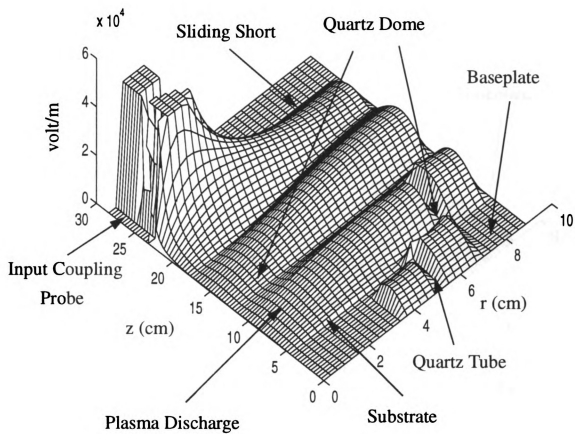


Figure 6-9: E_r field distribution.

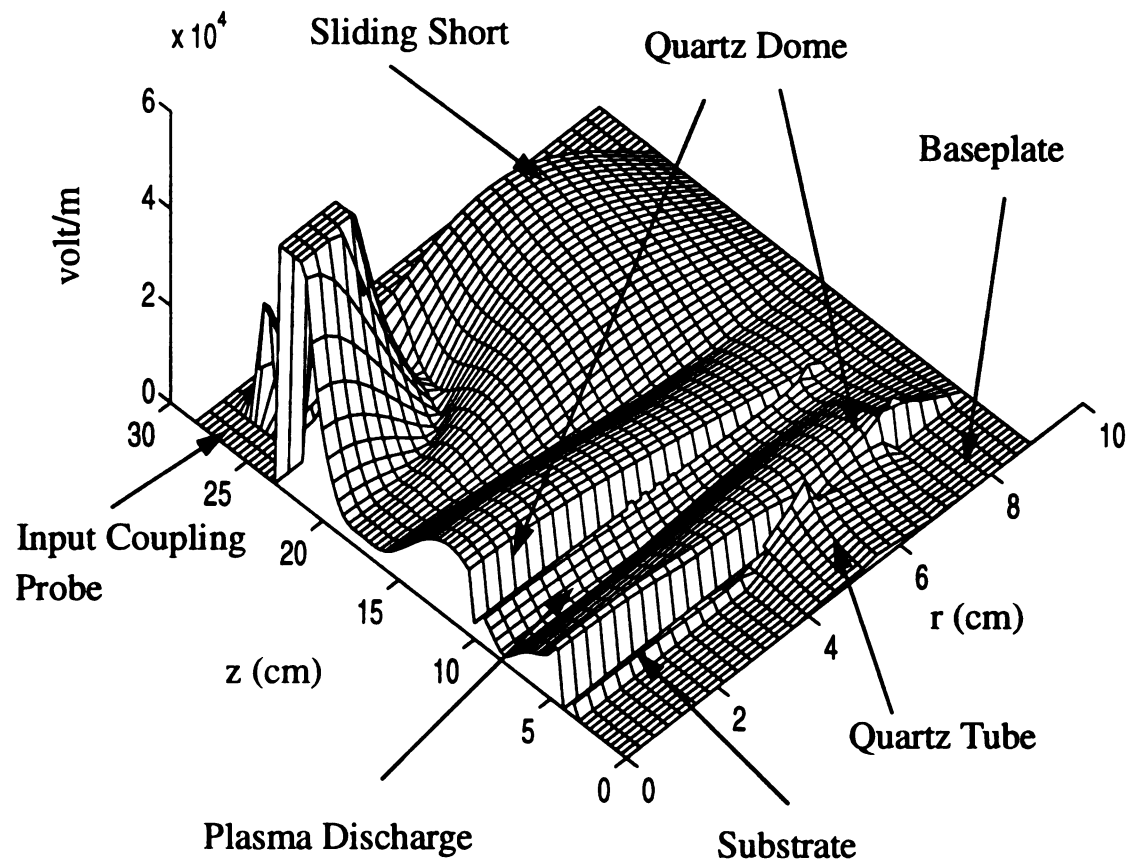


Figure 6-10: E_z field distribution.

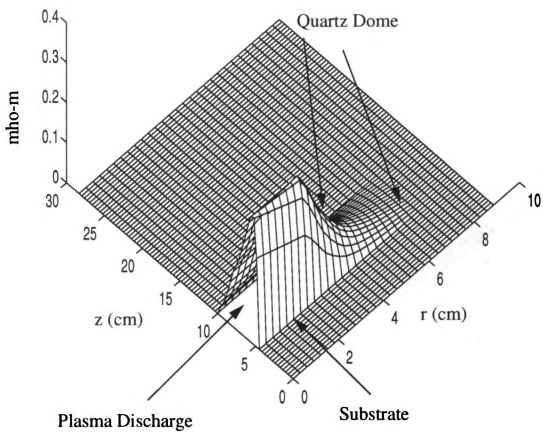


Figure 6-11: Conductivity distribution.

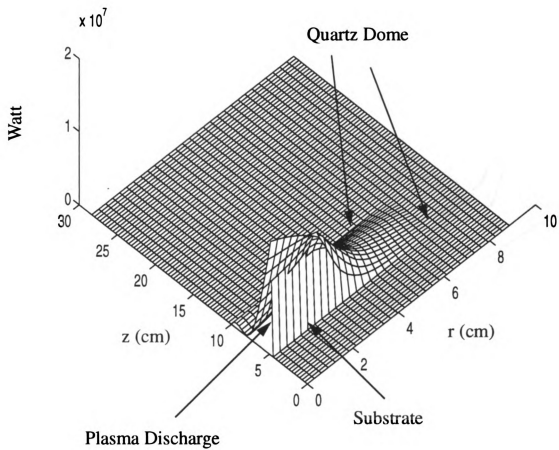


Figure 6-12: Absorbed power patterns.

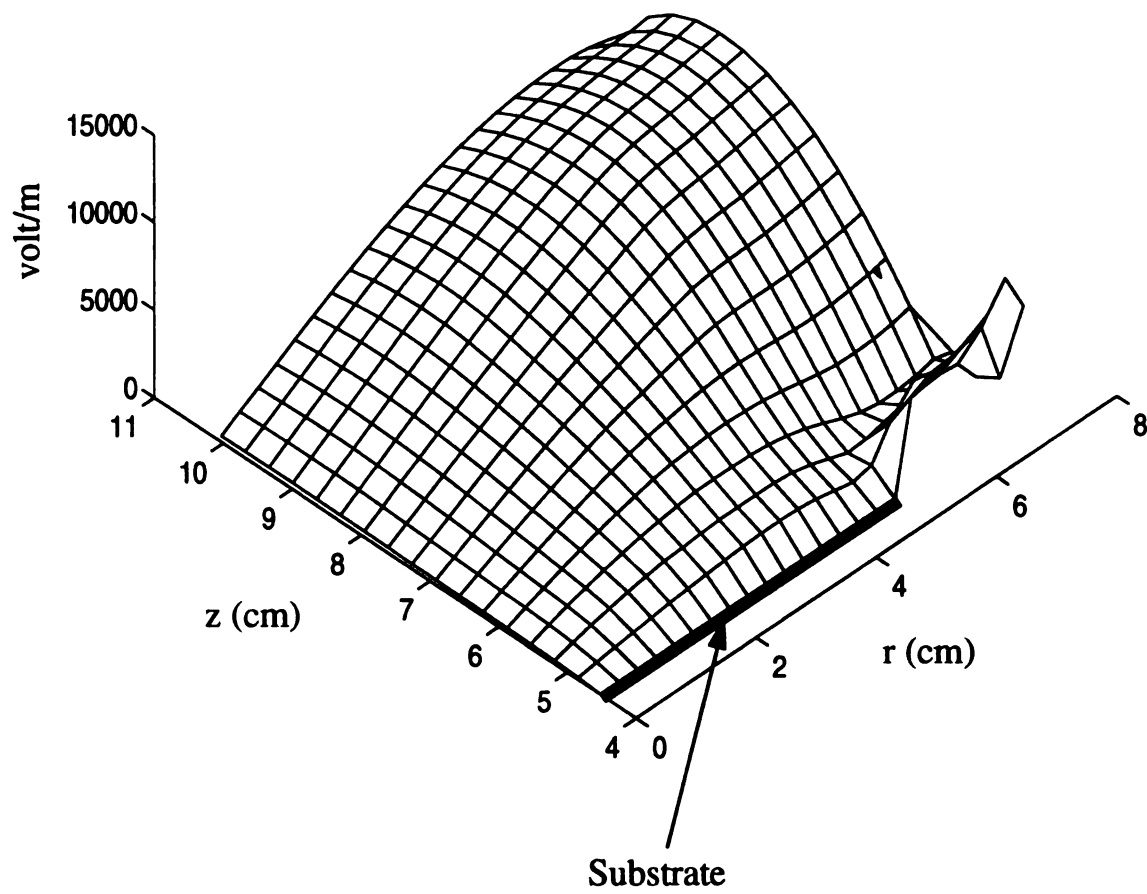


Figure 6-13: E_r field pattern inside the quartz disk region.

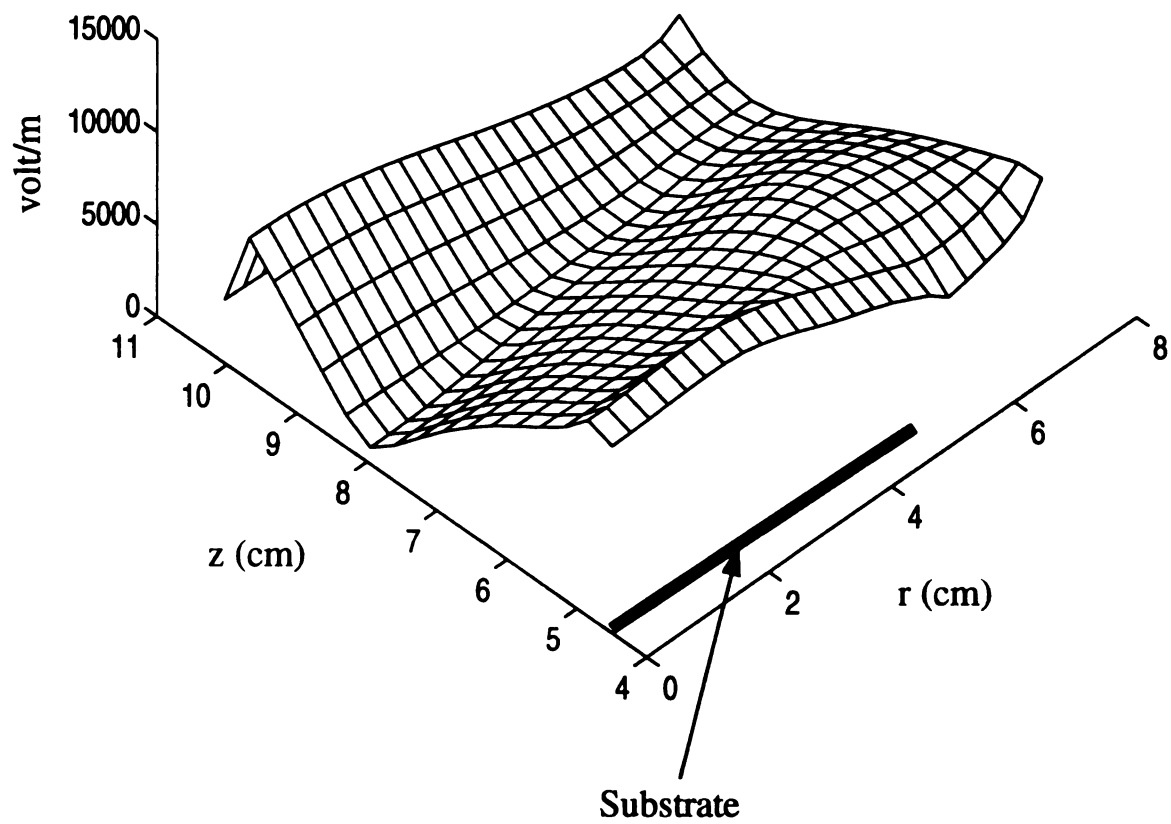


Figure 6-14: E_z field pattern inside the quartz disk region.

because the discharge has a finite size and the plasma density is not uniform. Therefore, the electric field might propagate into the quartz disk region from other directions and concentrate at the region above the substrate without being blocked by the discharge.

The simulation result of the characteristics of a H_2 discharges at 50 Torr and 1500 Watts input power is shown in Figure 6-15. The neutral temperature profile determined by the empirical equations is shown at part (d). The plasma density is concentrated more at the center. The electron temperature is also highest at the center of the discharge. The spatial variation of ionization and recombination rate are shown in Figure 6-16. The ionization rate is higher near the substrate due to the electron temperature being higher at that region. The recombination rate profile basically follows the electron density variation. Figure 6-17 shows spatial variations of various energy loss mechanism of electrons, including ionization, excitation, dissociation, recombination, and elastic collisions. It shows the energy loss due to elastic collision is the major energy loss for electrons in H_2 discharge under moderate pressure. The convergence behavior of the absorbed power is shown in Figure 6-18. When the power absorbed by the plasma converges to a stable value, the steady state solution of this numerical model has been obtained.

The characteristics of H_2 discharges and cavity quality factor Q are analyzed for various pressure and absorbed power by this numerical model. The neutral temperature and plasma volume determined by (6.29) and (6.30) are the input data for simulations and their variations for different incident power and pressure are shown Figure 6-19. The simulation results of average electron temperature vs. absorbed microwave power are shown in Figure 6-20. These average values are calculated by integrating the temperature inside the plasma volume and divided by the plasma volume. The average electron

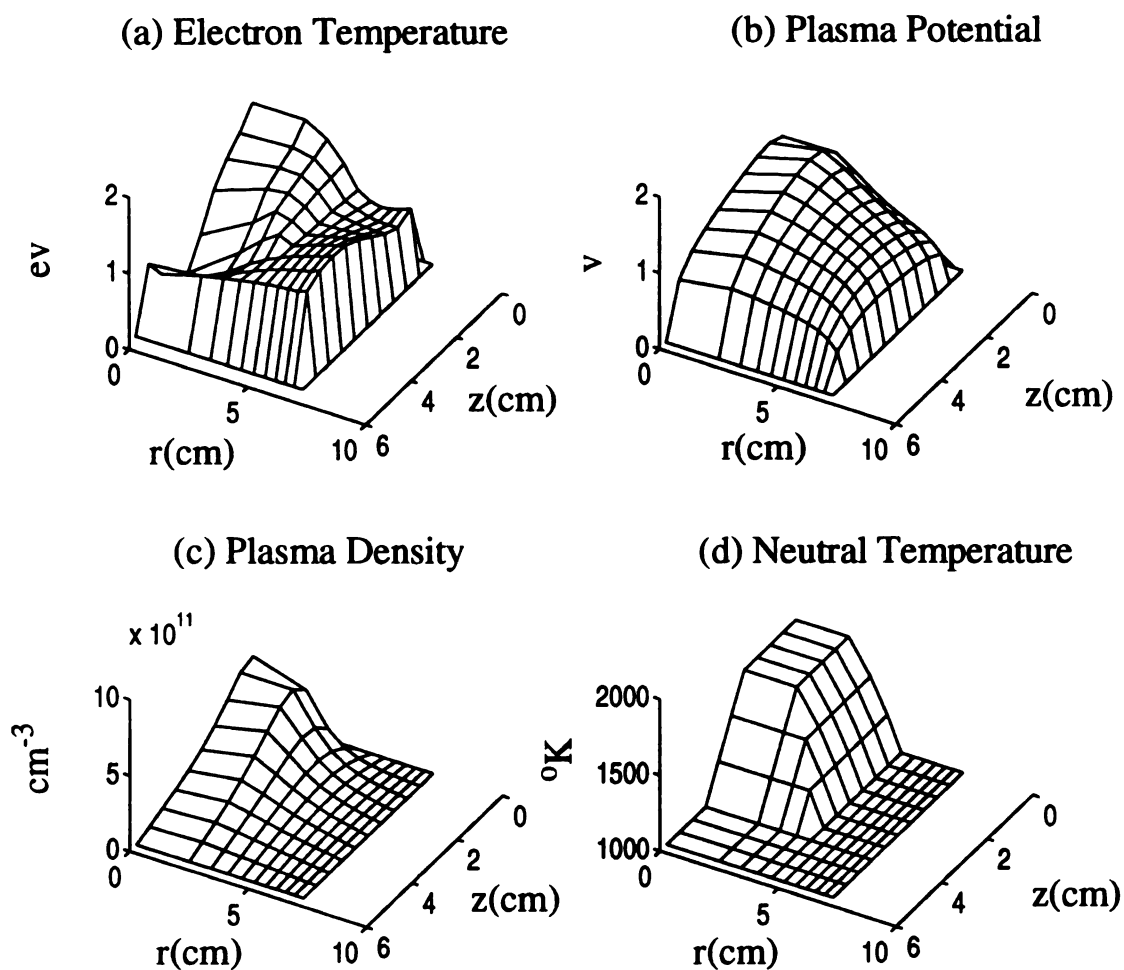


Figure 6-15: Simulation results of a microwave cavity plasma reactor for pressure = 50 Torr and input microwave power = 1500 watt. (a) Electron density (b) Plasma potential (c) Electron temperature (d) Neutral temperature (assigned values).

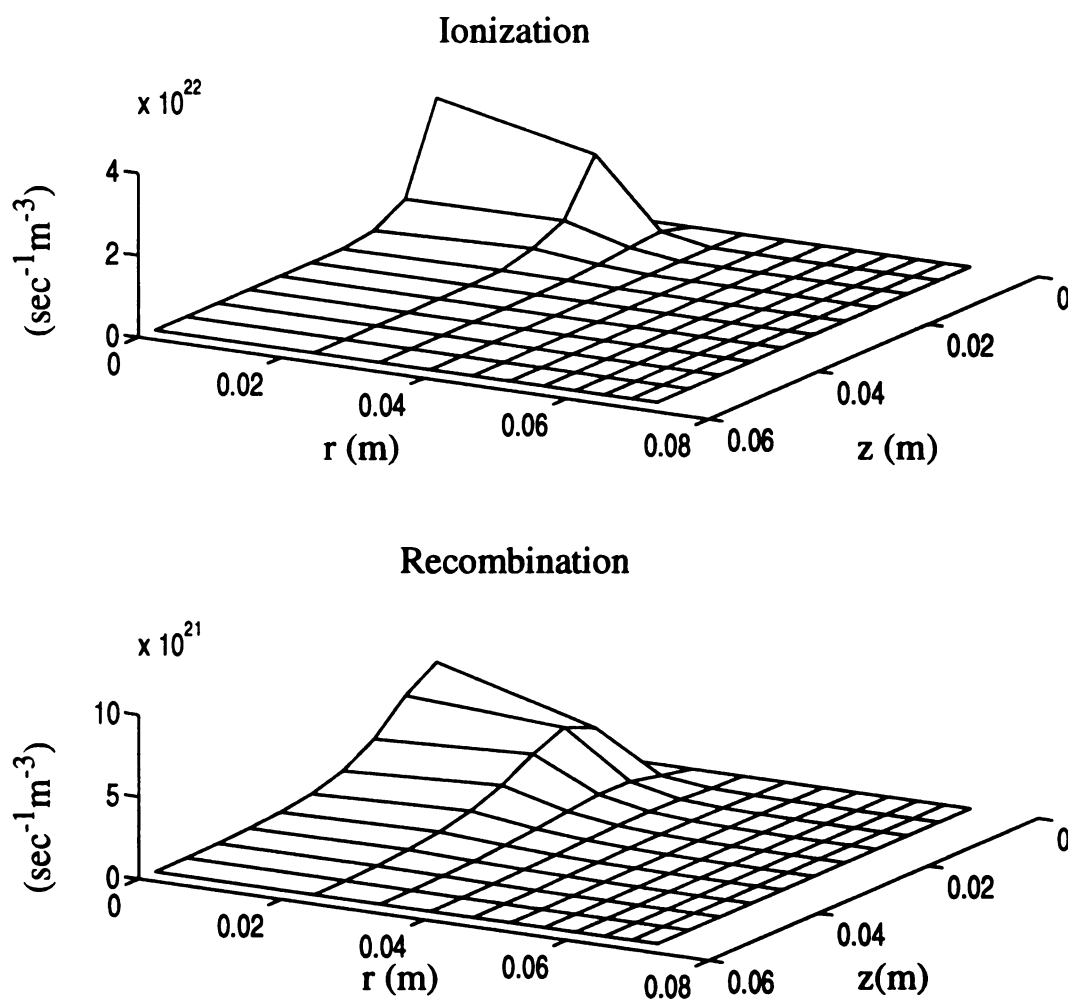


Figure 6-16: Spatial variation of ionization rate and recombination rate for pressure = 50 Torr and input microwave power = 1500 watt.

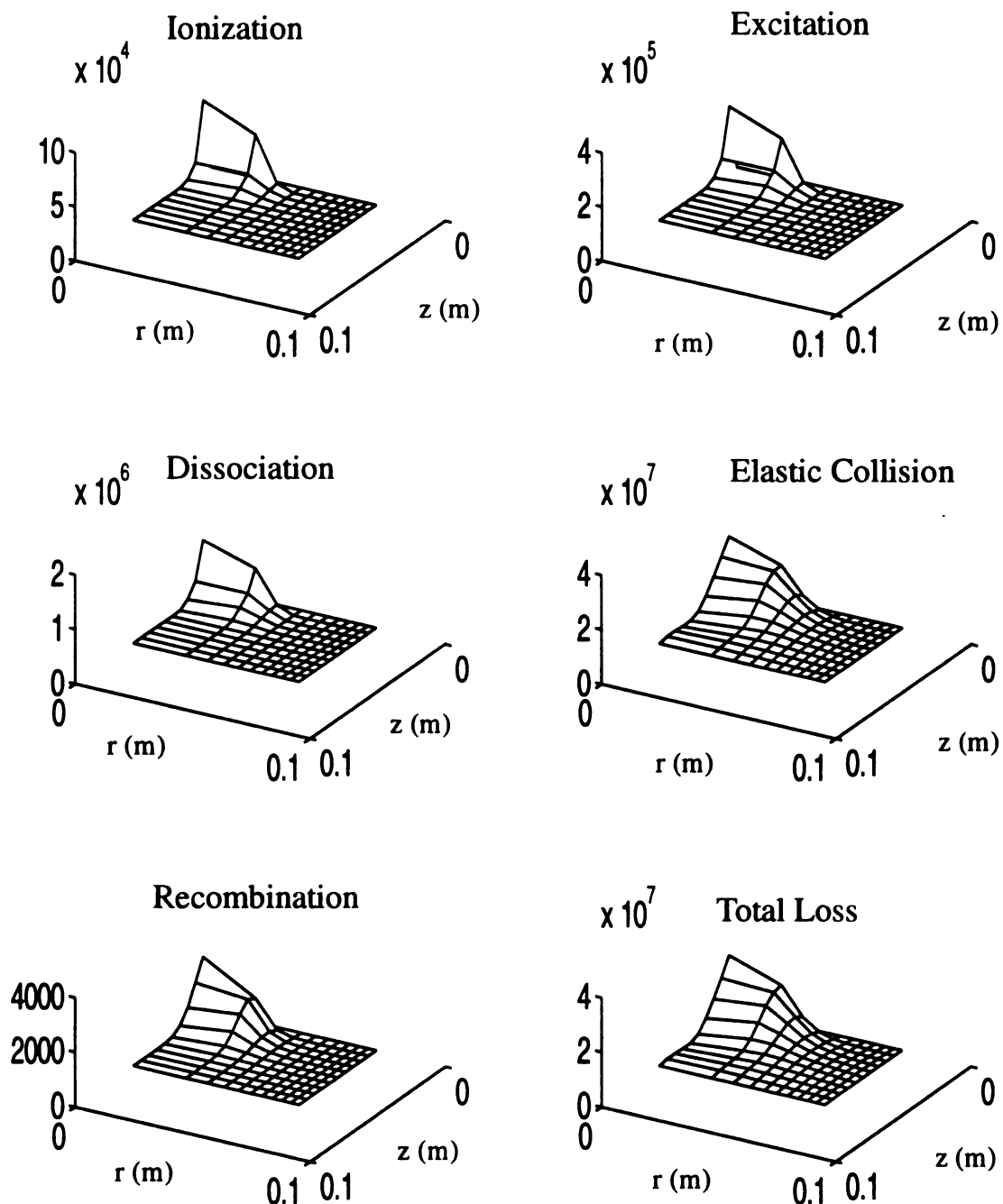


Figure 6-17: Spatial distribution of various energy loss for pressure = 50 Torr and input microwave power = 1500 watt. The unit of the energy loss is Watt/m^3 .

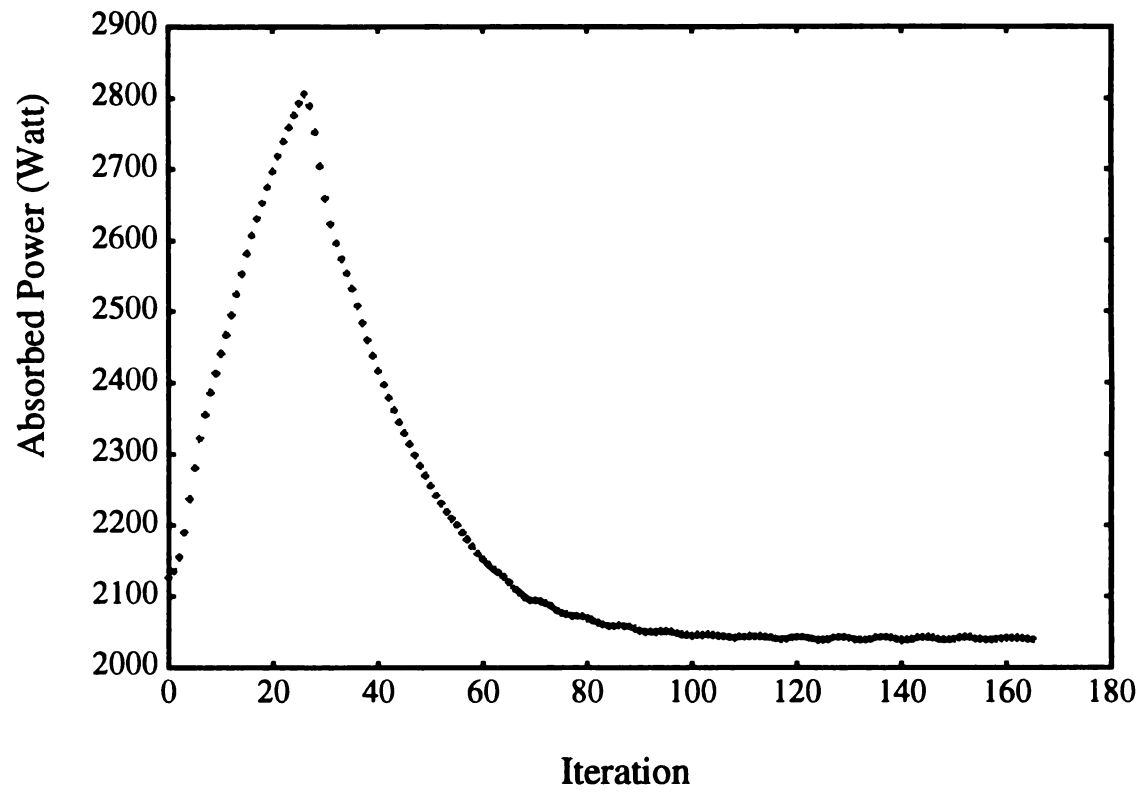


Figure 6-18: Absorbed power vs. number of iterations.

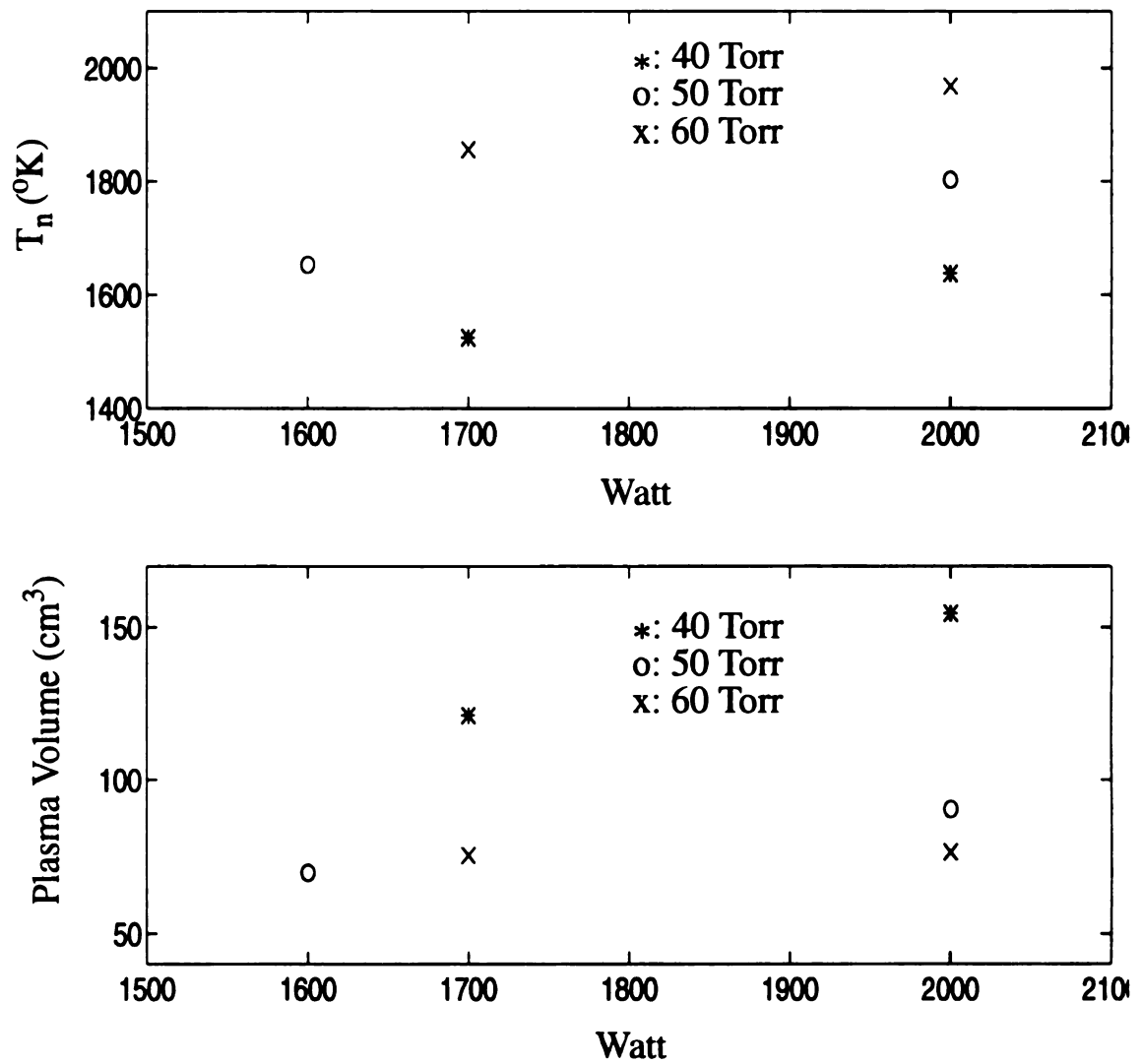


Figure 6-19: Neutral temperature and plasma volume vs. incident power for various pressures.

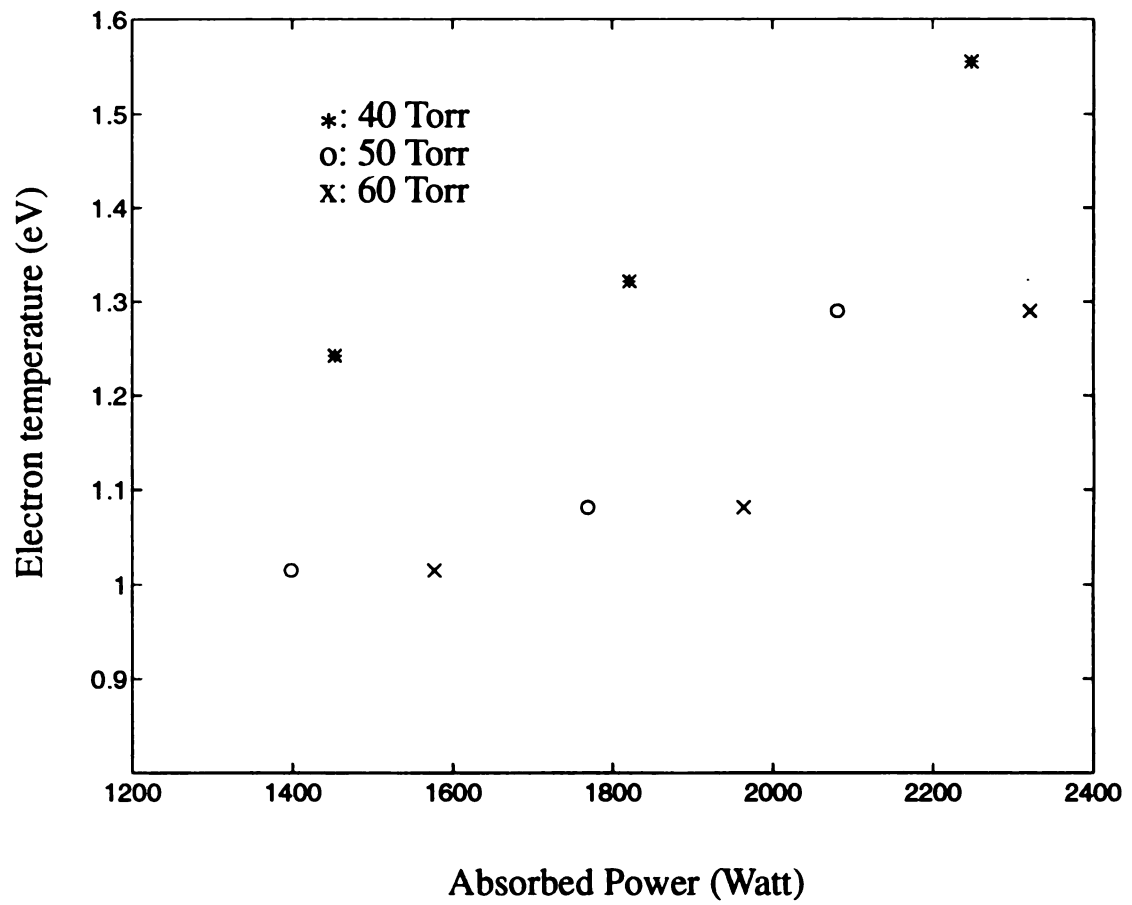


Figure 6-20: Electron temperature vs. absorbed power for three different pressures.

temperature is about 1.5 eV. The electron temperature increase with higher absorbed microwave power. Also, the electron temperature drops with increases of pressure. This can be understood since higher pressure means higher collision frequency for electron with neutrals. Therefore, electrons more easily transfer their energy to neutral particles and reduce their kinetic energy. The results for Q vs. absorbed microwave power are shown in Figure 6-21 respectively. It shows when the more power absorbed by the discharge the lower the Q factor. The pressure has only a little effect on the Q factor. At the 50 Torr pressure and 1500 microwave power condition, the Q factor of the microwave cavity plasma reactor with a H_2 discharge has been experimental determined by using the technique developed earlier Section 6.3. The Q value determined experimentally is about 100 which is close to the simulation result ($Q = 107$). This close agreement is an additional indication of the validity of the model.

6.7 Summary

The self-consistent simulation results for a microwave cavity plasma reactor were given in this chapter by coupling the FDTD model and the fluid plasma model developed in previous chapters. The electric field patterns and power absorption patterns in a TM_{013} mode microwave cavity plasma reactor operating with a hydrogen discharge were simulated. The simulated electric field distributions showed a good agreement with the results of electric field measurements done using a micro-coax probe technique. The characteristics of the H_2 plasma were also investigated and analyzed for various microwave powers and pressures. The quality factor Q for the discharge loaded cavity was determined by numerical simulation and by experimental measurement. The two results

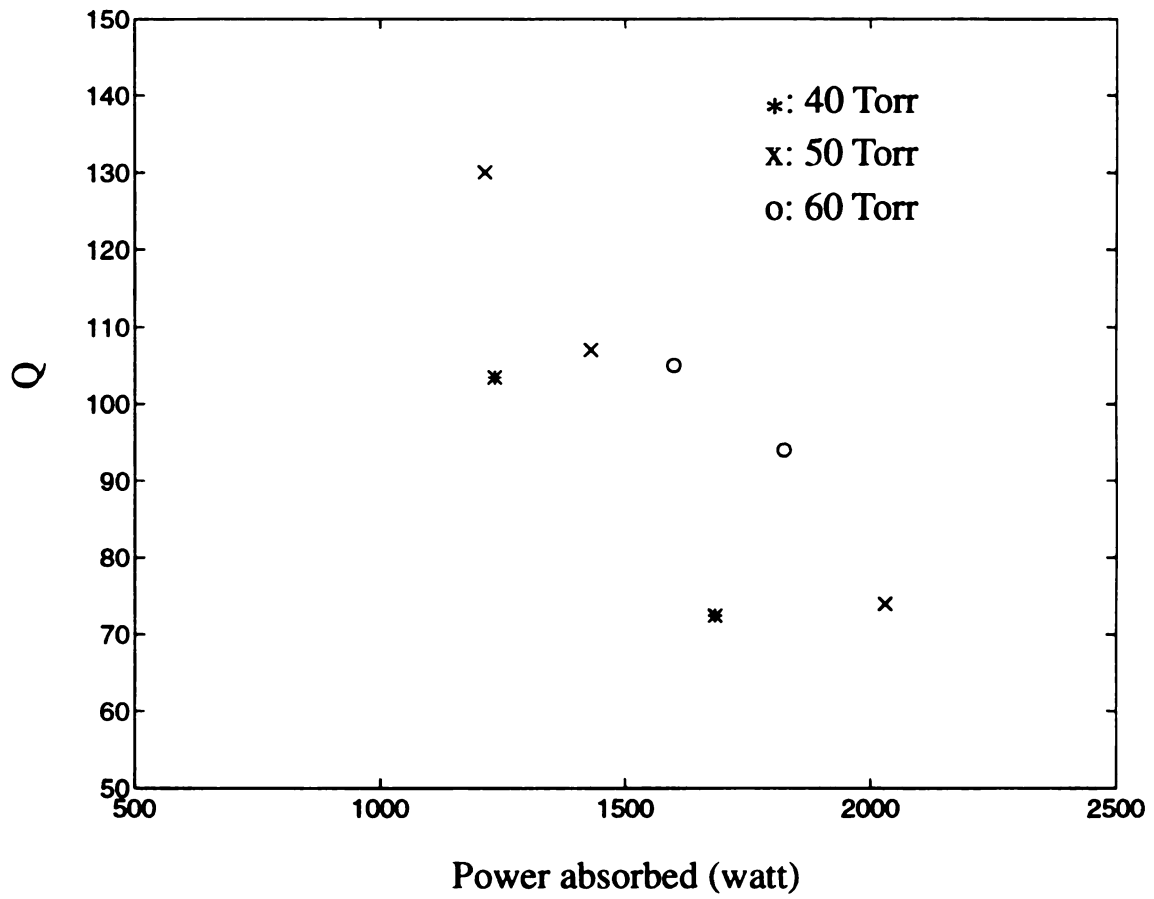


Figure 6-21: Q value vs. absorbed power for three different pressures.

showed good agreement which serves as a verification of the accuracy of the numerical model developed in this study.

Chapter 7

Conclusions

A self-consistent numerical model has been developed to simulate the electromagnetic excitation of discharges inside microwave cavity plasma reactors. This software includes a electromagnetic field model and a fluid plasma model. The microwave cavity plasma reactors simulated by this numerical software were loaded with a H₂ discharge and used for diamond thin film deposition. The complex reactor geometry and input power coupling probe structure were included in the simulation. The input parameters for the microwave cavity plasma reactor simulation included the pressure and input microwave power. The operating pressure investigated in this study was the moderate pressure range (1 Torr to 100 Torr). The input microwave power was from several hundred watts to several kilowatts. The electromagnetic behavior of the discharge loaded resonant cavity, such as the electric field distributions, power absorption patterns, and cavity quality factor Q, were studied and analyzed for various input condition. The characteristics of H₂ discharges, including the plasma density, electron temperature, and plasma potential, were also investigated and studied. The electromagnetic mode and cavity Q value of a H₂ discharge loaded reactor were simulated and shown to be in agreement with measured experimental values.

The electromagnetic field model developed in this research is based on using the finite-difference time-domain (FDTD) numerical method to solve the time-dependent Maxwell's equations. The major advantage of this method is that it can be easily implemented to solve the field in complex geometry structures with complex loaded materials, such as plasmas. In order to investigate the microwave power absorbed by the lossy materials or discharges, appropriate conductivity models were identified and used to solve the microwave field induced current density. For plasma discharges, this induced current density was determined by solving the electron momentum transport equation.

Chapter 4 presented the transient simulation results of microwave resonant cavities using the three-dimensional FDTD simulation method for empty and loaded cylindrical cavities. Comparisons to exact analytical models using simple geometry cavities were used to verify the accuracy of the electromagnetic field model. The results of empty cavity simulations agreed well with the theoretical resonant mode. The simulated natural frequency of a lossy loaded cavity also match the analytical solutions. A compact ECR ion source and a Ar loaded cavity were also simulated by using a magnetized discharge conductivity model for the ECR source and by simultaneously solving the electron momentum transport equation in the time domain, respectively. The steady state simulation method was introduced by including the input power coupling structure into the electromagnetic model as shown in Chapter 5. By implementing a non-reflecting boundary condition, the open boundary problem at the end of the input coupling probe was solved. The Q value and the power reflected from the microwave cavity plasma reactor were analyzed for various cavity height and loaded conductivity. This simulated reflected power characteristic behavior is similar to that found in experimental systems.

A fluid plasma model was developed in Chapter 3. It solved the electron and ion continuity equations, the electron energy balance equation, and the Poisson equation. The input to this plasma model was the microwave power density absorbed by the discharge, which was calculated by the electromagnetic field model. The discharge characteristics simulated by the plasma model were feedback to the electromagnetic field model to update the electromagnetic field and power absorption. The final self-consistent results were solved iteratively to a converging solution by these two models. This self-consistent solution was done using two dimensional solution of the FDTD and fluid plasma models.

The electromagnetic field solution technique present in this study allows the calculation of the power absorption profile in microwave discharges which has often been a difficulty in plasma simulations. The understanding obtained from the electromagnetic solution allows the reactor design structure to be analyzed for improvement and optimization of such quantities as uniformity of microwave power absorption. Additionally, the simulation and understanding of the electromagnetic fields is expected to be key to microwave reactor control.

The techniques developed in this study could in the future be applied to a wide range of plasma sources including the various high density sources, e.g. inductively coupled sources, helicon source and ECR sources. Other future work extending this study includes self-consistently solving the temperatures and densities of various neutral species, expanding the two dimensional fluid plasma model to three dimensions, and developing a numerical model to simulate the side-feed input coupling structure for TE_{n11} mode cavities.

APPENDIX

APPENDIX

The derivation of discretized Poisson equation (3.37) is provided here in details.

The Poisson equation can be written as

$$\nabla \bullet \mathbf{E} = \frac{\rho}{\epsilon}. \quad (\text{A.1})$$

In 2-D cylindrical coordinates, it can be expanded to

$$\frac{\partial}{\partial r}(rE_r) + r\frac{\partial E_z}{\partial z} = r\frac{\rho}{\epsilon}. \quad (\text{A.2})$$

Integrating from $r_{i-1/2}$ to $r_{i+1/2}$ and $z_{k-1/2}$ to $z_{k+1/2}$, (A.1) becomes

$$\begin{aligned} & r_{i+1/2}E_r\left(i+\frac{1}{2}, k\right) \cdot (z_{k+1/2}-z_{k-1/2}) - r_{i-1/2}E_r\left(i-\frac{1}{2}, k\right) \cdot (z_{k+1/2}-z_{k-1/2}) \\ & + \left(\frac{r_{i+1/2}^2 + r_{i-1/2}^2}{2}\right) \left(E_z\left(i, k+\frac{1}{2}\right) - E_z\left(i, k-\frac{1}{2}\right)\right) \\ & = \frac{\rho(i, k)}{\epsilon} \left(\frac{r_{i+1/2}^2 + r_{i-1/2}^2}{2}\right) (z_{k+1/2} - z_{k-1/2}) \end{aligned} \quad (\text{A.3})$$

Since

$$z_{k+1/2} - z_{k-1/2} = \frac{\Delta z_k + \Delta z_{k-1}}{2}, \quad (\text{A.4})$$

for uniform grid spacing in the z direction and

$$\rho(i, k) = e(n_i(i, k) - n_e(i, k)), \quad (\text{A.5})$$

(A.3) can be rewritten as

$$\begin{aligned} & \left(\frac{2}{r_{i+1/2}^2 - r_{i-1/2}^2} \right) \cdot \left(r_{i+1/2} E_r\left(i + \frac{1}{2}, k\right) - r_{i-1/2} E_r\left(i - \frac{1}{2}, k\right) \right) \\ & + \frac{2}{(\Delta z_k + \Delta z_{k-1})} \cdot \left(E_z\left(i, k + \frac{1}{2}\right) - E_z\left(i, k - \frac{1}{2}\right) \right) \\ & = \frac{e}{\epsilon} (n_i(i, k) - n_e(i, k)) \quad . \end{aligned} \quad (\text{A.6})$$

Moreover, using

$$\nabla \Psi = E, \quad (\text{A.7})$$

E_r and E_z are discretized to be

$$E_r\left(i + \frac{1}{2}, k\right) = -\frac{\Psi(i+1, k) - \Psi(i, k)}{\Delta r(i)} \quad (\text{A.8})$$

and

$$E_z\left(i, k + \frac{1}{2}\right) = -\frac{\Psi(i, k+1) - \Psi(i, k)}{\Delta z(k)}. \quad (\text{A.9})$$

Substitute (A.8) and (A.9) into (A.6) the discretized Poisson equation is

$$\begin{aligned}
& \left(\frac{2}{r_{i+1/2}^2 - r_{i-1/2}^2} \right) \cdot \frac{r_{i+1/2}}{\Delta r_i} \cdot \Psi(i+1, k) \\
& + \left(\frac{2}{r_{i+1/2}^2 - r_{i-1/2}^2} \right) \cdot \frac{r_{i-1/2}}{\Delta r_{i-1}} \cdot \Psi(i-1, k) \\
& + \frac{2}{(\Delta z_k + \Delta z_{k-1})} \cdot \frac{\Psi(i, k+1)}{\Delta z_k} \\
& + \frac{2}{(\Delta z_k + \Delta z_{k-1})} \cdot \frac{\Psi(i, k-1)}{\Delta z_{k-1}} \\
& - \left(\left(\frac{2}{r_{i+1/2}^2 - r_{i-1/2}^2} \right) \cdot \left(\frac{r_{i+1/2}}{\Delta r_i} + \frac{r_{i-1/2}}{\Delta r_{i-1}} \right) \right. \\
& \left. + \frac{2}{(\Delta z_k + \Delta z_{k-1})} \cdot \left(\frac{1}{\Delta z_k} + \frac{1}{\Delta z_{k-1}} \right) \right) \cdot \Psi(i, k) \\
& = -\frac{q}{\epsilon} (n_i(i, k) - n_e(i, k)) \quad .
\end{aligned} \tag{A.10}$$

as shown in (3.37). The other discretized equations, such as electron continuity equation (3.38) and electron energy balance equation (3.41), can be derived in a similar manner.

In case of the point $r = 0$ ($i = 1$), then (A.2) is integrated from 0 to $r_{3/2}$ instead of from $r_{i-1/2}$ to $r_{i+1/2}$. With (A.4) and (A.5), (A.6) becomes

$$\begin{aligned}
& r_{3/2} E_r \left(\frac{3}{2}, k \right) + \frac{2}{(\Delta z_k + \Delta z_{k-1})} \cdot \left(E_z \left(1, k + \frac{1}{2} \right) - E_z \left(1, k - \frac{1}{2} \right) \right) \\
& = \frac{e}{\epsilon} (n_i(1, k) - n_e(1, k))
\end{aligned} \tag{A.11}$$

Then, substituting (A.8) and (A.9) into (A.11), the discretized Poisson equation for $r = 0$ is

$$\begin{aligned}
& \frac{2}{r_{3/2}} \cdot \frac{1}{\Delta r_1} \cdot \Psi(2, k) + \frac{2}{r_{3/2}} \cdot \frac{1}{\Delta r_1} \cdot \Psi(1, k) \\
& + \frac{2}{(\Delta z_k + \Delta z_{k-1})} \cdot \frac{\Psi(1, k+1)}{\Delta z_k} + \frac{2}{(\Delta z_k + \Delta z_{k-1})} \cdot \frac{\Psi(1, k-1)}{\Delta z_{k-1}} \\
& - \frac{2}{(\Delta z_k + \Delta z_{k-1})} \left(\frac{1}{\Delta z_k} + \frac{1}{\Delta z_{k-1}} \right) \cdot \Psi(1, k) \\
& = -\frac{q}{\varepsilon} (n_i(1, k) - n_e(1, k)).
\end{aligned} \tag{A.12}$$

Similarly, the discretized electron continuity equation and electron energy balance equation at $r = 0$ can be derived as

$$\begin{aligned}
& \frac{2}{r_{3/2}} \cdot J_{er} \left(\frac{3}{2}, k \right) + \frac{2}{(\Delta z_k + \Delta z_{k-1})} \cdot \left(J_{ez} \left(1, k + \frac{1}{2} \right) - J_{ez} \left(1, k - \frac{1}{2} \right) \right) \\
& = n_e(i, k) [n_n(1, k) k_{ion}(1, k) - \alpha_r(1, k) n_i(1, k)]
\end{aligned} \tag{A.13}$$

and

$$\begin{aligned}
& \frac{2}{r_{3/2}} \cdot q_{er} \left(\frac{3}{2}, k \right) + \frac{2}{(\Delta z_k + \Delta z_{k-1})} \cdot \left(q_{ez} \left(1, k + \frac{1}{2} \right) - q_{ez} \left(1, k - \frac{1}{2} \right) \right) \\
& = n_e(1, k) \sum_j H^j(1, k) + P_{abs}(1, k)
\end{aligned} \tag{A.14}$$

where J_{er} , J_{ez} , q_{er} and q_{ez} are defined in (3.39), (3.40), (3.42), and (3.43).

LIST OF REFERENCES

LIST OF REFERENCES

- [1] J. Asmussen, "Electron cyclotron resonance microwave discharges for etching and thin-film deposition," *J. Vac. Sci. Technol. A*, vol. 7, no. 3, pp. 883-893, May/June 1989.
- [2] S. Whitechair, J. Asmussen, and S. Nakanishi, "Microwave electrothermal thruster performance in helium gas," *J. Propul. Power*, vol. 3, pp.136-144, March/April 1987.
- [3] J. Zhang, B. Huang, D. K. Reinhard, and J. Asmussen, "An investigation of electromagnetic field patterns during microwave plasma diamond thin film deposition," *J. Vac. Sci. Technol. A*, vol. 8, no. 3, pp. 2124-2128, May/June 1990.
- [4] J. Hopwood, M. Dahimene, D. K. Reinhard, and J. Asmussen, "Plasma etching with a microwave cavity plasma disk source," *J. Vac. Sci. Technol. B*, vol. 6, no. 1, pp.268-271, Jan/Feb 1988.
- [5] S. J. Pearton, U. K. Charkabarti, A. Katz, A. P. Perley, and W. S. Hobson, "Comparison of $\text{CH}_4/\text{H}_2/\text{Ar}$ reactive ion etching and electron cyclotron resonance plasma etching of In-based III-V alloys," *J. Vac. Sci. Technol. B*, vol. 9, no. 3, pp. 1421-1432, May/June 1991.
- [6] J. R. Rogers, "Properties of steady-state, high-pressure, argon microwave discharges," Ph.D. Dissertation, Michigan State University, East Lansing, 1982.
- [7] M. L. Passow, M. L. Brake, P. Lopez, W. B. McColl, and T. E. Repetti, "Microwave resonant-cavity-produced air discharges," *IEEE Trans. Plasma Sci.*, vol. 19, no. 2, pp. 219-228, April 1991.
- [8] J. B. Manring, "Electromagnetic field solutions for the natural modes of a cylindrical cavity loaded with lossy materials," Ph.D. Dissertation, Michigan State University, East Lansing, 1992.
- [9] S. Offermanns, "Resonance characteristics of a cavity-operated electrodeless high-

- pressure microwave discharge system," *IEEE Trans. Microwave Theory Tech.*, vol. 38, no. 7, pp. 904-911, July 1990.
- [10] S. Offermanns, "Electrodeless high-pressure microwave discharges," *J. App. Phys.*, vol. 67, no. 1, pp. 115-123, Jan 1990.
 - [11] K. S. Yee, "Numerical solution of initial boundary value problems involving Maxwell's equations in Isotropic media," *IEEE Trans. Antennas Propagat.*, vol. 14, no. 3, pp. 302-307, May 1966.
 - [12] R. Holand, "THREDE: a free-field EMP coupling and scattering code," *IEEE Trans. Nuclear Sci.*, vol. 24, no. 6, pp. 2416-2421, Dec 1977.
 - [13] A. Taflove, and M. E. Brodwin, "Numerical solution of steady-state electromagnetic scattering problems using the time-dependent Maxwell's equations", *IEEE Trans. Microwave Theory Tech.*, vol. 23, no. 8, pp. 623-630, Aug 1975.
 - [14] A. Taflove, "Application of the finite-difference time-domain method to sinusoidal steady-state electromagnetic-penetration problems," *IEEE Trans. Electromagn. Compat.*, vol. 22, no. 3, pp. 191-202, Aug 1980.
 - [15] G. Mur, "Absorbing boundary conditions for the finite-difference approximation of the time-domain electromagnetic-field equations," *IEEE Trans. Electromagn. Compat.*, vol. 23, no. 4, pp. 377-382, Nov 1981.
 - [16] R. Luebbers, F. P. Hunsberger, K. S. Kunz, R. B. Standler, and M. Schneider, "A frequency-dependent finite-difference time-domain formulation for dispersive materials," *IEEE Trans. Electromagn. Compat.*, vol. 32, no. 3, pp. 222-227, Aug 1990.
 - [17] C. Wang and O. P. Gandhi, "Numerical simulation of annular phased arrays for anatomically based models using the FDTD method," *IEEE Trans. Microwave Theory Tech.*, vol. 37, no. 1, pp. 118-126, Jan 1989.
 - [18] D. Sullivan, "Three-dimensional computer simulation in deep regional hyperthermia using the finite-difference time-domain method," *IEEE Trans. Microwave Theory Tech.*, vol. 38, no. 2, pp. 204-211, Feb 1990.
 - [19] J. Chen, and O. P. Gandhi, "Electromagnetic deposition in an anatomically based model of man for leakage fields of a parallel-plate dielectric heater," *IEEE Trans. Microwave Theory Tech.*, vol. 37, no. 1, pp. 174-180, Jan 1989.
 - [20] X. Zhang and K. K. Mei, "Time-domain finite difference approach to the calculation of the frequency-dependent characteristics of microstrip discontinuity," *IEEE Trans. Microwave Theory Tech.*, vol. 36, no. 12, pp. 1775-1787, Dec 1988.

- [21] X. Zhang, J. Fang, K. K. Mei, and Y. Liu, "Calculations of the dispersive characteristics of microstrips by the time-domain finite difference method," *IEEE Trans. Microwave Theory Tech.*, vol. 36, no. 2, pp. 263-267, Feb 1988.
- [22] G. Liang, Y. Liu, and K. K. Mei, "Full-wave analysis of coplanar waveguide and slotline using the time-domain finite-difference method," *IEEE Trans. Microwave Theory Tech.*, vol. 37, no. 12, pp. 1949-1957, Dec 1989.
- [23] D. M. Sheen, A. M. Ali, M. D. Abouzahra, and J. A. Kong, "Application of the three-dimensional finite-difference time domain method to the analysis of planar microstrip circuits," *IEEE Trans. Microwave Theory Tech.*, vol. 38, no. 7, pp. 849-856, July 1990.
- [24] D. H. Choi, and W. J. R. Hoefer, "The finite-difference-time-domain method and its application to eigenvalue problems," *IEEE Trans. Microwave Theory Tech.*, vol. 34, no. 12, pp. 1464-1469, Dec 1986.
- [25] A. Navarro, M. J. Nunez, and E. Martin, "Study of TE_0 and TM_0 modes in dielectric resonators by a finite difference time-domain method coupled with the discrete fourier transform," *IEEE Trans. Microwave Theory Tech.*, vol. 39, no. 1, pp. 14-17, Jan 1991.
- [26] M. F. Iskander, O. Andrade, H. Kimrey, R. Smith, and S. Lamoreaux, "Computational techniques in modeling and quantifying microwave interactions with materials," *Ceramic Transactions*, vol. 21, Ed. Clark, Gae, and Sutton, pp. 141-147, 1991.
- [27] D. B. Graves and K. F. Jensen, "A continuum model of DC and RF discharges," *IEEE Trans. Plasma Sci.*, vol. 14, no. 2, pp. 78-91, April 1986.
- [28] D. B. Graves, "Fluid model simulations of a 13.56-MHz rf discharge: time and space dependence of rates of electron impact excitation," *J. Appl. Phys.*, vol. 62, no. 1, pp. 88-94, July 1987.
- [29] J. P. Boeuf, "Numerical model of rf glow discharges," *Physical Review A*, vol. 36, no. 6, pp. 2782-2792, Sep 1987.
- [30] J. H. Tsai and C. Wu, "Two-dimensional simulations of rf glow discharges in N_2 and SF_6 ," *Physical Review A*, vol. 41, no. 10, pp. 5626-5644, May 1990.
- [31] M. J. Kushner, "Monte-Carlo simulation of electron properties in rf parallel plate capacitively coupled discharges," *J. Appl. Phys.*, vol. 54, no. 9, pp. 4958-4956, Sep 1983.
- [32] B. E. Thompson and H. H. Sawin, "Monte Carlo simulation of ion transport through rf glow-discharge sheaths," *J. Appl. Phys.*, vol. 63, no. 7, pp. 2241-2251,

April 1988.

- [33] J. I. Ulacia and J. P. McVittie, "A two-dimensional computer simulation for dry etching using Monte Carlo techniques," *J. Appl. Phys.*, vol. 65, no. 4, pp. 1484-1491, Feb 1989.
- [34] G. R. Govinda Raju and M. S. Dincer, "Monte Carlo simulation of electron swarms in nitrogen in uniform $E \times B$ field," *IEEE Trans. Plasma Sci.*, vol. 18, no. 5, pp. 819-825, Oct 1990.
- [35] T. E. Sheridan, M. J. Goeckner, and J. Goree, "Model of energetic electron transport in magnetron discharges," *Vac. Sci. Technol.*, vol. A8, no. 1, pp. 30-37, Jan/Feb 1990.
- [36] C. K. Birdsall, "Particle-in-cell charged-particle simulations, plus Monte Carlo collisions with neutral atoms, PIC-MCC," *IEEE Trans. Plasma Sci.*, vol. 19, no. 2, pp. 65-85, April 1991.
- [37] D. Vender and R. W. Boswell, "Numerical modeling of low-pressure RF plasmas," *IEEE Trans. Plasma Sci.*, vol. 18, no. 4, pp. 725-732, April 1990.
- [38] M. Surendra and D. B. Graves, "Particle simulations of radio-frequency glow discharges," *IEEE Trans. Plasma Sci.*, vol. 19, no. 2, pp. 144-157, May 1991.
- [39] H. W. Trombley, F. L. Terry, and M. E. Elta, "A self-consistent particle model for the simulation of RF glow discharges," *IEEE Trans. Plasma Sci.*, vol. 19, no. 2, pp. 158-162, April 1991.
- [40] R. W. Boswell and D. Vender, "Simulation of Pulsed electropositive and electronegative plasmas," *IEEE Trans. Plasma Sci.*, vol. 19, no. 2, pp. 141-143, April 1991.
- [41] T. A. Grotjohn, "Numerical modeling of a compact ECR ion source," *Rev. Sci. Instruments*, vol. 63, pp. 2535-2539, 1992.
- [42] M. S. Barnes, T. J. Colter, and M. E. Elta, "Large-signal time-domain modeling of low-pressure rf glow discharges," *J. Appl. Phys.*, vol. 61, no. 1, pp. 81-89, Jan 1987.
- [43] M. S. Barnes, T. J. Cotler, and M. E. Elta, "A staggered-mesh finite-difference numerical method for solving the transport equations in low pressure RF glow discharges," *J. Comp. Phys.*, vol. 77, pp. 53-72, 1988.
- [44] N. Sato and H. Tagashia, "A hybrid Monte Carlo/fluid model of RF plasmas in a SiH_4/H_2 mixture," *IEEE Trans. Plasma Sci.*, vol. 19, no. 2, pp. 102-112, April 1991.

- [45] R. K. Porteous and D. B. Graves, "Modeling and simulation of magnetically confined low-pressure plasmas in two dimensions," *IEEE Trans. Plasma Sci.*, vol. 19, no. 2, pp. 204-213, April 1991.
- [46] Y. Weng and M. J. Kushner, "electron energy distribution in electron cyclotron resonance discharges for materials processing," *J. Appl. Phys.*, vol. 72 no. 1, pp. 33-42, July 1992.
- [47] R. W. Boswell and I. J. Morey, "Self-consistent simulation of a parallel-plate rf discharge," *Appl. Phys. Lett.*, vol. 52, no. 1, pp. 21-23, Jan 1988.
- [48] J. Zhang, "Experimental development of microwave cavity plasma reactors for large area and high rate diamond film deposition," Ph. D. Dissertation, Michigan State University, 1993.
- [49] R. F. Harrington, *Time-Harmonic Electromagnetic Fields*, McGraw-Hill, 1961.
- [50] B. E. Cherrington, *Gaseous Electronic and Gas Lasers*, Pergamon, New York, 1979.
- [51] M. Surendra et al, "Self-consistent dc glow-discharge simulations applied to diamond film deposition reactors," *J. Appl. Phys.*, vol. 71, no. 10, pp. 5189-5198, May 1992.
- [52] J. D. P. Passchier and W. J. Goeheer, "A two-dimensional fluid model for an argon rf discharge," *J. Appl. Phys.*, vol. 74, no. 6, pp. 3744-3751, Sep 1993.
- [53] S. Ramo, J. R. Whinnery, and T. Van Duzer, *Fields and Waves in Communication Electronics*, Wiley, New York, 1965.
- [54] G. L. King and T. A. Grotjohn, 40th National Symposium of the American Vacuum Society, Orlando, 1993.
- [55] W. H. Press et al, *Numerical Recipes*, Cambridge University Press, 1986.
- [56] T. A. Grotjohn et al, "Modeling the electromagnetic excitation of a compact ECR ion/free radical source," *Rev. Sci. Instruments*, vol. 65, no. 5, pp. 1761-1765, May 1994.
- [57] R. K. Janev et al, *Elementary Processes in Hydrogen-Helium Plasmas*, Springer, Berlin, 1987.
- [58] G. King, "Temperature and concentration of ionic and neutral species in resonant microwave cavity plasma discharges," Ph.D. Dissertation, Michigan State University, 1994.

- [59] Fongray F. Young and Chwan-Hwa Wu, "Two-dimensional, self-consistent, three-moment simulation of RF glow discharges," *IEEE Trans. Plasma Sci.*, vol. 21, no. 3, pp. 312-321, June 1993.
- [60] Yao-Tsung Tsai, "AC simulation of field effect transistors with a hydrodynamic transport model," Ph.D. Dissertation, Michigan State University, 1990.
- [61] Chi-Jung Huang, "An investigation of hot electron induced degradation for silicon bipolar transistors," Ph.D. Dissertation, Michigan State University, 1992.
- [62] Dennis M. Manos and Daniel L. Flamm, *Plasma Etching*, Academic press, San Diago, 1989.
- [63] R. W. Hockney and J. W. Eastwood, *Computer Simulation Using Particles*, McGraw-Hill, New York, 1981.
- [64] C. K. Birdsall and A. B. Langdon, *Plasma Physics via Computer Simulation*, McGraw-Hill, New York, 1985.
- [65] M. E. Tajima-Tochiki, *Computational Plasma Physics*, Addison-Wesley, 1988.